Reduced-order model for dynamic soil-pipe interaction analysis

Thesis by
Kien Trung Nguyen

In Partial Fulfillment of the Requirements for the
Degree of
Doctor of Philosophy

Caltech

CALIFORNIA INSTITUTE OF TECHNOLOGY
Pasadena, California

2020
Defended May 15th, 2020

© 2020

Kien Trung Nguyen
ORCID: 0000-0001-5761-3156

Acknowledgements

First and foremost, I would like to express my deepest appreciation to my advisor, Professor Domniki Asimaki, for her support through my Caltech graduate journey. Domniki has given me the motivation and the freedom to pursue my research. Her guidance has significantly deepened my experience into the field of site response and geotechnical earthquake engineering. The problem-solving skills that I learn from her will absolutely benefit my future careers. I am also thankful for the excellent exemplar of a successful professor that she has provided.

Next, I would like to thank Professor José Andrade, Professor John Hall, and Professor Chiara Daraio for serving on my thesis committee, for generously offering their time and support throughout the review of this thesis, and for their insightful comments.

I would like to acknowledge Dr. Craig Davis, previously at the Los Angeles Department of Water and Power role, in motivating this work.

I would also like to acknowledge the postdoctoral researchers and PhD students in my research group, for good advice as well as collaboration and friendships. Apart from my own group, I have also learned a lot from other PhD students and professors at Caltech during my coursework, which have provided me with a solid background necessary to conduct my research. For this, I very much appreciate.

Thanks should also go to the administrative staff at the Mechanical and Civil Engineering Department, International Student Programs, and Graduate Studies Office for always being so helpful and friendly.

To my roommates, friends, and V-League group, thank you for spending time with me, offering me advice, and helping me during my time at Caltech.

Lastly, I am deeply indebted to my family and in-laws for all their love and encouragement, despite the long distance between us. And I would like to thank, with love, my wife Phuong for her understanding, constant support, and unconditional love.

Abstract

Pipelines are very vulnerable infrastructure components to geohazard-induced ground deformation and failure. How soil transmits loads on pipelines and vice versa, known as soil-pipe interaction (SPI), thus is very important for the assessment and design of resilient pipeline systems.

In the first part, this work proposes a simplified macroelement designed to capture SPI in cohesionless soils subjected to arbitrary loading normal to the pipeline axis. We present the development of a uniaxial hysteresis model that can capture the smooth nonlinear reaction force-relative displacement curves (FDCs) of SPI problems. Using the unscented Kalman filter, we derived the model parameter κ that controls the smoothness of the transition zone from linear to plastic using published experimental data. We extended this uniaxial model to biaxial loading effects and showed that the macroelement can capture effects such as pinching and shear-dilation coupling. The model input parameters were calibrated using finite element (FE) analyses validated by experiments. The FDCs of the biaxial model were verified by comparison with FE and smoothed-particle hydrodynamic (SPH) simulations for different loading patterns: cyclic uniaxial, 0-shaped, 8-shaped, and transient loading. Accounting for smooth nonlinearity, hysteresis, pinching, and coupling effects, the proposed biaxial macroelement shows good agreement with FE and SPH analyses, while maintaining the computational efficiency and simplicity of beam-on-nonlinear-Winkler foundation models, as well as a small number of input parameters.

Next, this work presents analytical solutions for computing frequency-domain axial and in-plane soil impedance functions (SIFs) for an infinitely long rigid circular structure buried horizontally in homogeneous elastic half-space. Using Hankel– and Bessel–Fourier series expansion, we solved a mixed-boundary-value problem considering a harmonic displacement at the structure boundary and traction-free boundary condition at the half-space free surface. We then verified our analytical solutions using results obtained from FE simulations. The SIFs of a buried structure in a homogeneous elastic half-space calculated by these two approaches are in perfect agreement with each other. In addition, we used analytical solutions and FE simulations to comprehensively investigate factors that affect the SIFs in homogeneous and two-layered half-spaces, respectively. The parametric study shows that SIFs of buried structures in elastic half-space primarily depend on frequency of excitation, shear modulus and Poisson's ratio of the half-space, burial depth and radius of the structure. In a two-layered soil domain, SIFs depend also on material contrast and the distance from the structure location to the interface between soil layers.

Lastly, it demonstrates how the SIFs obtained previously can be incorporated into a reduced-order model to analyze SPI problems, specifically a straight pipe subjected to Rayleigh surface wave propagating through homogeneous and heterogeneous elastic half-spaces. Calculated displacement time histories at the control points are shown to agree well with those computed by direct two-dimensional FE analyses.

Published Content and Contributions

Asimaki, D., J. Garcia-Suarez, D. Kusanovic, K. Nguyen, and E. E. Seylabi (2019), Next generation reduced order models for soil-structure interaction, in *Earthquake Geotechnical Engineering for Protection and Development of Environment and Constructions*, vol. 4, edited by F. Silvestri and N. Moraci, pp. 138–152, CRC Press, London, doi: 10.1201/9780429031274,
K.T.N participated in the conception of the project, solved and analyzed the pipeline structures, and wrote Section 4 of the manuscript.

Nguyen, K. T., and D. Asimaki (2018), A modified uniaxial Bouc–Wen model for the simulation of transverse lateral pipe-cohesionless soil interaction, in *Geotechnical Earthquake Engineering and Soil Dynamics V*, pp. 25–36, American Society of Civil Engineers, Texas, doi:10.1061/9780784481479.003,
K.T.N performed all data analysis, model development, numerical simulations, produced all figures, and wrote most of the manuscript.

Nguyen, K. T., and D. Asimaki (2020), Smooth nonlinear hysteresis model for coupled biaxial soil-pipe interaction in sandy soils, *Journal of Geotechnical and Geoenvironmental Engineering*, *146*(6), doi:10.1061/(ASCE)GT.1943-5606.0002230,
K.T.N performed all data analysis, model development, numerical simulations, produced all figures, and wrote most of the manuscript.

Table of Contents

List of Illustrations

List of Tables

C h a p t e r   1

Introduction

Contents of this chapter

1.1 Pipelines and seismic actions

Buried pipeline networks are used for the transportation of water, natural gas, fuel, and oil, and are very important lifelines of modern societies. According to the US Central Intelligence Agency (*CIA*, 2018), the total length of pipelines globally is approximately 3, 500, 000 km. In 2018 alone, operators installed approximately 24, 000 km of oil and gas pipelines worldwide, twice the length installed in 2017 (*Smith*, 2018), and this volume is expected to increase because the rapid increase in global demand for water and energy has prioritized the installation, operation and resilience requirements of transmission networks.

Frequently, pipelines are structures that extend over long distances, and cross various geologic units and geohazard zones, such as faults and liquefaction- and landslide-susceptible sites. Extensive data from past earthquakes have shown that geohazard-induced ground deformation often drives the risk to pipeline networks. According to the guidelines of the American Society of Civil Engineers (*ASCE*, 1984), the Pipeline Research Council International (*PRCI*, 2004), the American Lifeline Alliance (*ALA*, 2005), and the European Committee for Standardization (*CEN*, 2006), two types of primary earthquake hazards are relevant to the structural integrity of pipelines: (1) transient ground deformation (TGD), which is ground shaking induced by wave propagation; and (2) permanent ground deformation (PGD), namely ground failures resulting from fault ruptures, lateral spreading, landslides, and slope movements. The illustration of these seismic hazards is shown in Fig. 1.1.
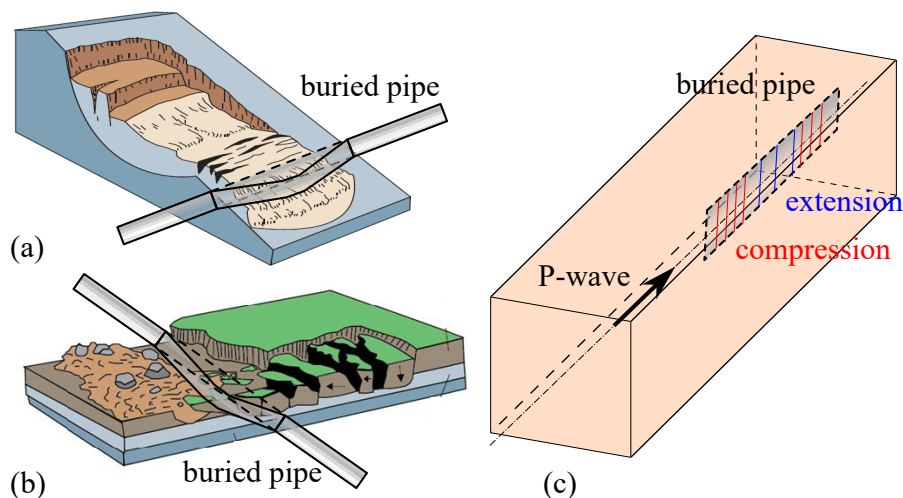
Figure 1.1: Pipe damage by: (a) landslide; (b) lateral spreading; and (c) P-wave propagation. (Adapted from *Highland et al.* 2008.)

Post-earthquake observation data have repeatedly demonstrated that pipe damage is mainly

caused by PGD (*Hamada*, 1992; *O'Rourke and Nordberg*, 1992; *O'Rourke and Palmer*, 1996; *Tang and Eidinger*, 2013; *Uckan*, 2013; *Davidson and Poland*, 2016), occurring in isolated areas with high damage rates. In contrast to common belief, TGD can potentially induce undesirable deformations in pipeline networks, especially in heterogeneous soil mediums. There is convincing evidence that TGD has considerably contributed to the pipe damage (*Sakurai and Takahashi*, 1969; *Ayala et al.*, 1989; *Lund and Cooper*, 1995; *O'Rourke and Palmer*, 1996; *O'Rourke*, 2009; *Tang and Eidinger*, 2013; *Uckan*, 2013; *Esposito et al.*, 2013). The damage due to TGD usually happens over much larger geographic areas but with lower rates compared with that due to PGD (*O'Rourke and Liu*, 1999).

1.2 Methods for soil-pipe interaction analysis
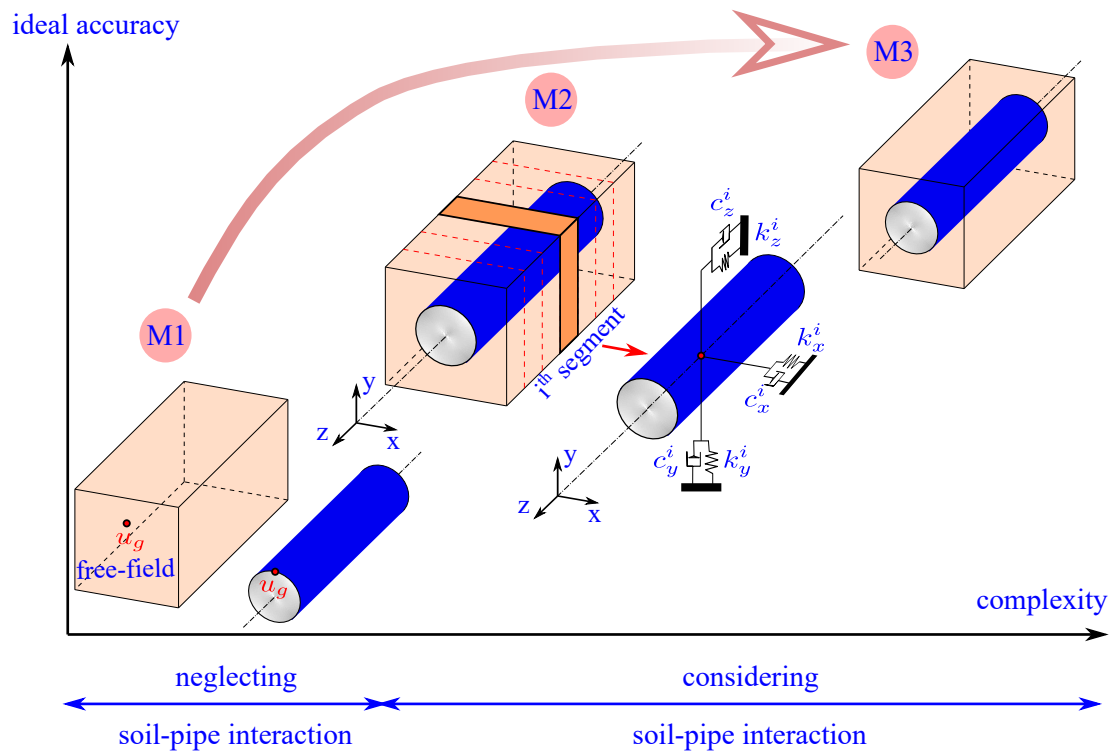
Figure 1.2: Methods for SPI analysis.

How soil transmits loads on pipelines and vice versa, known as SPI, is very important for the assessment and improvement of a pipeline system's resilience — and by extension, for performing cost-benefit analyses as part of the commodity distribution sustainability. In general, methods to analyze SPI problems can be categorized based on their complexity and ideal accuracy: model neglecting SPI (M1), reduced-order (simplified) beam-on-Winkler-foundation model considering SPI (M2), and full three-dimensional (3D) model of soil and

pipe (M3), as shown in Fig. 1.2. The following subsections present the overview of these models.

1.2.1 Model neglecting soil-pipe interaction

The most straightforward method to analyze pipeline seismic response is the one that neglects SPI phenomenon, in which pipe is assumed to be much softer than soil and cannot provide any resistance to ground motions. Hence, the pipe perfectly conforms to free-field ground motions, which are the soil displacements induced by seismic waves in the absence of excavations and structures. Despite its simplicity and simplifying assumption, such method can provide a first-order approximation of the structure deformation (*Hashash et al.*, 2001).

Newmark (1968) was among the first to provide the fundamentals of this approach. By solving a harmonic wave propagating problem in a homogeneous elastic medium, he derived a simplified, closed-form solution for estimating the maximum axial strain and curvature in underground extended structures, such as tunnels or pipelines. In a similar manner, *Kuesel* (1969) proposed the earthquake-resistant design for the San Francisco Bay Area Rapid Transit System, considering harmonic incident waves parallel and oblique to the structure axis. The maximum combined strain in structure, in conforming to wave deformation, is obtained at the critical incident angle and used as a design criteria. Meanwhile, based on Newmark's approach, *St John and Zahrah* (1987) calculated the strains and stresses experienced by structures under P-, S-, and Rayleigh waves propagation.

However, this method is limited to very stiff soils and highly flexible pipes. In case of soft soil condition, where the free-field deformation is generally larger and the stiffness of pipe prevents it from conforming to ground motion during seismic excitation, such method potentially leads to over-conservative design (*Hashash et al.*, 2001).

1.2.2 Beam-on-Winkler-foundation model considering soil-pipe interaction

This method is based on Winkler's hypothesis, which states that soil reaction at any point on the base of pipe beam depends only on the deformation at that point. *Vesic* (1961) showed that such a hypothesis is practically satisfied for infinite beams. This enables us to replace each soil segment surrounding the structure with a set of springs and dashpots formulated to represent its macroscopic reaction to differential deformations between soil and structure. For instance, the ith soil segment is replaced with a set of springs with stiffness k_x^i, k_y^i, k_z^i and dashpots with damping coefficient c_x^i, c_y^i, c_z^i along x-, y-, and z-axes, as shown in

Fig. 1.3. The pipe, meanwhile, is represented by either beam or shell elements.
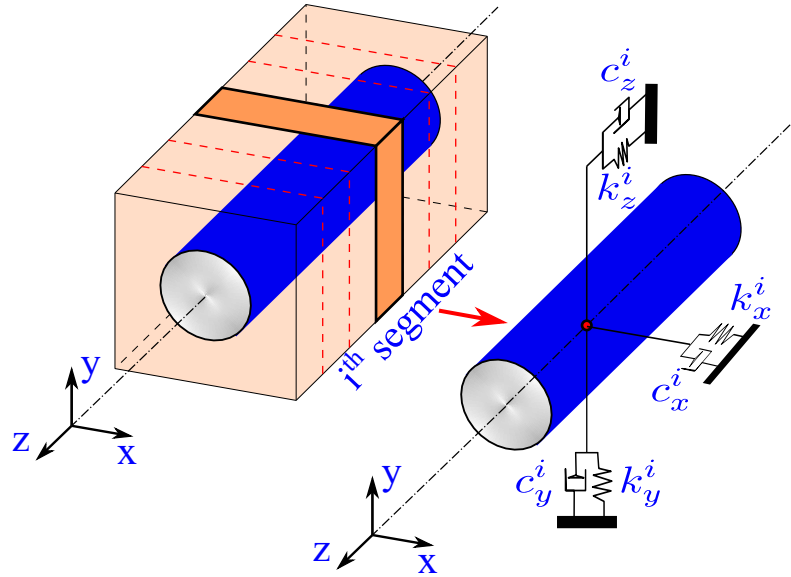
Figure 1.3: Beam-on-Winkler-foundation model based on Winkler's hypothesis.

In one-dimensional treatment of a 3D problem, the absolute axial and transverse vertical displacements, denoted as w and u, are governed by (*Hindy and Novak*, 1980)

$$m\frac{\partial^2 w}{\partial t^2} + c_z\frac{\partial w}{\partial t} + k_z w - EA\frac{\partial^2 w}{\partial z^2} = c_z\frac{\partial w_g}{\partial t} + k_z w_g, \tag{1.1}$$

$$m\frac{\partial^2 u}{\partial t^2} + c_y\frac{\partial u}{\partial t} + k_y u + EI\frac{\partial^4 u}{\partial z^4} = c_y\frac{\partial u_g}{\partial t} + k_y u_g, \tag{1.2}$$

where w_g and u_g are the imposed ground motions along axial and transverse vertical directions, m is the distributed pipe mass, t is time, E is the Young modulus, A and I are the area and the area moment of inertia of the pipe cross section, k_z, k_y and c_z, c_y are the spring stiffnesses and dashpot damping coefficients along axial and transverse vertical directions, respectively.

This method is sufficiently reliable, easy to implement, and computationally inexpensive. Hence, it has been used extensively over the years by many researchers and structural design codes (*ASCE*, 1984; *PRCI*, 2004; *ALA*, 2005; *CEN*, 2006; *PRCI*, 2009). Table 1.1 provides a (not intended to be exhaustive) list of published studies using this approach from the 1970s to the present.

In this method, accurate estimation of spring stiffness and dashpot damping coefficient is a top priority, which affects significantly the computation of internal loads and design of the

Reference	Soil	Pipe	Axis	Excitation
Sakurai and Takahashi (1969)	spring, elastic	beam	A	harmonic
Shinozuka and Koike (1979)	spring, slippage	beam	A	plane wave
Hindy and Novak (1979)	spring, dashpot	beam	A, L	San Fernando
Hindy and Novak (1980)	spring, dashpot	beam	A, L	random
Muleski and Ariman (1985)	spring	shell	A, L	harmonic
O'Rourke and El Hmadi (1988)	spring, slippage	beam	A	Rayleigh wave
Mavridis and Pitilakis (1996)	spring, dashpot	beam	A, L	S-wave
Ogawa and Koike (2001)	spring, slippage	beam	A	Rayleigh wave
Anastasopoulos et al. (2007)	spring, dashpot, slider	beam	A, L	actual records
Joshi et al. (2011)	spring	beam	A, L	reverse fault
Saberi et al. (2013)	spring	beam, shell	A	Chichi, Northridge
Liu et al. (2016)	spring	shell	A, L	strike-slip fault
A: axial, L: lateral				

Table 1.1: A non-exhaustive list of published studies using beam-on-Winkler-foundation approach.

buried structures (*Pitilakis and Tsinidis*, 2014). In the literature, these values are mainly computed by two approaches, namely mathematical models and experimental data.

As regards the mathematical models, *St John and Zahrah* (1987) numerically integrated the solution of Kelvin's and Flamant's problems, which are in turn the problems of a static load point applied within an infinite and semi-infinite homogeneous elastic media, to obtain the wavelength-dependent values of spring stiffness, expressed as

$$k_z = k_x = \frac{16\pi(1-\nu)}{(3-4\nu)}\frac{GD}{\lambda},$$ (1.3)

$$k_y = \frac{2\pi}{1-\nu}\frac{GD}{\lambda},$$ (1.4)

where D is the pipe outer diameter, λ is the wavelength of the incident sinusoidal wave, and ν and G are the Poisson's ratio and shear modulus of the medium. *Hindy and Novak* (1979); *Datta and Mashaly* (1986, 1988) combined the solution by *Mindlin* (1964), for static displacements within elastic half-space due to a concentrated load, with the solution by *Novak et al.* (1978), for dynamic plane-strain soil reactions to the harmonic motion of an embedded cylindrical body, to obtain dynamic soil spring stiffness and dashpot damping coefficient in their lumped-mass models for pipelines buried in elastic half-space.

Regarding experimental data, one of the first known experiment test to investigate SPI problems was conducted by *Audibert and Nyman* (1977), in which the transverse horizontal

response of steel pipe in loose and dense sand was investigated with a wide range of burial depth and pipe diameter. *Trautmann* (1983) performed a series of experiments to evaluate the response of buried pipes to lateral and uplift movements of loose, medium, and dense sands, with the burial depth-to-pipe diameter ratio ranging from 1.5 to 13. Later, *El Hmadi and O'Rourke* (1988) back-calculated the experimental data provided by *Colton* (1981) to achieve the bound values of axial spring constant, expressed as $1.57G \leq k_z \leq 1.70G$. Other experimental work is mentioned in Section 2.2 of this thesis.

ASCE (1984) provided the first guidelines on earthquake analysis and design of buried pipelines, describing nonlinear force-displacement curves (FDCs) of soil springs in axial, transverse horizontal, vertical upward, and vertical downward directions. Typically, these curves are ideally assumed to be elastic-perfectly plastic. Thus, only ultimate soil resistance and displacement, computed in Table 1.2, are required for the curves identification. This document is the basis for the guidelines by *ALA* (2005); *PRCI* (2004, 2009), which jointly provide the most comprehensive set of provisions for this subject.

1.2.3   Full three-dimensional model considering soil-pipe interaction

3D FE model constitutes a rigorous numerical tool to analyze SPI problems. This approach is applicable to most practical problems with complex geometries and material nonlinearities, rigorously describing distortion of pipe cross section as well as soil-pipe interface behavior. Pipe is typically represented by shell elements, while continuum soil medium is simulated using 3D solid elements. Some studies used this method include *Vazouras et al.* (2010, 2015); *Robert et al.* (2016a); *Vazouras and Karamanos* (2017); *Psyrras et al.* (2019), among many others.

However, the ability of full 3D analysis to improve on simplified method solution lies in the uncertainties of input parameters. The physical problem of SPI is sophisticated and uncertain, and includes, among other phenomena, the effects of nonlinear soil behavior, soil heterogeneity, pipe defects and/or degradation due to aging, and incoherent ground shaking. In such situations, a complex full 3D model does not necessarily produce more accurate results than a simplified one does. Depending on the problem at hand and the focus of the analysis, one might choose to adopt either simplified assumptions of pipe and soil behaviors or a full model to perform the task.

Furthermore, the 3D FE analyses are computationally expensive. Particularly in case of TGD with a large number of full dynamic time histories analyses, as well as the spatial extension of buried pipeline networks, it is computationally impossible to implement a 3D FE model to analyze such an infrastructure.

Component	Soil type	Ultimate resistance	Ultimate displacement
Axial	sand	$\dfrac{\pi D}{2}\bar{\gamma}h(1+K_0)\tan\delta$	3–5 mm for dense to loose
	clay	$\pi D\alpha S_u$	5–10 mm for stiff to soft
Horizontal	sand	$\bar{\gamma}hN_{qh}D$	0.07–0.10 $(h+D/2)$ for loose
			0.03–0.05 $(h+D/2)$ for medium
			0.02–0.03 $(h+D/2)$ for dense
	clay	$S_uN_{ch}D$	0.03–0.05 $(h+D/2)$ for stiff to soft
Upward	sand	$\bar{\gamma}hN_{qv}D$	0.01–0.015h for dense to loose
	clay	$S_uN_{cv}D$	0.1–0.2h for stiff to soft
Downward	sand	$\bar{\gamma}hN_qD + 0.5\gamma D^2N_\gamma$	0.10–0.15D
	clay	S_uN_cD	0.10–0.15D

D: pipe outer diameter.

h: burial depth.

δ: interface angle of friction between soil and pipe.

$\bar{\gamma}$: effective unit weight of soil.

γ: total unit weight of soil.

K_0: coefficient of soil pressure at rest.

S_u: undrained soil shear strength.

α: empirical coefficient varying with S_u.

N_{qh} and N_{ch}: horizontal bearing capacity factors for sand and clay.

N_{qv} and N_{cv}: vertical uplift factors for sand and clay.

N_c, N_q, and N_γ: vertical downward factors for sand and clay.

Note: ultimate resistances are per unit length of pipe.

Table 1.2: Ultimate resistance and ultimate displacement by *ASCE* (1984).

1.3 Challenges in soil-pipe interaction analysis

This thesis focuses on the reduced-order beam-on-Winkler-foundation approach. As previously mentioned, the cornerstone of such an approach is the estimation of soil spring stiffness and dashpot damping coefficient, i.e., the relationship between reaction force that soil exerts on pipe and relative displacement between them. This relationship is referred to as FDC.

One challenge lies in the simplifications associated with FDC. Most of the aforementioned work has been based on an assumption of linear or elastic-perfectly plastic idealization of a true nonlinear FDC. This idealization overlooks also hysteresis characteristics of soil in cyclic loading, which frequently exists in seismic hazards. Furthermore, published experimental and numerical studies have shown the coupling between directional components of

soil-pipe motion, which cannot be reflected using independent soil springs. Our efforts in addressing this challenge are presented in Chapter 2.

The other challenge is the lack of knowledge about soil spring stiffness and dashpot damping coefficient, a.k.a SIF, in dynamic loading scenarios. The frequency-dependent SIFs for the design of shallow and deep foundations have been established and widely accepted by the profession. However, there are no equivalent methods to account for the frequency dependence of SIFs in case of horizontally oriented buried structures. Experimental tests dealing with the derivation of equivalent soil springs are usually conducted in quasi-static loading conditions, which fail to notice the frequency dependence of spring stiffness. In view of this, our efforts to compute dynamic axial and in-plane SIFs for an infinitely long rigid circular pipe buried in elastic half-space are presented in Chapter 3 and 4, respectively.

1.4   Organization of the text

The remainder of this thesis is divided into five chapters.

Chapter 2 presents a mechanics-based reduced-order method to capture SPI under biaxial loading on a two-dimensional plane perpendicular to the pipe axis. This simplified method is able to account for the true smooth nonlinearity, the hysteresis loop, pinching phenomenon, and the coupling between lateral and vertical soil-pipe motions of the soil spring FDC. Results of the proposed method are compared with those of FE and SPH approaches for different cases of loading patterns.

Chapter 3 and 4 derive analytical solutions for computing the frequency-domain axial and in-plane SIFs, respectively, for a rigid circular structure buried in homogeneous elastic half-space. Meanwhile, FE analyses are used to calculate those impedance functions in case of two-layered[1] elastic half-space. Parametric study is conducted to investigate the dependence of SIFs on frequency of excitation, shear modulus of soil, and burial depth and dimension of the structure.

Chapter 5 demonstrates a reduced-order model to analyze pipe subjected to Rayleigh surface wave propagating through homogeneous and heterogeneous elastic half-spaces, in which the soil spring stiffness and dashpot damping coefficient are chosen based on the SIFs obtained in Chapters 3 and 4. Calculated displacement time histories at the control points are compared against those computed by direct two-dimensional FE analyses.

Chapter 6 summarizes the whole thesis and proposes potential future research directions.

---

[1]In the context of this thesis, a two-layered half-space refers to a single layer over a half-space.

C h a p t e r   2

Smooth nonlinear hysteresis model for coupled biaxial soil-pipe interaction in sandy soils

Contents of this chapter

2.1 Introduction

The beam-on-nonlinear-Winkler foundation (BNWF) model has been used extensively to analyze SPI problems, in which pipe and soil are represented by beam and elastic-perfectly plastic spring elements, respectively. SPI is accounted for through soil springs distributed along the pipe axis that simulate soil reaction from the pipe perspective.

The cornerstone of the BNWF method is the relationship between the reaction force (F) that the soil exerts on the pipe and the relative displacement between them (u); this relationship typically is referred to as FDC. Although the BNWF model and the FDC are well-known and widely used concepts, the simplifications associated with them lead to certain limitations

- Most of the previous work has been based on the assumption of a linear or elastic-perfectly plastic idealization of the true nonlinear FDC.

- The linear or elastic-perfectly plastic soil spring model is applicable only to monotonic PGD problems. It does not account for the hysteresis characteristics of soil in case of cyclic loading, which frequently exists in TGD.

- In the conventional BNWF, the vertical soil reaction is represented by uplift and bearing soil springs. Those springs are active in compression but inactive in tension (*Kouretzis et al.*, 2015), which causes a sharp change in the FDC stiffness in the vicinity of equilibrium. However, in cyclic loading tests, closing of the gap between soil and pipe during the unloading phase occurs through a smooth change from uplift stiffness K_{y1}, through 0, to bearing stiffness K_{y2} at zero deformation ($y = 0$), known as the pinching effect (Fig. 2.1). Experimental data were reported by *Finch* (1999).

- Published experimental and numerical studies (*Nyman*, 1984; *Hsu*, 1996; *Yimsiri et al.*, 2004; *Guo and Stolle*, 2005; *Daiyan*, 2013; *Jung et al.*, 2016) have shown that to achieve a realistic approximation of soil reactions using soil springs, the springs should be coupled instead of acting independently, as is assumed by BNWF theory.

Although axial strains are clearly dominant in pipe response to ground deformation, *Yan et al.* (2018) showed that bending strains become important for non-uniform excitation caused by, for example, propagation of surface waves across sedimentary basins (*Ayoubi et al.*, 2018). Accordingly, this chapter focused on the coupled reaction forces of the soil when the pipe moves obliquely on a two-dimensional (2D) vertical plane perpendicular to the pipe axis. The approach presented here is capable of simulating the true nonlinear FDC, hysteresis of the soil reaction force in dynamic cyclic loading, pinching effects upon
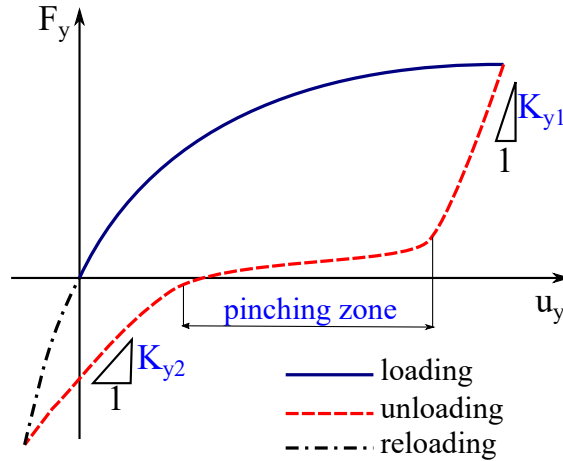
Figure 2.1: Pinching effect observed from vertical cyclic pipe loading.

unloading, and coupling effects between lateral and vertical soil springs. The proposed model was systematically verified and validated by comparison with published experimental and numerical data, as well as numerical simulations carried out by the authors. The limitations of the approach are that it currently is applicable to the case of rigid (or nearly rigid) pipes, and that it cannot capture the post-peak (softening) behavior of FDC, which has been observed for dense to very dense sands.

This chapter is organized as follows. In Section 2.2, we derive a uniaxial hysteretic model to capture the true nonlinear FDC for monotonic loading. Section 2.3 extends the model to biaxial hysteretic, considering the pinching effect and coupling between the lateral and vertical directions of loading. Finally, in Section 2.4, results of the biaxial model are verified by comparison with finite element method (FEM), SPH simulations, and BNWF method with elastic-perfectly plastic soil springs calculated following *ASCE* (1984) guidelines.

2.2 Uniaxial hysteresis model

The formulation of our uniaxial hysteretic model is based on the work by *Bouc* (1971) and *Wen* (1976) on nonlinear hysteretic systems. The so-called Bouc–Wen (BW) model is applicable to SPI problems, in which the soil reaction force F per unit length of the pipe associated with the relative soil-pipe displacement u is calculated as

$$F = \alpha K u + (1 - \alpha) F_u \zeta \tag{2.1}$$

where α is the ratio of post-yield to initial stiffness of the soil, K is the soil initial stiffness, F_u is the ultimate soil reaction force (yield strength), and ζ is a dimensionless hysteresis parameter.

In the original BW model, the parameter ζ is governed by the nonlinear differential equation $\dot{\zeta} = \left(1 - |\zeta|^n \big(\beta \operatorname{sgn}(\dot{u}\zeta) + \gamma\big)\right)\dot{u}/u_0$, where $u_0 = F_u/K$ is the yield displacement, β and γ control the unloading-reloading stiffness ($\beta + \gamma = 1$), n controls the smoothness of the transition zone (between the linear and asymptotic sections of the FDC), and sgn is the sign function. However, using the preceding definition of ζ, the model has limited flexibility to capture force-displacement nonlinearity (depicted as the shaded area between $n = +\infty$ and $n = 1$ in Fig. 2.2), and *Nguyen and Asimaki* (2018) demonstrated that representative FDCs for SPI problems require a more versatile function (especially for the case of loose sands). To overcome this limitation, we used the modified Bouc–Wen (MBW) equation, originally proposed by *Varun and Assimaki* (2012) and subsequently used by *Asimaki et al.* (2019), to express the variation of ζ with relative displacement

$$\dot{\zeta} = \frac{1}{u_0}\left(1 - \frac{\tanh(\kappa|\zeta|)}{\tanh \kappa}\big(\beta \operatorname{sgn}(\dot{u}\zeta) + \gamma\big)\right)\dot{u} \tag{2.2}$$

where κ is a dimensionless constant that controls the smoothness of the transition zone in lieu of n, but with a broader range of nonlinearity (Fig. 2.2).
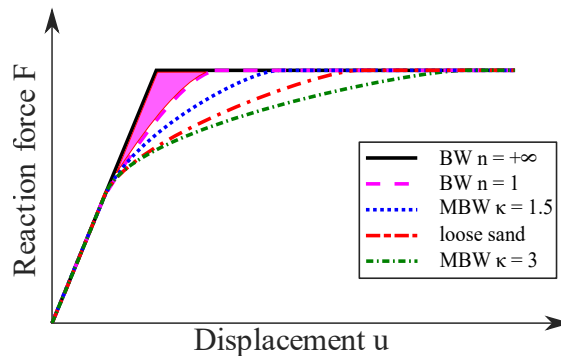
Figure 2.2: Smoothness of FDC depending on κ. (Reprinted from *Nguyen and Asimaki* 2018, © ASCE.)

Nguyen and Asimaki (2018) determined the values of κ for transverse lateral SPI in dry sand: $\kappa = 1.2$–1.9 and $\kappa = 0.0$–0.2 for loose and dense sand, respectively. In this study, we derived κ for combined vertical–transverse displacement of the pipe on a plane normal to the pipe axis, in loose, medium, and dense sand with relative density $I_D = 0$–35%, 35%–65%, and 65%–100%, respectively. The embedment ratio (H/D) cases in this study varied from 1.0 to 12.5, where H is the burial depth to the pipe centerline and D is the pipe diameter. The value of κ was back-calculated from the FDCs of published physical experiments (*Audibert and Nyman*, 1977; *Trautmann*, 1983; *Dickin*, 1994; *Hurley and Phillips*, 1999; *Bransby et al.*, 2001; *Hsu et al.*, 2001; *Di Prisco and Galli*, 2006; *Karimian et al.*, 2006; *Olson*, 2009;

Daiyan, 2013; *Robert and Thusyanthan*, 2015; *Burnett*, 2015; *Robert et al.*, 2016b) using the unscented Kalman Filter (UKF), an optimal estimator through which we extracted the unknown variables (*Simon*, 2006). From Eqs. (2.1) and (2.2), the discrete-time nonlinear system for κ estimation is

$$
\begin{cases}
\zeta_{n+1} = \zeta_n + \dfrac{K}{F_u}\left(1 - \dfrac{\tanh(\kappa_n|\zeta_n|)}{\tanh \kappa_n}\Big(\beta \operatorname{sgn}\big((u_{n+1} - u_n)\zeta_n\big) + \gamma\Big)\right)(u_{n+1} - u_n) + w_n \\
\kappa_{n+1} = \kappa_n + w'_n \\
F_n = (1 - \alpha)F_u\zeta_n + \alpha K u_n + v_n
\end{cases}
$$

$$(2.3)$$

where subscripts n and $n + 1$ indicate state parameters at time step t_n and t_{n+1}, respectively; w_n and w'_n are process noises; and v_n is measurement noise.

One parameter needs to be estimated: κ. The perfectly plastic (with no hardening) behavior of the FDC at large displacements indicates that the post-yield stiffness of the soil is 0, and thus $\alpha = 0$. We used experimental results from *Robert et al.* (2016b) to demonstrate how we derived κ. Fig. 2.3(a) presents the experimentally measured lateral FDC for dry medium Cornell sand, with relative density $I_D = 35.5\%$ and for the case of $H/D = 5.3$. Because the MBW model cannot capture the post-peak behavior of the FDC, only the monotonically increasing resistance-displacement part of the FDC was used as input in the optimization scheme, F_n - u_n, for Eq. (2.3). For this curve, $\operatorname{sgn}\big((u_{n+1} - u_n)\zeta_n\big) = 1$, and hence $\beta \operatorname{sgn}\big((u_{n+1} - u_n)\zeta_n\big) + \gamma = \beta + \gamma = 1$. The values of F_u and K were determined directly from the FDC, $F_u = 20$ kN and $K = 4.5$ kN/mm. The process and measurement noise for the UKF were chosen as random signals with 0-mean and standard deviation 10^{-3} and 1.0, respectively. Fig. 2.3(b) shows the estimated values of κ converging to 1.1 as more data points are recursively included in UKF. In this example, the estimated value $\kappa = 1.1$ was used in the MBW to generate the FDC and confirm the excellent fit of the experimental data to the idealized MBW model with estimated parameter κ, as shown in Fig. 2.3(a).

It should be noticed that κ is a dimensionless parameter. Although the input FDC, F_n - u_n, is dimensional, it is implicitly normalized in Eq. (2.3), e.g., F_n/F_u and $(u_{n+1} - u_n)/(F_u/K)$.

In the same way, we used UKF estimation to obtain κ from an extensive set of experimental data available in the literature. Because of a lack of experimental results in some cases, we used validated FE simulations, which are described in detail in Section 2.4. Results are summarized in Fig. 2.4, which shows that κ for lateral and uplift displacements depends on H/D for dense, medium and loose sand. Results show that κ is most sensitive to the variation of H/D for loose sands, and least sensitive to the variation of H/D for dense sands. From a physical point of view, softer soil requires larger relative displacement to reach the
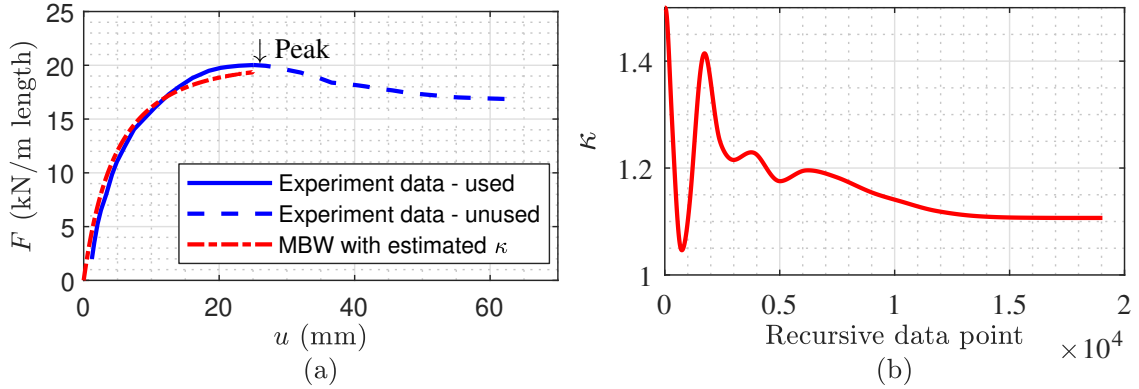
Figure 2.3: Estimating κ by UKF method: (a) FDC and MBW (data from *Robert et al. 2016b*); and (b) κ estimation.

ultimate soil reaction force. The transition zone in this case is longer and smoother, and accordingly, κ is larger. A similar trend was observed for medium-dense sands. For dense sands, $\kappa \approx 0$, indicating an abrupt change from the linear regime to the peak strength over a small soil-pipe relative displacement increment.
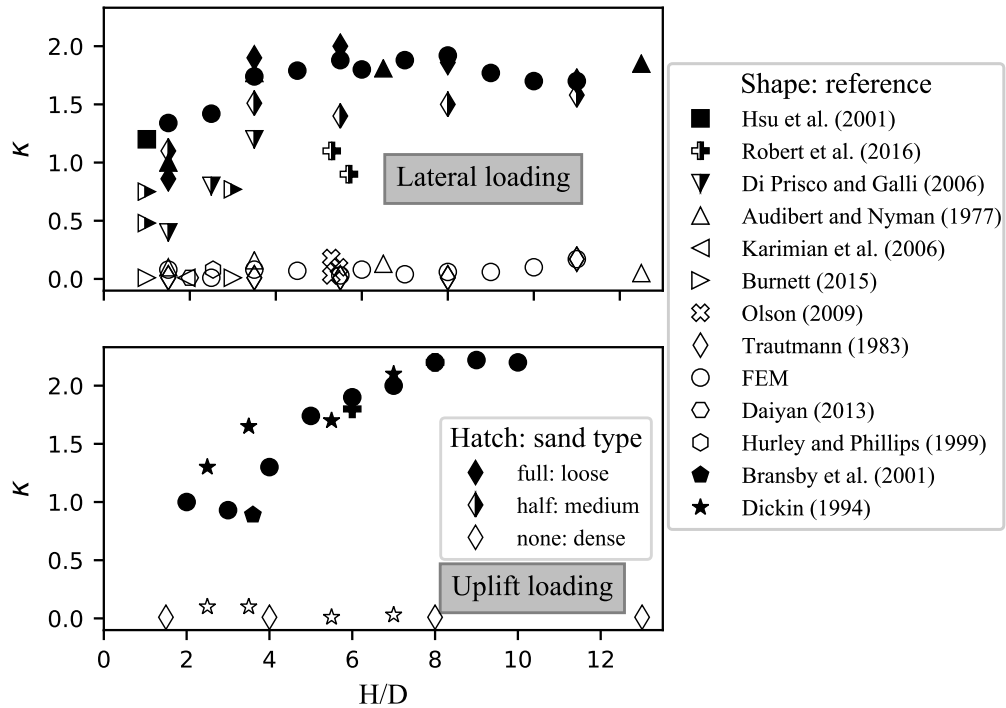
Figure 2.4: κ for loose sand $I_D = 0$–35%, medium sand $I_D = 35$%–65%, dense sand $I_D = 65$%–100% for lateral and uplift pipe movement.

As a function of embedment depth, κ increases gradually with H/D up to a maximum value

near H/D = 6–8. For larger embedment depths, κ remains constant. This trend of κ is directly related to the failure mechanism of SPI (*Nguyen and Asimaki*, 2018). For shallow buried pipelines, the soil failure follows a "passive-wedge" mode, in which the shear band develops and reaches the soil surface. The change from linear to the asymptote region is not very smooth, which translates to a small κ. As the pipe embedment depth increases, the transition zone becomes smoother, and κ is larger. This corresponds to the transition of the soil failure from a "passive-wedge" to a "plow-through" mode at a critical depth H/D = 6–8. This critical depth is consistent with experimental data by *Trautmann* (1983) for loose and medium sands.

Similarities in trend and values of κ for lateral and uplift cases suggest that a biaxial model with a single value of κ should be sufficient to simulate SPI problems. Although the MBW model cannot capture the post-peak behavior, this limitation is not expected to affect pipeline design significantly. The model still can capture the ultimate soil reaction force that determines the upper bound of the force acting on a pipe, and the response envelope which the pipeline will be designed to withstand is independent of the post-peak section of FDC.

2.3 Biaxial hysteresis model

For the uniaxial model described in Eqs. (2.1) and (2.2), the direction of incremental reaction force $\vec{\mathrm{d}F}$ (i.e., the direction of $\vec{\mathrm{d}\zeta}$ when $\alpha = 0$) is parallel to that of the incremental relative displacement $\vec{\mathrm{d}u}$. For the case of bilateral loading, *Varun and Assimaki* (2012) showed that $\vec{\mathrm{d}F}$ (denoted $\vec{\mathrm{d}p}$ in that paper) depends not only on $\vec{\mathrm{d}u}$ but also on the plastic region developing around the pipe (current $\vec{\zeta}$). For example, in Fig. 2.5(a) the pipe is continuously pushed in one direction, $\vec{\mathrm{d}u} \parallel \vec{\zeta}$ (the symbol $\parallel$ is used to denote "parallel to"), so $\vec{\mathrm{d}F}$ ($\vec{\mathrm{d}\zeta}$) $\parallel$ $\vec{\mathrm{d}u}$. If, however, as shown in Fig. 2.5(b), the pipe is loaded at an angle ψ relative to the direction of first loading ($\vec{\zeta}$) after a plastic zone forms, the soil stress state is no longer symmetric, so $\vec{\mathrm{d}F}$ ($\vec{\mathrm{d}\zeta}$) $\nparallel$ $\vec{\mathrm{d}u}$. In local coordinates, as in Fig. 2.6, $\vec{\mathrm{d}\zeta}$ is projected onto $\vec{\mathrm{d}u}$ and its perpendicular direction

$$\vec{\mathrm{d}\zeta} = \begin{bmatrix} \mathrm{d}\zeta_{ii} \\ \mathrm{d}\zeta_{ij} \end{bmatrix} = \begin{bmatrix} k_{ii} & k_{ij} \\ k_{ij} & k_{ii} \end{bmatrix} \begin{bmatrix} \mathrm{d}u \\ 0 \end{bmatrix} \frac{1}{u_0} = \mathbf{K}\frac{\vec{\mathrm{d}u}}{u_0} \tag{2.4}$$

where $k_{ii} = 1 - f_\zeta(\beta\cos\psi + \gamma)$ is the diagonal stiffness term, $k_{ij} = cf_\zeta\sin\psi$ is the cross-stiffness term, $\mathbf{K}$ is the stiffness matrix, $f_\zeta = \tanh(\kappa|\vec{\zeta}|)/\tanh\kappa$, $\cos\psi = (\vec{\zeta}\cdot\vec{\mathrm{d}u})/(|\vec{\zeta}||\vec{\mathrm{d}u}|)$, $\sin\psi = (\vec{\zeta}\times\vec{\mathrm{d}u})/(|\vec{\zeta}||\vec{\mathrm{d}u}|)$, and c is a coefficient controlling the degree of coupling between the two directions.
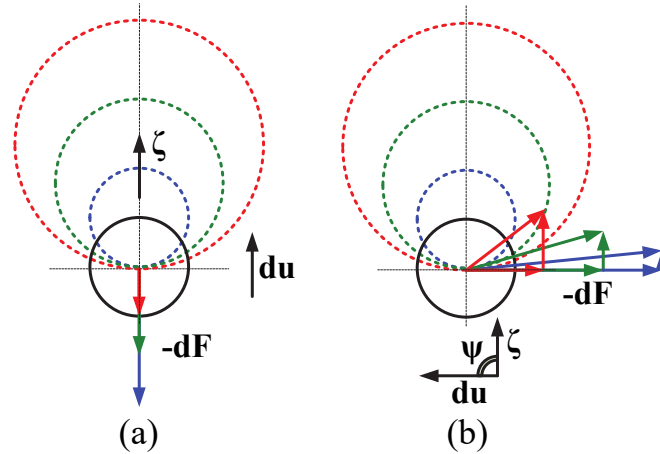
Figure 2.5: Incremental reaction force as a function of nonlinearity: (a) $\vec{du} \parallel \vec{\zeta}$; and (b) $\vec{du} \nparallel \vec{\zeta}$. (Adapted from *Varun and Assimaki* 2012.)
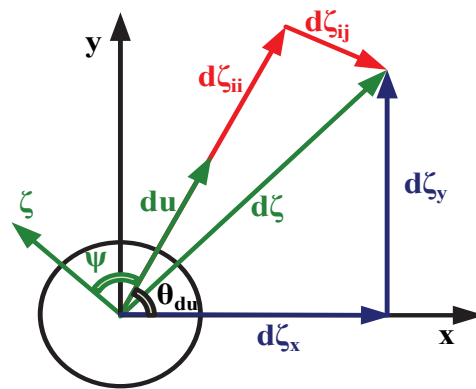
Figure 2.6: Transformation from local to global coordinate system. (Adapted from *Varun and Assimaki* 2012.)
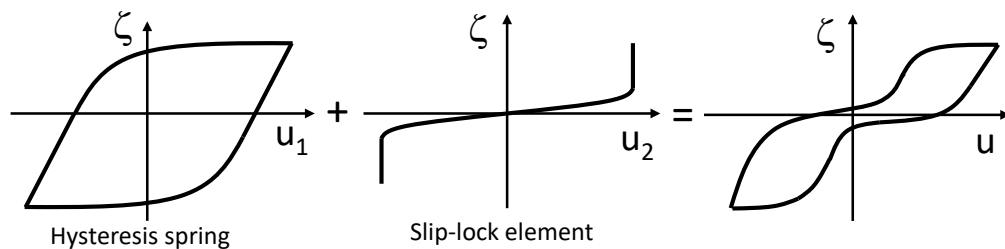
Figure 2.7: Hysteresis spring in series with slip-lock element.

Eq. (2.4) captures the relationship between $\vec{dF}$ and $\vec{du}$ without considering the pinching effect. During cyclic loading, however, the FDC may exhibit pinching due to the gap formed between soil and pipe that needs to close before any resistance is offered by the soil upon stress reversal. To account for this phenomenon, $\vec{du}$ is decomposed into two components: one corresponding to a nonlinear, hysteresis spring $\vec{du_1}$; and the other corresponding to a

slip-lock element $\vec{du}_2$. So $\vec{du} = \vec{du}_1 + \vec{du}_2$. Fig. 2.7 shows the general form of the FDC when a hysteresis spring is put in series with a slip-lock element. Similar to Eq. (2.4), in local coordinates, the dimensionless hysteresis parameter is

$$\vec{d\zeta} = \begin{bmatrix} d\zeta_{ii} \\ d\zeta_{ij} \end{bmatrix} = \begin{bmatrix} k_{ii} & k_{ij} \\ k_{ij} & k_{ii} \end{bmatrix} \begin{bmatrix} du_1 \\ 0 \end{bmatrix} \frac{1}{u_0} \tag{2.5}$$

For the slip-lock element, the equation of motion has similar form with the one-dimensional (1D) equation by *Baber and Noori* (1985), and preserves the same ratio between diagonal and off-diagonal elements of the tangent stiffness tensor in Eq. (2.5)

$$\vec{d\zeta} = \begin{bmatrix} d\zeta_{ii} \\ d\zeta_{ij} \end{bmatrix} = \frac{1}{p_\zeta} \begin{bmatrix} 1 & \dfrac{k_{ij}}{k_{ii}} \\ \dfrac{k_{ij}}{k_{ii}} & 1 \end{bmatrix} \begin{bmatrix} du_2 \\ 0 \end{bmatrix} \frac{1}{u_0} \tag{2.6}$$

where

$$p_\zeta = \frac{1}{2}(1 - \operatorname{sgn} \dot{u}_y)\sqrt{\frac{2}{\pi}}\frac{s}{\sigma} \exp\left(-\frac{1}{2}\left(\frac{\zeta}{\sigma}\right)^2\right) \tag{2.7}$$

where s and σ control the length and sharpness of pinching, respectively. For a system that deteriorates, s is assumed to be a function of cumulative damage measure, in which the maximum displacement and dissipated energy are among the most frequently used (*Wang and Chang*, 2007). The present work used the following relation:

$$s = \delta_s\left(\frac{u_{ymax}}{u_0}\right)^2 \tag{2.8}$$

where δ_s is a coefficient, and u_{ymax} is the maximum relative displacement that has occurred in the process of cyclic loading in the vertical direction. Due to gravity, the gap between soil and pipe can appear only below the pipe; hence, the factor $(1 - \operatorname{sgn} \dot{u}_y)$ in Eq. (2.7) indicates that pinching appears only when the pipe moves downward.

From Eqs. (2.5) and (2.6), simple algebraic manipulation obtains

$$\begin{bmatrix} d\zeta_{ii} \\ d\zeta_{ij} \end{bmatrix} = \frac{1}{1 + k_{ii}p_\zeta} \begin{bmatrix} k_{ii} & k_{ij} \\ k_{ij} & k_{ii} \end{bmatrix} \begin{bmatrix} du \\ 0 \end{bmatrix} \frac{1}{u_0} \tag{2.9}$$

In global coordinates (Fig. 2.6), obtained using a transformation tensor, Eq. (2.9) becomes

$$\vec{d\zeta} = \begin{bmatrix} d\zeta_x \\ d\zeta_y \end{bmatrix} = \frac{1}{1 + k_{ii}p_\zeta} \begin{bmatrix} k_{ii}\cos\theta_{du} - k_{ij}\sin\theta_{du} \\ k_{ij}\cos\theta_{du} + k_{ii}\sin\theta_{du} \end{bmatrix} \frac{du}{u_0} \tag{2.10}$$

where $\theta_{\mathrm{d}u}$ is the angle between $\vec{\mathrm{d}u}$ and x-axis. Eq. (2.10) is rewritten in differential form as

$$\begin{bmatrix} \dot{\zeta}_x \\ \dot{\zeta}_y \end{bmatrix} = \frac{1}{1 + k_{ii}p_\zeta} \begin{bmatrix} k_{ii}\dot{u}_x - k_{ij}\dot{u}_y \\ k_{ij}\dot{u}_x + k_{ii}\dot{u}_y \end{bmatrix} \frac{1}{u_0} \tag{2.11}$$

If $\delta_s = 0$ then $p_\zeta = 0$, and Eq. (2.11) is identical to the corresponding formulation of *Varun and Assimaki* (2012).

Eq. (2.11) is applicable only to isotropic, symmetric cases, namely for cases where the ultimate reaction force F_u and initial stiffness K of the soil are independent of direction, and the magnitude of positive ultimate reaction force equals that of negative ultimate reaction force. Use of this formulation in SPI problems, therefore, required modifications because (1) along the vertical axis, the magnitude of the ultimate positive reaction F_{uy1} (uplift resistance capacity) is smaller than that of the ultimate negative reaction F_{uy2} (downward bearing capacity), i.e., the FDC is asymmetric along the vertical axis; (2) the initial soil stiffness for upward pipe movement K_{y1} and downward pipe movement K_{y2} are unequal; (3) the soil stiffness K_x and ultimate reaction force F_{ux} along the horizontal axis are not equal to K_y and F_{uy} along the vertical axis, i.e., the soil stiffness and strength are anisotropic, and (4) $\vec{\mathrm{d}F}$ depends not only on the plastic zone as mentioned previously, but also on the initial anisotropy of geostatic stresses.

To account for the aforementioned complexities associated with SPI problems, we made the following modifications:

1. F_{uy} was modified to: $F_{uy} = \big((1 + \mathrm{sgn}\,\zeta_y)F_{uy1} + (1 - \mathrm{sgn}\,\zeta_y)F_{uy2}\big)/2$.

2. Fig. 2.8 schematically depicts the soil stiffness that characterizes the branches of a load-unload-reload FDC cycle for vertical loading (ABCDEB): for the first loading branch, AB, the pipe moves upward and the soil has initial stiffness K_{y1}. A gap is formed below the pipe. In branch BC, the pipe moves downward, but does not touch the soil below. Due to gravity, the upper soil remains in contact with the pipe, so the initial stiffness is continually K_{y1}. For branch CD of the FDC, the pipe continues to move downward and touches the soil below, which now has stiffness K_{y2}. Upon load reversal (branch DEB), the pipe travels upward, loses contact with the lower soil, and comes in contact with upper soil again, and the stiffness is once again K_{y1}. As a result, the stiffness along the y-axis can be idealized as $K_y = K_{y1} + (1 - \mathrm{sgn}\,\zeta_y)(1 - \mathrm{sgn}\,\dot{u}_y)(K_{y2} - K_{y1})/4$.
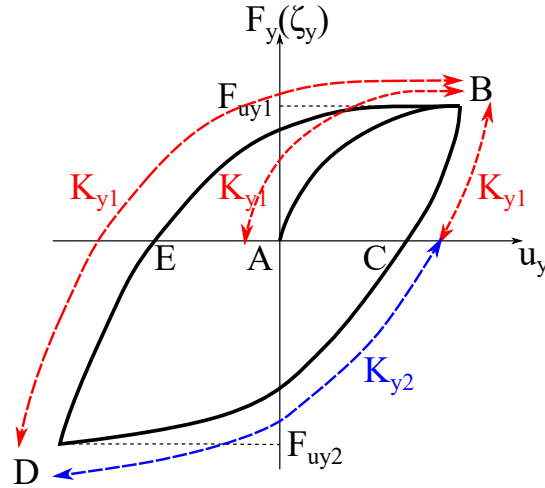
Figure 2.8: Initial stiffness in different parts of FDC.

3. We used the following transformation to make the problem isotropic: $u'_y = u_{0x}u_y/u_{0y}$, where $u_{0x} = F_{ux}/K_x$ and $u_{0y} = F_{uy}/K_y$. In global coordinates, the dimensionless hysteresis parameters are calculated as follows in the transformed domain:

$$
\begin{cases}
\dot{\zeta}_x = \dfrac{1}{u_{0x}(1 + k_{ii}p_\zeta)}\left(k_{ii}\dot{u}_x - k_{ij}\dfrac{u_{0x}}{u_{0y}}\dot{u}_y\right) \\
\dot{\zeta}_y = \dfrac{1}{u_{0x}(1 + k_{ii}p_\zeta)}\left(k_{ij}\dot{u}_x + k_{ii}\dfrac{u_{0x}}{u_{0y}}\dot{u}_y\right)
\end{cases}
\tag{2.12}
$$

4. The cross-stiffness component $c f_\zeta \sin \psi$ represents the directional difference between $\vec{dF}$ ($\vec{d\zeta}$) and $\vec{du}$ due to the formation of a plastic zone, assuming that prior to the first loading (under geostatic stresses), the soil stiffness and strength are isotropic. If the pipe is pushed monotonically along a fixed direction in the isotropic medium under geostatic conditions, $\psi = 0$ and $k_{ij} = 0$, and $\vec{d\zeta} \parallel \vec{du}$. However, geostatic stresses introduce anisotropy and further separate the direction $\vec{dF}$ ($\vec{d\zeta}$) and $\vec{du}$. In these conditions, even if the pipe is pushed along one fixed direction, the direction of $\vec{dF}$ ($\vec{d\zeta}$) still is different than that of $\vec{du}$ by an angle χ, which is attributed to the anisotropy of geostatic stresses.

Fig. 2.9 introduces the variation of χ with loading direction of the pipe: If $\theta_{du} = \pm 90°$, then $\chi = 0$ because geostatic stresses are symmetric about the off-plane horizontal y-axis. If $\theta_{du} = 0°$, then $\chi = \chi_0$, where χ_0 can be estimated from experiments or numerical simulations (Section 2.4). Because χ depends only on θ_{du}, we propose the

bell-shaped curve in Fig. 2.9:

$$\chi = \begin{cases} \chi_0 \left(\dfrac{4}{\pi^2}\right)^4 \left(\left(\theta_{du} + \dfrac{\pi}{2}\right)\left(-\theta_{du} + \dfrac{\pi}{2}\right)\right)^4 & \text{if } -\dfrac{\pi}{2} \le \theta_{du} \le \dfrac{\pi}{2} \\[3mm] -\chi_0 \left(\dfrac{4}{\pi^2}\right)^4 \left(\left(\theta_{du} - \dfrac{\pi}{2}\right)\left(-\theta_{du} + \dfrac{3\pi}{2}\right)\right)^4 & \text{if } \dfrac{\pi}{2} < \theta_{du} \le \dfrac{3\pi}{2} \end{cases} \tag{2.13}$$

The cross-stiffness k_{ij} is modified by adding one component k_{ij1} to account for the anisotropic state of geostatic stresses: $k_{ij} = c f_\zeta \sin\psi + k_{ij1}$. When $\psi = 0$, $k_{ii} = 1 - f_\zeta$ and $k_{ij} = k_{ij1}$. From Eq. (2.9), $k_{ij}/k_{ii} = \mathrm{d}\zeta_{ij}/\mathrm{d}\zeta_{ii} = -\tan\chi$ (where $\chi = \theta_{du} - \theta_{d\zeta}$). Therefore, $k_{ij1} = -(1 - f_\zeta)\tan\chi$. Next, to ensure that $k_{ij1} = 0$ when $\zeta = 0$, k_{ij1} is multiplied by the weight function f_ζ, so that $k_{ij} = c f_\zeta \sin\psi - f_\zeta(1 - f_\zeta)\tan\chi$. Because χ is small, we approximate $\tan(\chi) \approx \chi$ to simplify the differential equation at hand; the error introduced is approximately 4% for $\chi = 20°$. Consequently, k_{ij} is expressed as: $k_{ij} = c f_\zeta \sin\psi - f_\zeta(1 - f_\zeta)\chi$.
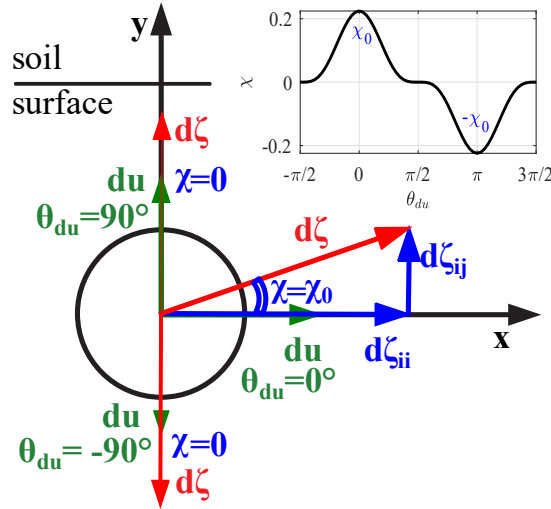
Figure 2.9: Values of χ for variation of θ_{du}.

The final system of equations (expressed in global coordinates) for the smooth nonlinear, hysteretic, biaxial MBW model with pinching that has been presented so far (henceforth

referred to as BMBW) is:

$$
\begin{cases}
F_x = \alpha K_x u_x + (1 - \alpha) F_{ux} \zeta_x \\
F_y = \alpha K_y u_y + (1 - \alpha) F_{uy} \zeta_y \\
F_{uy} = \frac{1}{2} \big((1 + \text{sgn}\, \zeta_y) F_{uy1} + (1 - \text{sgn}\, \zeta_y) F_{uy2} \big) \\
K_y = K_{y1} + \frac{1}{4} (1 - \text{sgn}\, \zeta_y)(1 - \text{sgn}\, \dot{u}_y)(K_{y2} - K_{y1}) \\
u_{0x} = F_{ux}/K_x; \quad u_{0y} = F_{uy}/K_y \\
k_{ii} = 1 - f_\zeta (\beta \cos \psi + \gamma) \\
k_{ij} = c f_\zeta \sin \psi - f_\zeta (1 - f_\zeta) \chi \\
\dot{\zeta}_x \text{ and } \dot{\zeta}_y \text{ are determined by Eq. (2.12)}
\end{cases}
\tag{2.14}
$$

The physical interpretation of this reduced-order model, relative to the continuum model, is demonstrated in Fig. 2.10. The model inputs were classified into three groups: physical parameters, shape-control parameters of the hysteresis loop, and pinching-control parameters. The model input parameters are summarized in Table 2.1.
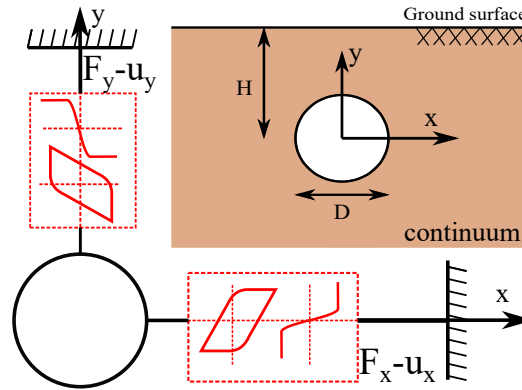
Figure 2.10: Schematic illustration of continuum and proposed reduced model.

2.4 Numerical verification

This section presents results of the verification analyses we conducted to evaluate the proposed BMBW method; comparison of our model predictions with FEM and SPH numerical analyses were necessary due to the scarcity of experimental data on pipe response to biaxial cyclic loading in dry sands. The FEM and SPH simulations were validated using available experimental results for lateral loading, and subsequently were used to generate FDCs for different cases of pipe loading to verify the proposed model.

Category	Input parameter	Description
Physical quantities	α	ratio of post-yield to initial stiffness of soil
	K_x, K_{y1}, K_{y2}	initial soil stiffness along transverse lateral, upward vertical, and downward vertical directions
	F_{ux}, F_{uy1}, F_{uy2}	ultimate soil reaction force along transverse lateral, upward vertical, and downward vertical directions
	c	coefficient of cross-stiffness term in biaxial model
	χ_0	angle between incremental relative displacement and incremental reaction force at $\theta_{du} = 0$
Shape of hysteresis loop	κ	smoothness of transition zone
	β, γ	general shape of hysteresis loop, $\beta + \gamma = 1$
Pinching control	δ_s	coefficient of pinching length
	σ	coefficient of pinching sharpness

Table 2.1: Summary of input parameters for the proposed BMBW model.

Trautmann (1983) conducted experiments to study SPI under lateral and uplift loading in dry loose, medium, and dense sand, for H/D varying from 1.5 to 13. We used data from Test 20 as the benchmark to validate our numerical models. In that test setup, the 102-mm-outer-diameter pipe was embedded at $H/D = 5.5$ and pushed laterally in dry loose Cornell filter sand which had density $\gamma_s = 14.8$ kN/m^3, friction angle obtained from direct shear test $\phi'_{ds} = 31°$, and relative density $I_D = 0\%$.

2.4.1   Finite element method

The FEM analyses were conducted using 3D LS-DYNA R10.0.0. The pipe was modeled as a rigid cylinder, with an outside diameter $D = 100$ mm. The soil medium was represented by constant stress hexahedron elements, and an elastic-perfectly plastic constitutive model with the Mohr–Coulomb failure criterion. For loose sand, the dilation angle was assumed to be $\psi_s = 0$. *Olson* (2009) reported that the plane-strain friction angle is $\phi'_{crit} = 38.6°$, considering the maximum stress obliquity in the soil medium. A small value of cohesion, $c = 0.1$ kPa, which had negligible effect on the result, was applied to increase the stability of the numerical model. The interface between soil and pipe was modeled by automatic-surface-to-surface contact, allowing separation and slip. The friction at the interface followed the Coulomb friction model with friction angle $0.6\phi'_{crit}$ (*Trautmann*, 1983). The Poisson's ratio was $\nu = 0.3$. *O'Rourke* (2010) suggested an empirical equation for Young's modulus used in plane-strain simulation: $E = 2 \times 10^{-13.97}(\gamma_s \sigma_{vc}^{0.0378})^{13.7}$, where σ_{vc} is the vertical overburden stress at the pipe centerline. The shear modulus G initially was calculated based

on that equation. It then was calibrated to better fit the FDC of Test 20. Eventually, $G = 230$ kPa was taken at the pipe centerline. An approximately linear variation of shear modulus with depth then assumed $\partial G / \partial y = -400$ kPa/m to reflect the dependency of shear modulus on the soil overburden pressure.

The geometry mesh and boundary conditions for the FEM model are shown in Fig. 2.11(a). The side nodes were constrained along x-direction, whereas the bottom nodes were pinned. To ensure plane-strain conditions, all nodes were constrained in the out-of-plane direction. The numerical simulation was executed in two stages. First, the model with soil and pipe was analyzed under gravity loading to generate the initial (geostatic) stress state. Second, the desired pipe movement was imposed in a displacement-controlled manner.
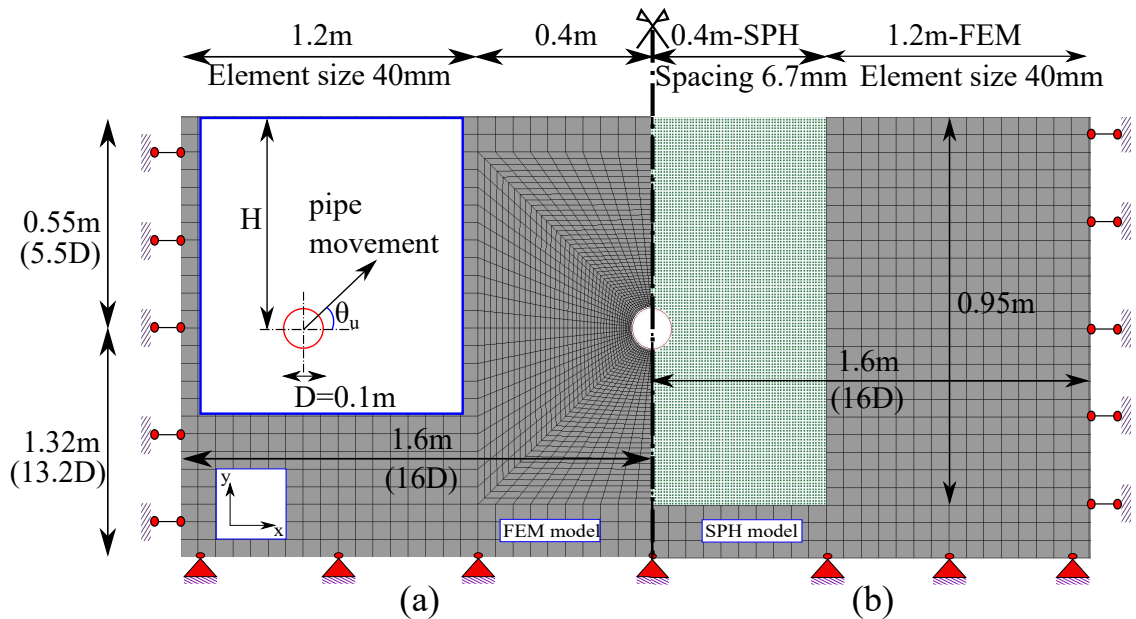
Figure 2.11: Geometry of the numerical models (not to scale): (a) FEM model; and (b) SPH model.

2.4.2 Smoothed-particle hydrodynamics

SPH is a mesh-free particle method based on the Lagrangian formulation. The problem domain is discretized into a set of arbitrarily distributed particles without connectivity. Possessing material properties, these particles represent the state of the system (e.g., density, velocity) and move accordingly to the governing conservation equations. The state function and its derivatives in continuous form are written as integral representation, which subsequently is approximated by summation of the neighboring particles. Interested readers can refer to *Liu and Liu* (2010).

SPH is a mesh-free approach by nature, and hence does not suffer from mesh distortion as in FEM for problems that involve large displacements, at the expense of computational efficiency. To take advantage of both SPH and FEM approaches, the soil domain near the pipe (large deformation region) was simulated with SPH particles, whereas the far-field soil domain (small deformation region) and the pipe were modeled by FEM. The element type and input parameters for FEM pipe and FEM soil were identical with those of the FEM model. The elastic-perfectly plastic constitutive model with Mohr–Coulomb failure criterion used for FEM soil also was used for the SPH soil particles.

The interface between FEM soil and SPH soil particles should guarantee displacement compatibility. A tied-nodes-to-surface-constrained-offset contact was used to constrain the SPH soil particles to move with FEM soil element surfaces. Another interface between the SPH soil particles and the FEM pipe was represented by automatic-nodes-to-surface contact. This contact allows separation and sliding between slave nodes (SPH soil particles) and master surface (FEM pipe surface). The sliding obeyed the Coulomb's friction law with the contact friction angle being $0.6\phi'_{crit}$. Fig. 2.11(b) shows the geometry mesh and boundary conditions of the SPH model. The boundary conditions and the loading phases were exactly the same as those imposed on the FEM model.

The smoothing Kernel function chosen was the cubic B-spline, which is the most commonly used by the SPH community. It is defined for a 3D problem as

$$W(R, h) = \frac{1}{\pi h^3} \begin{cases} 1 - \dfrac{3}{2}R^2 + \dfrac{3}{4}R^3 & 0 \leq R < 1 \\ \dfrac{1}{4}(2 - R)^3 & 1 \leq R < 2 \\ 0 & R \geq 2 \end{cases} \tag{2.15}$$

where h is the smoothing length; and $R = d_{ij}/h$, where d_{ij} is the distance between two particles. The constant applied to smoothing length was $\kappa_{SPH}h = 1.2h$. The renormalized formulation (FORM = 1) was chosen for particle approximation theory. More details of the SPH method in LS-DYNA were given by *Hallquist* (2006).

2.4.3 Validation of the FEM and SPH models

Fig. 2.12 shows the relation between normalized force $F_x/(\gamma_s HDL)$ and normalized relative displacement u_x/D, obtained from Test 20, the FEM model, and the SPH model. The FEM model validation for dense sand in Tests 22, 23, 24, 25, and 32 also is displayed. The constitutive model with strain softening behavior for dense sand used for this set of simulations was described by *Nguyen and Asimaki* (2018), and is not presented here. Clearly, there was good agreement, which proves the fidelity of the numerical simulations.

The FEM and SPH models for Test 20 subsequently were used to generate FDCs F_x - u_x and F_y - u_y for different pipe-loading patterns to verify the proposed BMBW model.
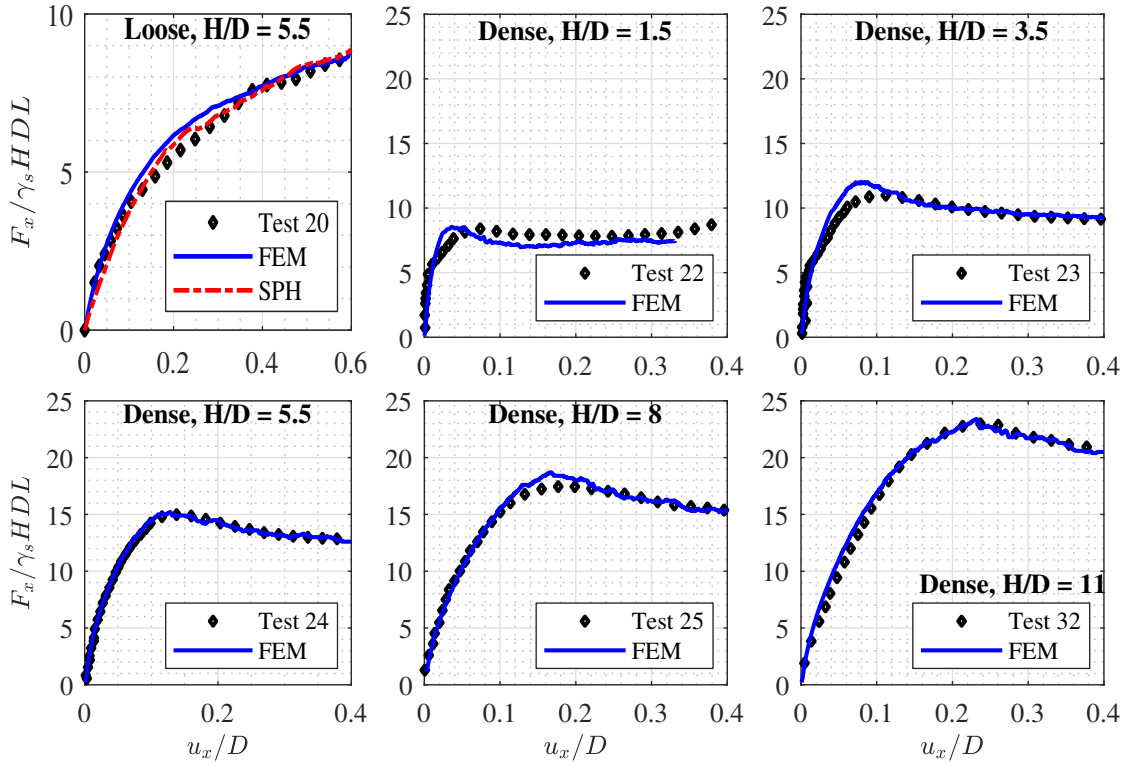
Figure 2.12: Validation of FEM and SPH models.

2.4.4 Parameter calibration for BMBW model

For the physical quantities, $\alpha = 0$, as mentioned previously, and $c = 0.25$, as suggested by *Varun and Assimaki* (2012). K_x, K_{y1}, K_{y2}, F_{ux}, F_{uy1}, and F_{uy2} were calibrated by performing FEM simulations of a pipe moving monotonically along three directions. The soil springs stiffness for the ASCE bilinear model also was chosen from the same FEM results. They were taken as the secant stiffness K_{70x}, K_{70y1}, and K_{70y2}, which corresponds to 70% of the ultimate forces. Fig. 2.13 shows the values of K_x, K_{y1}, and K_{y2} for the BMBW model, and K_{70x}, K_{70y1}, and K_{70y2} for the ASCE bilinear model. F_{ux}, F_{uy1}, and F_{uy2} were identical for both models. As shown in Fig. 2.13(d), in the FEM simulation of the lateral test, while the pipe was pushed laterally without being constrained along the y-axis, $F_y = 0$ and the pipe was moving obliquely with respect to the x-axis. $\chi_0 \approx -15°$.

For the parameters that control the shape of the hysteresis loop, κ was chosen from Fig. 2.4 as a function of the sand relative density and pipe embedment ratio. As mentioned previously, one value of κ is sufficient for all pipe-loading directions in 2D SPI problems. Here, β and γ
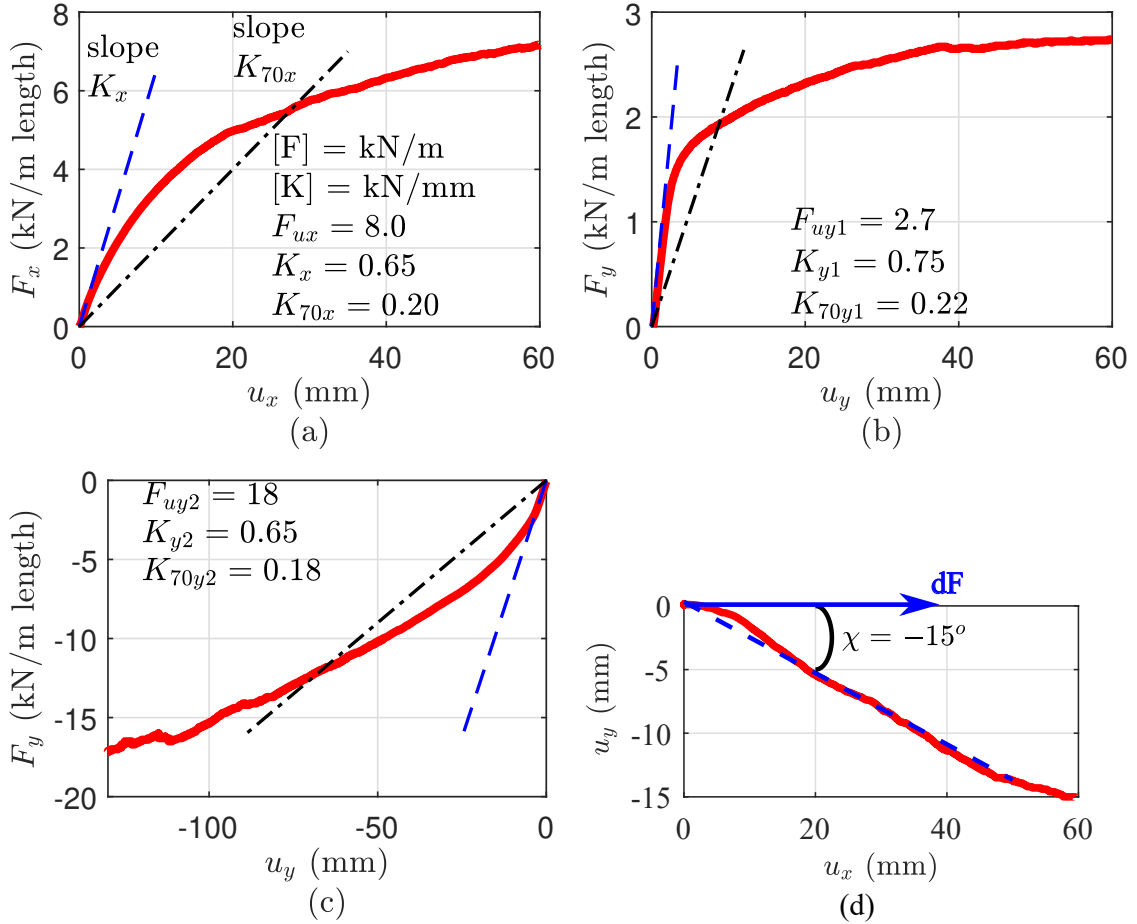
Figure 2.13: Calibration from numerical results: (a) lateral loading; (b) upward vertical loading; (c) downward vertical loading; and (d) pipe trajectory in lateral loading for χ_0.

were taken so that $\beta + \gamma = 1$, $\beta > 0$, and $\gamma > 0$. Furthermore, to ensure the physical rationality, for example, that maximum loads do not exceed the ultimate value or that soil stiffness decreases as the degree of nonlinearity increases, the following conditions were imposed: $\beta \in [0, 0.5]$, and $c \in [\beta/2, \beta]$ (*Varun and Assimaki*, 2012).

For the pinching-control parameters, $\delta_s = 0.150$ and $\sigma = 0.050$ were chosen.

The input parameters that we used for the proposed BMBW model and ASCE model are listed in Table 2.2. These parameters were used consistently for all cases of pipe loading in the subsequent sections. Eq. (2.14) is a stiff differential equation for which some explicit time integration methods give numerically unstable results. The implicit time integration methods generally give better results. In this study, under displacement-controlled loading, the implicit trapezoidal rule was used to solve the system of equations.

Model	Parameter	Value
BMBW	K_x	0.65
	K_{y1}	0.75
	K_{y2}	0.65
	F_{ux}	8.0
	F_{uy1}	2.7
	F_{uy2}	18.0
	α	0
	c	0.25
	χ_0	-15.0
	κ	1.88
	β	0.4
	γ	0.6
	δ_s	0.150
	σ	0.050
ASCE	K_{70x}	0.20
	K_{70y1}	0.22
	K_{70y2}	0.18
	F_{ux}	8.0
	F_{uy1}	2.7
	F_{uy2}	18.0

[Stiffness] = kN/mm, [Force] = kN/m length,

[χ_0] = deg, others are dimensionless

Table 2.2: Input parameters for the proposed BMBW model and ASCE model.

2.4.5 Uniaxial cyclic loading

The pipe was pushed cyclically along one direction that was inclined at an angle θ_u relative to the x-axis (Fig. 2.11). In this case of loading, loading or unloading takes place concurrently along two directions. The pipe displacement was a 3-cycle sinusoidal signal, $u = u_n \sin(2\pi t/10)$, where u_n is the amplitude, t is the time (0–30 s), $\theta_u = \{0, 30°, 45°, 60°, 90°\}$, and $u_n/D = \{0.1, 0.3\}$. The soil experienced weak nonlinearity when $u_n/D = 0.1$, whereas it experienced strong nonlinearity when $u_n/D = 0.3$.

Figs. 2.14, 2.15, 2.16, and 2.17 present the results of BMBW, FEM, SPH, and the ASCE-recommended bilinear method. Overall, the FEM and SPH results agreed well with each other and jointly showed that the FDCs were indeed smooth, nonlinear curves. The ASCE bilinear method generated straight lines with slopes K_{70}. The proposed BMBW method

produced true smooth curves which adequately matched those of the numerical simulations.

Finch (1999) conducted a centrifuge experiment showing typical patterns of the FDC for vertical cyclic loading, as shown in Fig. 2.1. The loading, unloading, and reloading phases jointly create a hysteresis loop. The pinching phenomenon only appears during the unloading phase because the gap forms only below the pipe. The FDCs obtained from FEM and SPH in Figs. 2.14, 2.15, 2.16, and 2.17 clearly depict the hysteresis loops and pinching phenomenon. In those figures, the BMBW method is capable of generating both the loops and pinching zones, in contrast to the ASCE-recommended bilinear method.
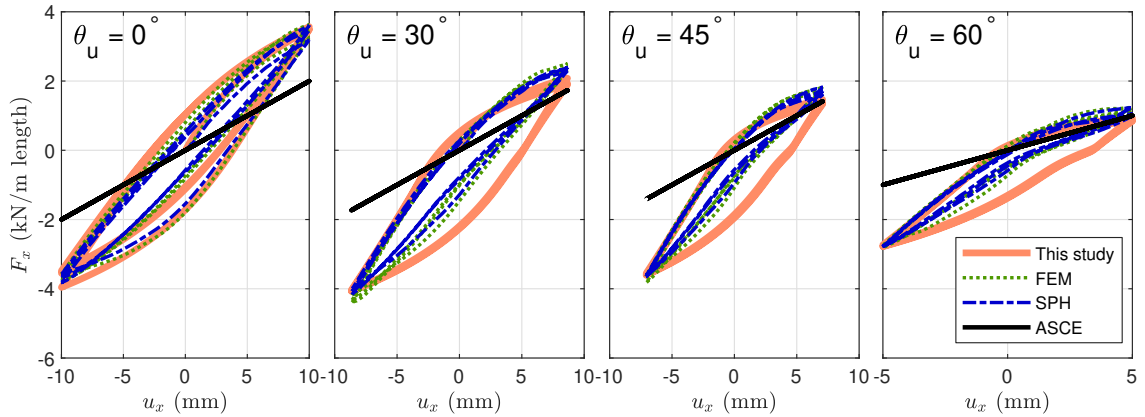
Figure 2.14: F_x - u_x for small pipe displacement $u_n/D = 0.1$.
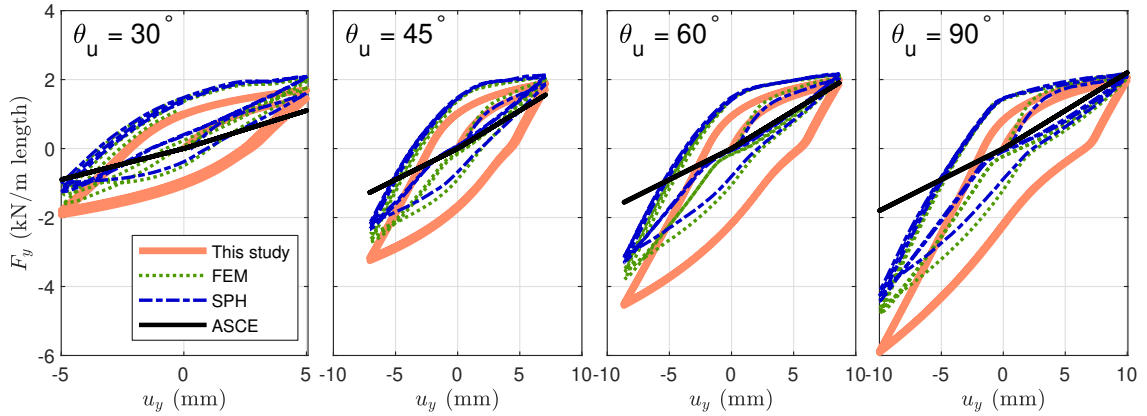
Figure 2.15: F_y - u_y for small pipe displacement $u_n/D = 0.1$.

In general, the pinching is clearer along the y-axis than along the x-axis. Specifically, the pinching length in the F_y - u_y curves is larger than that in the F_x - u_x curves (Figs. 2.14, 2.15, 2.16, and 2.17). The reason is obvious: the gap between pipe and soil causing pinching is due to gravity, which acts vertically. On the x-axis, when $\theta_u = 0°$, there is no pinching,
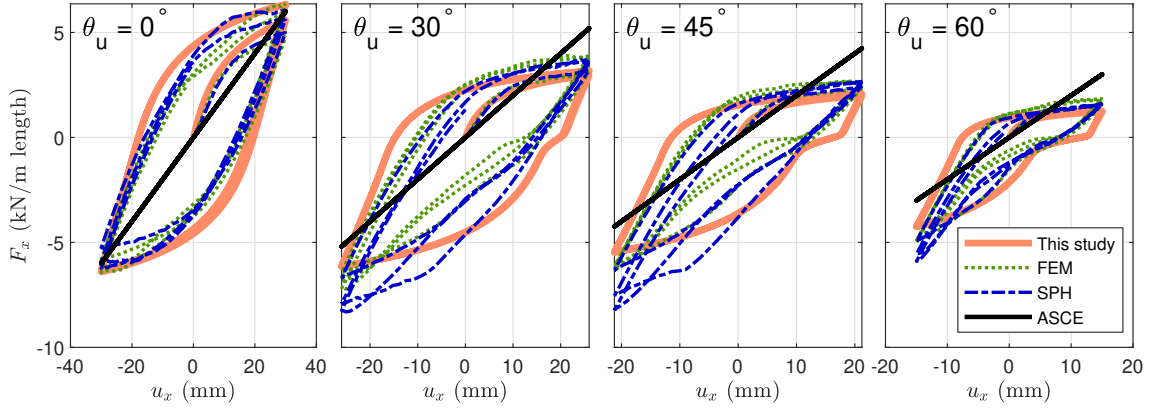
Figure 2.16: F_x - u_x for large pipe displacement $u_n/D = 0.3$.
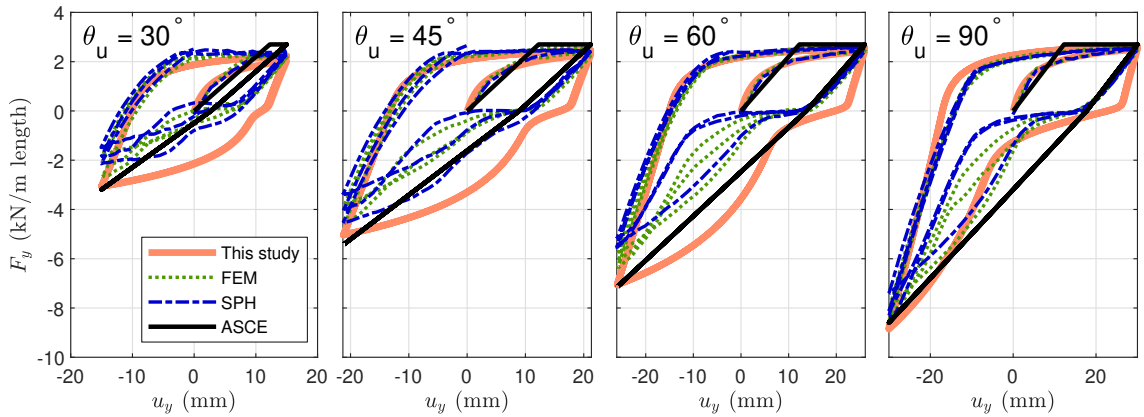
Figure 2.17: F_y - u_y for large pipe displacement $u_n/D = 0.3$.

as shown in Figs. 2.14 and 2.16. When $\theta_u = 30°$, $45°$, and $60°$, the pinching occurs. The appearance of pinching is attributed to the effect of u_y, demonstrating the coupling effect between vertical and horizontal directions. For both F_x - u_x, F_y - u_y, the pinching length increases with displacement u_n and angle θ_u. The BMBW results captured this trend well.

Whereas the secant stiffness and ultimate reaction force in the ASCE uncoupled bilinear model remained unchanged, FEM and SPH results showed that they indeed change depending on θ_u. Taking F_x - u_x in Fig. 2.16 as an example, the ultimate reaction forces were about 8, 4, 3, and 2 kN/m when $\theta_u = 0°$, $30°$, $45°$, and $60°$, respectively. The BMBW had similar results as the numerical simulations, indicating that it captures the coupling when the pipe moves obliquely.

Additionally, the coupling effect between two directions is illustrated by drawing the lateral uplift failure envelope, as in Fig. 2.18, in which $F_{ux\theta}$ and $F_{uy\theta}$ are the ultimate reaction forces along the x- and y-axes corresponding to pipe movement angle θ_u. These forces are normalized by the ultimate reaction forces corresponding to purely lateral and uplift

pipe movements, F_{ux0} and F_{uy90}. When the inclination angle θ_u increased, the ultimate normalized horizontal reaction forces decreased and the vertical reaction forces increased, indicating the coupling effect of pipe displacements in the lateral and vertical directions. The envelope of the proposed BMBW method was close to that of the FEM simulations. The analytical results of *Nyman* (1984), and the FEM results of *Guo* (2005) and *Daiyan* (2013) also are plotted in Fig. 2.18 for comparison.
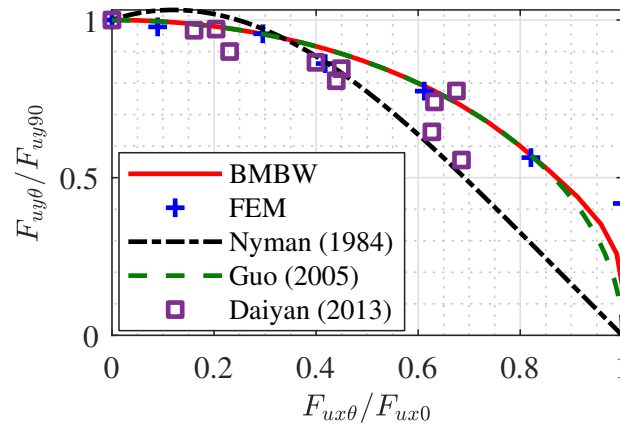
Figure 2.18: Lateral uplift failure envelope.

2.4.6 0-Shaped loading

In 0-shaped loading, as shown in Fig. 2.19(a), the loading phase occurs in one direction and the unloading phase occurs in another direction. Because the lateral displacement usually is dominant over the vertical displacement in earthquakes, two ratios of displacement amplitude were considered, namely $u_y/u_x = 0.25$ and 0.5. The displacement amplitude along the x-axis is u_n, where $u_n/D = 0.1$ and 0.3.
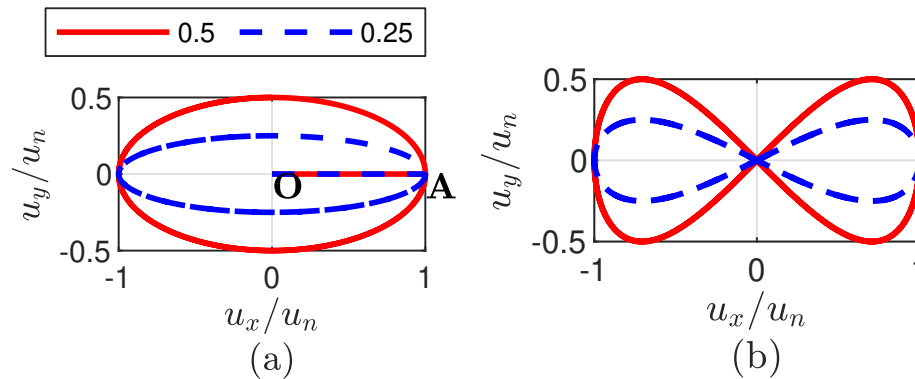
Figure 2.19: Cyclic displacement loading patterns: (a) 0-shape loading; and (b) 8-shape loading.

Again, in Figs. 2.20 and 2.21, contrary to the oversimplified bilinear ASCE model, the BMBW produced smooth nonlinear curves and captured the dissipated energy via hysteresis loops. The areas of hysteresis loops were narrow for $u_n/D = 0.1$ and fatter for $u_n/D = 0.3$, indicating that more energy is dissipated for higher degree of soil nonlinearity.
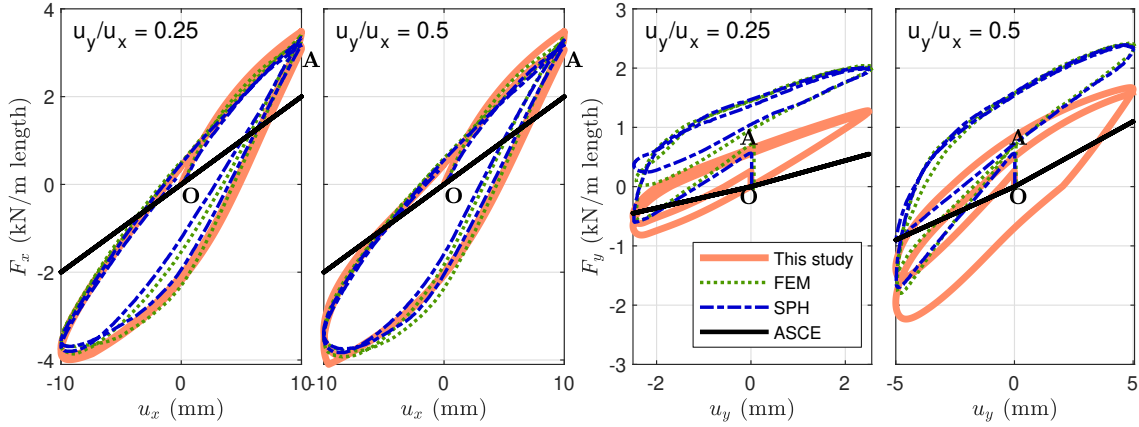
Figure 2.20: F_x - u_x and F_y - u_y for 0-shape loading and small pipe displacement $u_n/D = 0.1$.
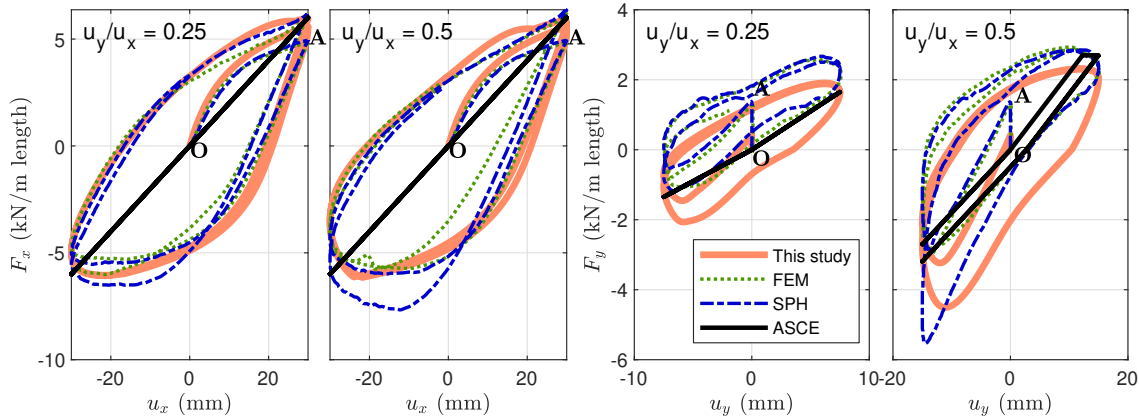
Figure 2.21: F_x - u_x and F_y - u_y for 0-shape loading and large pipe displacement $u_n/D = 0.3$.

When the pipe was pushed horizontally along branch OA in Fig. 2.19(a), the ASCE method predicted $F_y = 0$, whereas the FEM, SPH, and BMBW results were non-zero values for F_y (hysteresis loop branch OA in Figs. 2.20 and 2.21). The F_y value of the BMBW was different from that of the FEM and SPH models because the simplified assumed function for $\chi(f_\zeta, \theta_{du})$ does not exactly capture the variation of χ in numerical simulations. However, the difference is acceptable considering the simplicity and computational efficiency that the BMBW offers while reproducing the trend of F_y - u_y.

In Figs. 2.20 and 2.21, as u_y/u_x increases from 0.25 to 0.5, the corners of F_x - u_x become rounder, namely the effect of u_y on u_x becomes increasingly noticeable. In addition, when

u_n increases, the coupling effect is more pronounced. This is indicated by the rounder corners of F_x-u_x and F_y-u_y curves in Fig. 2.21 compared with the corresponding corners in Fig. 2.20.

2.4.7   8-Shaped loading

In 8-shaped loading, as displayed in Fig. 2.19(b), both loading and unloading along the y-axis occur in either loading or unloading along the x-axis. Figs. 2.22 and 2.23 show results for $u_n/D = 0.1$, 0.3 and $u_y/u_x = 0.25$, 0.5. Similar to the case of 0-shaped loading, the hysteresis loops were thinner for $u_n/D = 0.1$ and fatter for $u_n/D = 0.3$. This reconfirms that energy dissipation increases with the degree of soil nonlinearity. Moreover, when u_y increased, it increasingly affected F_x-u_x, creating a bulkier hysteresis loop. The FDC predicted by the BMBW model was in good agreement with the results of FEM and SPH.
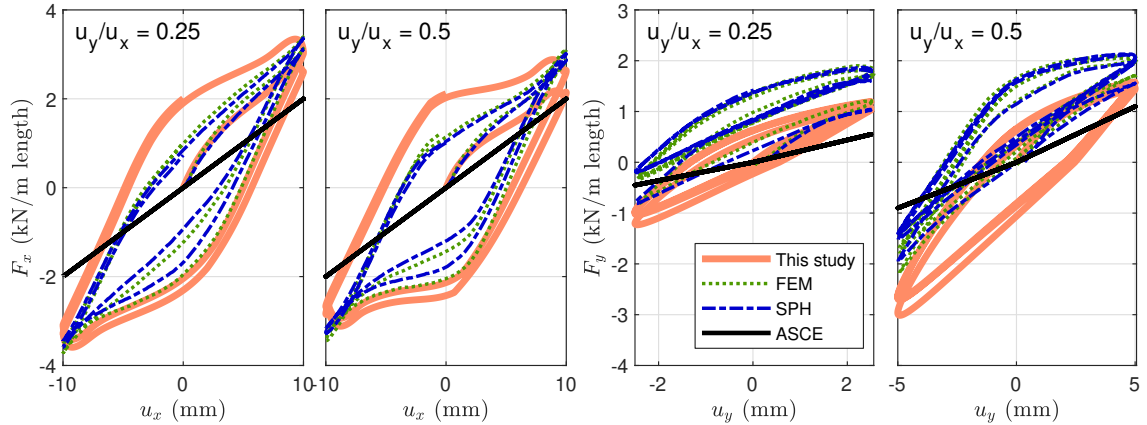
Figure 2.22: F_x-u_x and F_y-u_y for 8-shape loading and small pipe displacement $u_n/D = 0.1$.
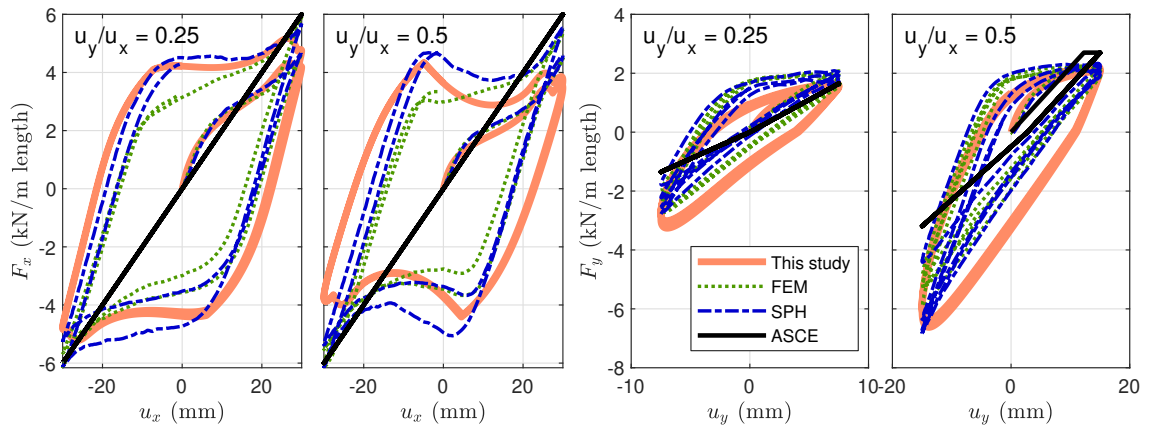
Figure 2.23: F_x-u_x and F_y-u_y for 8-shape loading and large pipe displacement $u_n/D = 0.3$.

In Fig. 2.23, there are two points at the corners of F_x-u_x, and one point at $F_y = 0$ of F_y-u_y

where the slope of FDC becomes discontinuous. This occurs because at those points, ζ_y switches between positive and negative values, leading to changes in F_{uy} and K_y, as in Eq. (2.14). Subsequently, this causes discontinuities in $\dot{\zeta}_x$ and $\dot{\zeta}_y$. This is inevitable when F_{uy1}, K_{y1} and F_{uy2}, K_{y2} are combined into one single spring. Nevertheless, the discontinuities vanish when $F_{uy1}/K_{y1} = F_{uy2}/K_{y2}$. Furthermore, this happens only at isolated points on the FDC and does not affect the general trend of F_x - u_x and F_y - u_y.

2.4.8 Transient loading

The reaction force of the soil acting on the pipe was investigated for the case of biaxial transient loading. The 1995 Kobe earthquake M_W 6.9 ground motions at OSAJ station, 8.5 km from the fault rupture, were used for this purpose (*Ancheta et al.*, 2013). Fig. 2.24 shows the time histories and pattern of displacement. The lateral displacement was dominant, with a peak value of 88 mm, whereas the peak vertical displacement was 23 mm. The SPH method was chosen for the reference simulations to appropriately model large displacement of the pipe. Fig. 2.25 compares the response time histories F_x - t and F_y - t predicted using the BMBW, SPH, and ASCE bilinear model. The proposed BMBW method captured the responses obtained by SPH to a high degree of accuracy. In contrast, the ASCE model tended to overestimate the F_x in regions of large lateral displacement and ignored the coupling effect. Accordingly, F_y was considerably different from the values predicted by SPH and BMBW. Fig. 2.26 shows the FDCs F_x - u_x and F_y - u_y estimated using the aforementioned three methods. Clearly, the shape of FDC from the BMBW matched well that from SPH, with round corners expressing the coupling between lateral and vertical directions.
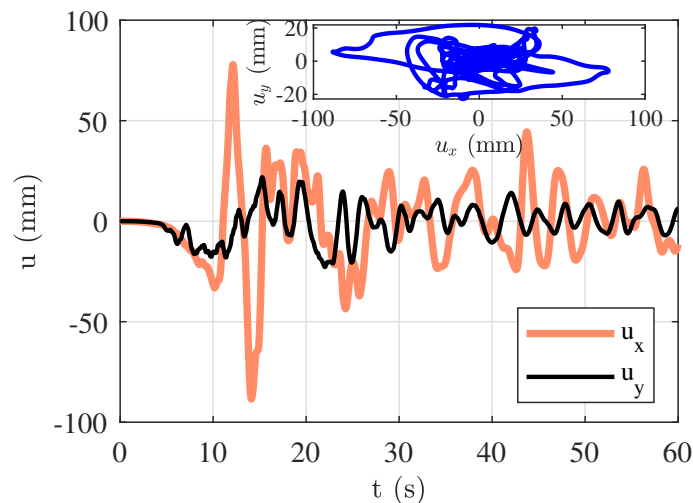
Figure 2.24: Kobe earthquake signal.
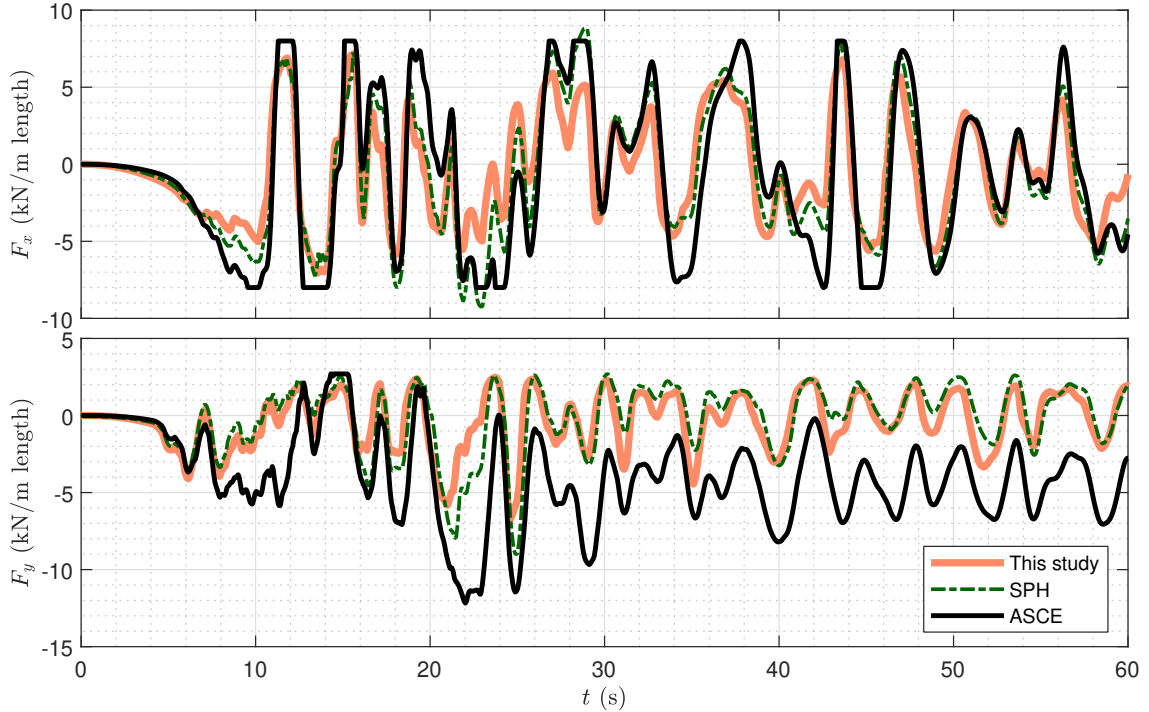
Figure 2.25: F_x - t and F_y - t from BMBW, SPH, and ASCE model for Kobe earthquake.

2.4.9 Suggestions for input parameters

In general, the input parameters for the proposed BMBW methods are suggested as follows:

1. $\alpha = 0$.

2. K_x, K_{y1}, K_{y2}, F_{ux}, F_{uy1}, and F_{uy2} are chosen by performing simple FEM simulations as in the preceding section. Alternatively, *ASCE* (1984) provides formulas to calculate F_{ux}, F_{uy1}, and F_{uy2}. It also provides the hyperbolic form of the FDC $F = u/(A + Bu)$ where A and B are case-specific coefficients for lateral, vertical uplift, and vertical downward pipe movements. Therefore, the initial soil stiffness K_x, K_{y1}, K_{y2} can be estimated as $(\partial F/\partial u)|_{u\to 0} = 1/A$.

3. $c = 0.25$, as suggested by *Varun and Assimaki* (2012).

4. χ_0 can be chosen from FEM simulations or experimental data. The authors used FEM simulations to generate χ_0 for practical design purposes. The FEM models were conducted for dense, medium, and loose sands, whose direct shear test peak friction angle and relative density were $\phi'_{ds-p} = 44°$, $36°$, and $31°$ and $I_D = 80\%$, 45%, and 0%, respectively. The embedment ratio H/D ranged from 1.5 to 11. The results are shown in Fig. 2.27.
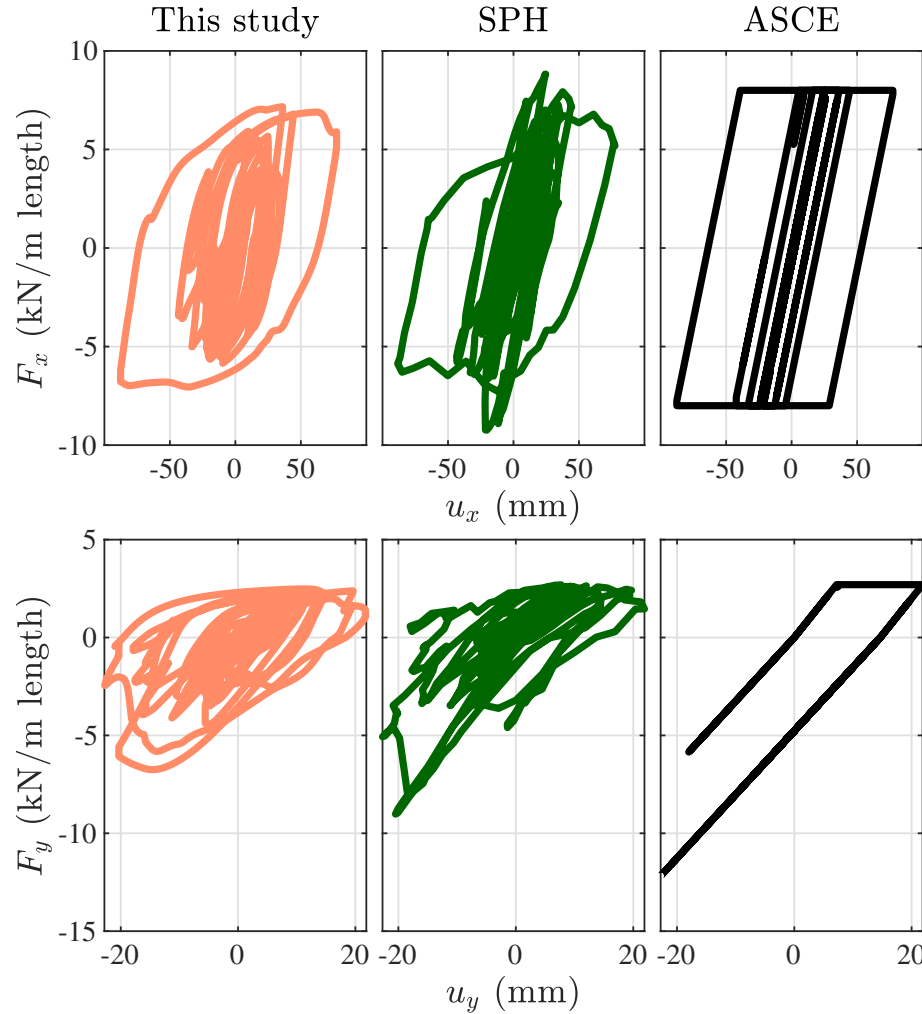
Figure 2.26: F_x - u_x and F_y - u_y from BMBW, SPH, and ASCE model for Kobe earthquake.

5. κ is taken from Fig. 2.4.

6. β and γ satisfy the equality $\beta + \gamma = 1.0$. The general shape of the hysteresis loop is not very sensitive with respect to β and γ. Normally, $(\beta, \gamma) = (0.5, 0.5)$ or $(\beta, \gamma) = (0.4, 0.6)$ is suggested.

7. δ_s and σ are case-specific parameters. They can be calibrated from cyclic experimental data or simple FEM simulations for cyclic loading. The FEM models also were used to generate the FDCs for cyclic vertical loading; for example, F_y - u_y for $\theta_u = 90°$ in Fig. 2.17 was predicted by the FEM model for loose sand with $H/D = 5.5$. Values of δ_s and σ then were derived by fitting F_y - u_y curves of the proposed BMBW method to those of the FEM models. The results are shown in Fig. 2.28. When no cyclic experiment data or FEM simulations are available, using δ_s and σ from Fig. 2.28 can
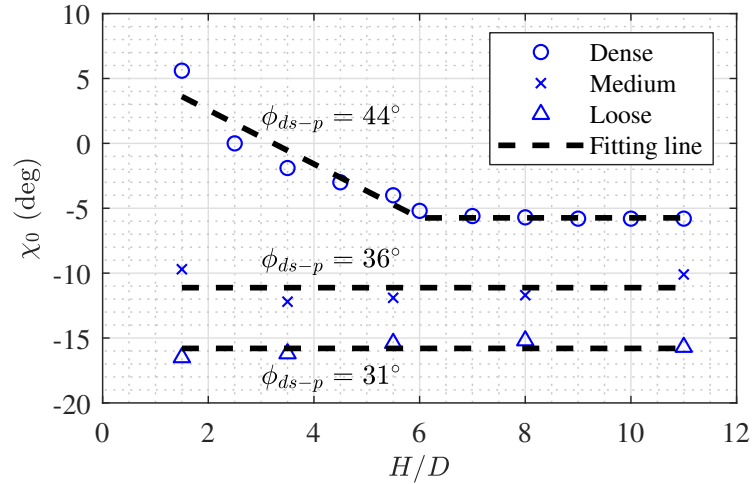
Figure 2.27: χ_0 for various embedment ratios H/D and sand types.

provide a good first approximation.
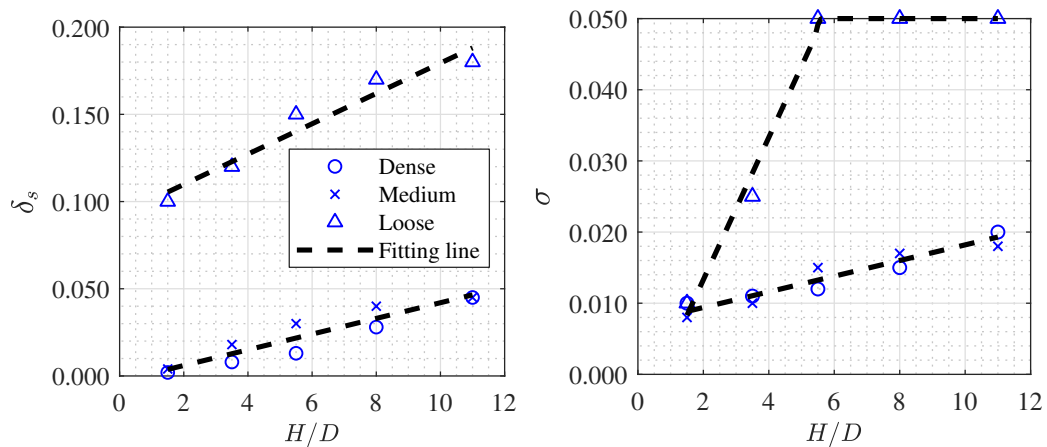
Figure 2.28: δ_s and σ for various embedment ratios H/D and sand types.

2.5 Conclusions

This chapter presents a mechanics-based reduced-order method to capture SPI under biaxial loading on a 2D vertical plane. Unlike the most widely used ASCE bilinear model, this novel method is able to take into consideration the true smooth nonlinearity, the hysteresis loop, pinching phenomenon, and the coupling between lateral and vertical displacement. Results of the proposed method showed great agreement with those of numerical simulations by FEM and SPH. In summary, our study showed/confirmed that

1. For loose and medium sand, $\kappa = 0.5$–2.2, and for dense sand, $\kappa \approx 0.0$; κ follows

the same variation with H/D and relative density for both lateral and uplift pipe displacement.

2. Hysteresis is more pronounced for higher degree of soil nonlinearity (large pipe displacement).

3. Pinching mainly occurs in F_y-u_y due to gravity. Similar behavior in F_x-u_x results from the effect of coupling.

4. Coupling becomes more pronounced for larger displacement amplitude.

Despite some limitations, namely the applicability for rigid (or nearly rigid) pipe, and the inability to capture the post-peak behavior of FDC, this study is a first step toward building a reduced-order 3D hysteresis model to incorporate soil springs along lateral, vertical, and longitudinal directions of pipeline-soil interaction models. Our work will provide a tool to investigate cyclic/dynamic SPI, which we envision integrating in large-scale soil-structure interaction models.

Dynamic axial soil impedance function for rigid circular structures buried in elastic half-space

Contents of this chapter

3.1 Introduction

The spatial distribution of underground buried structures, such as tunnels, pipelines, and culverts, makes them more prone to seismic damage induced by geohazards. It is therefore critical to accurately quantify dynamic soil-buried structure interaction (SbSI) effects in designing earthquake-resistant structures. Generally, seismic analyses of SbSI are carried out by either a fully three-dimensional simulation (direct method) or a reduced-order model (substructure method). The highly computational cost of direct method hinders it from routine use for deterministic and especially stochastic design procedures. Meanwhile, the reduced-order model is computationally effective and has been extensively used over the years by many researchers and structural design codes. State-of-the-art reduced-order SbSI models of buried structures are based on the theory of beam on dynamic Winkler foundation, where the soil surrounding the structure is replaced by a set of springs and dashpots (aka SIFs) formulated to represent its macroscopic reaction to differential deformations between soil and structure. In such a method, estimation of SIF (spring stiffness and dashpot damping coefficient) is a top priority, which significantly affects the computation of internal loads and design of the buried structures (*Pitilakis and Tsinidis*, 2014).

Since the 1960s, quite a number of studies have been carried out to investigate the dynamic SIF of different types of foundation. For example, *Karasudhi et al.* (1968); *Luco and Westmann* (1972); *Gazetas* (1980); *Hryniewicz* (1981) studied the dynamic response of a surface rigid strip foundation (Fig. 3.1a), while *Rajapakse and Shah* (1988); *Israil and Ahmad* (1989); *Ahmad and Bharadwaj* (1991); *Bharadwaj and Ahmad* (1992) examined the dynamic behavior of embedded rigid strip foundation (Fig. 3.1b). *Novak et al.* (1978); *Novak and Aboul-Ella* (1978); *Padrón et al.* (2012); *Goit and Saitoh* (2013), meanwhile, derived the SIF for pile foundation (Fig. 3.1c) in homogeneous and layered soil domain. Nevertheless, the SIFs for spatially distributed buried structures (Fig. 3.1d) have not been properly addressed until now, even in the current guidelines of the American Society of Civil Engineers (*ASCE*, 1984), the American Lifeline Alliance (*ALA*, 2005), the European Committee for Standardization (*CEN*, 2006), and the Pipeline Research Council International (*PRCI*, 2009). Due to this lack of information, throughout the years, many researchers have to use rough estimation of SIF in their reduced-order models when dealing with SbSI problems. *Hindy and Novak* (1979); *Datta and Mashaly* (1986, 1988) used approximation method, which is a combination of the static solution by *Mindlin* (1964) with the dynamic plane-strain solution by *Novak et al.* (1978) to derive SIF in their lumped-mass models for underground pipelines. Or in the development of an analytical solution to estimate the upper bounds of stresses and strains for soil-pipeline interaction, *Mavridis and Pitilakis* (1996) used directly the dynamic SIF originally for pile foundation. Recently, when performing

the risk assessment of the pipeline network under earthquake scenario, the SIF is chosen as static stiffness following the American Lifelines Alliance guideline (e.g., *Lee et al.*, 2009; *Nourzadeh and Takada*, 2013; *Saberi et al.*, 2013), or as static stiffness of a long rectangular tunnel (e.g., *Anastasopoulos et al.*, 2007), or obtained as a frequency-independent constant (e.g., *Hsu*, 2020). Most, if not all, of the mentioned work, ignores the dynamic nature of
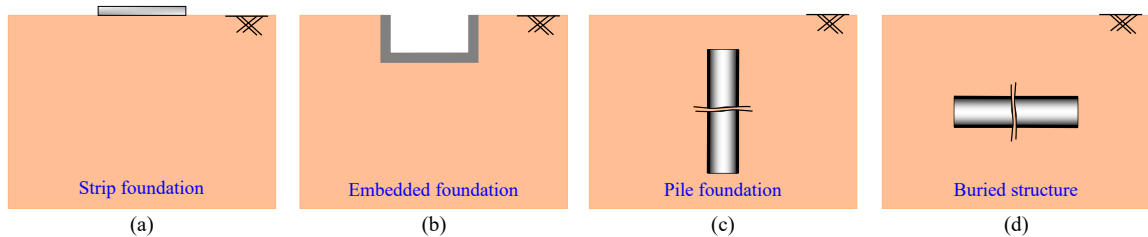
Figure 3.1: Schematics of: (a) strip foundation; (b) embedded foundation; (c) pile foundation; and (d) buried structure.

seismic loading, and resorts to frequency-independent SIFs that cannot account for transient differential strains induced by wave passage effects (e.g., surface waves from basin effects). Besides, a small number of recent studies (*Seylabi et al.*, 2016; *Seylabi*, 2016) have showed that in SSI problems of buried structures, frequency dependency of SIF is more important than in the case of either shallow or deep foundations, because the free surface distorts the path of radiated energy away from the vibrating tunnel or pipeline (Fig. 3.2).

Although the axial strain is dominant in buried structures response, very little research has been done to determine the dynamic axial SIF for this type of structure. Some experiments were done in the past to study dynamic axial response of underground structures during seismic ground motion (e.g., *Sakurai and Takahashi*, 1969; *Nasu et al.*, 1974), but almost no information about soil spring stiffness or dashpot damping coefficient was drawn from these experiments. *Colton et al.* (1982) conducted dynamic tests to measure the soil-pipe axial interactions in sand backfill at frequencies from 0.1 to 12 Hz. Their results were then used by *El Hmadi and O'Rourke* (1988) to back-calculate the axial soil spring stiffness via a pseudo-static model. Lately, *Liu et al.* (2018) proposed an experimental method to obtain the axial soil spring stiffness of ductile cast iron and welded steel pipes through artificial earthquake. Generally, all mentioned work only focused on axial soil spring stiffness, although the results are sparse, while neglecting the dashpot damping coefficient.

In an attempt to find the analytical solution for axial SIF of infinitely long circular hole in half-space soil domain, *Matsubara and Hoshiya* (2000) solved a Neumann boundary condition problem, with stress p applied at the hole circumference and the approximate displacement calculated by averaging the displacement of nodes around the circumference. While the
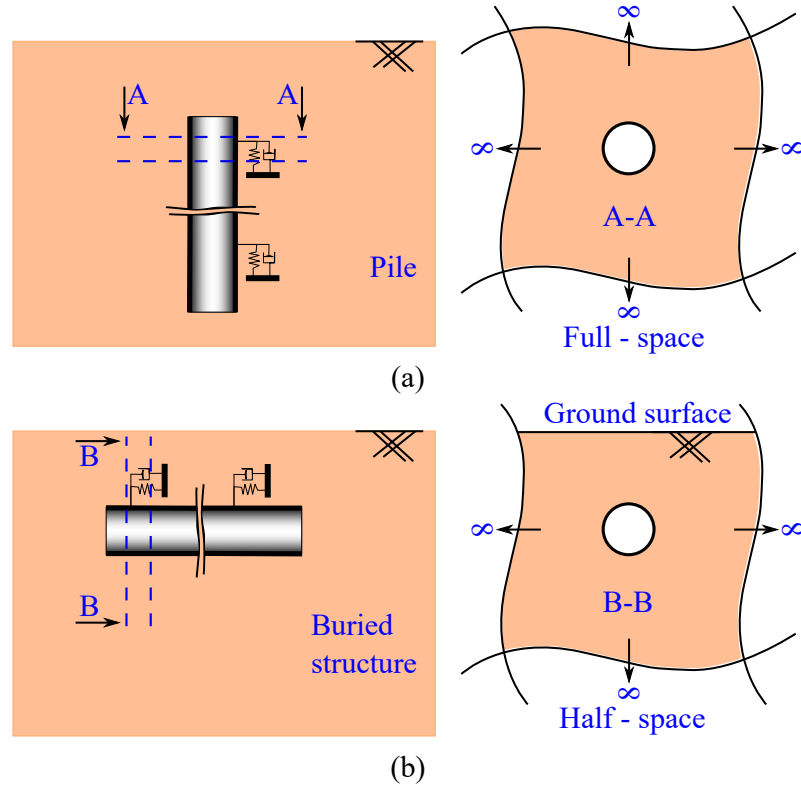
Figure 3.2: Geometry to compute SIF of a cross section: (a) full-space for pile foundation; and (b) half-space for buried structure.

stress boundary conditions at free surface (traction free) and at the hole circumference (pressure p) are satisfied, the displacement of nodes around the hole circumference is unconstrained. It means that the nodes at the interface are able to move freely, and as a result, the stiffness of the pipe is not taken into account. This underlying assumption is not physically appropriate, because the soil particles at the circumference and the pipe usually conform to each other, especially in small displacement regime. Moreover, the relatively high stiffness of the structure with respect to the near-surface soil (which is usually soft soil) making the assumption of rigid buried structures is more appropriate. Besides, the analytical solution of *Matsubara and Hoshiya* only considers the participant of the first mode shape by using the second kind of Hankel's function of only zero order $H_0^{(2)}(kr_1)$.

It appears necessary to obtain an analytical solution which is mathematically exact for axial SIF of spatially distributed buried structures. This solution should precisely account for the energy reflected from the soil free surface and yield constant displacement around the structure boundary. It is also important to build a high-fidelity numerical model to estimate SIF, which can be generalized to any geometry of underground structure or soil strata. In this chapter, we devised an analytical solution for dynamic axial SIF of rigid cylinder buried

in homogeneous elastic half-space by solving a mixed-boundary-value problem, in which the displacement is prescribed at the circular buried structure boundary and traction-free condition is satisfied at the soil free surface. We further used FE analyses to accurately extract the axial SIF of rigid cylinder in homogeneous and two-layered soil half-space. While the work here focuses on the rigid circular interface, the FE approach can apply well to more general shape and flexibility of the underground structures. Finally, we performed the parametric studies to investigate the effects of cylinder burial depth and material contrast on the SIFs of homogeneous and two-layered half-space.

The remainder of this chapter is organized as follows: In Section 3.2, we reviewed some basics of the SIF. In Section 3.3, we derived the analytical solution for homogeneous half-space, using Hankel–Fourier series expansion. We also described the FE modeling procedure to generate SIFs for homogeneous and two-layered half-spaces in Section 3.4. In Section 3.5, we verified the analytical solution and the FE approach by comparing their results with each other. Sections 3.6 and 3.7 present the SIFs and the effect of cylinder burial depth on SIFs in case of homogeneous and two-layered half-space, respectively. The effect of material contrast also was investigated in two-layered half-space. Concluding remarks were provided in Section 3.8.

3.2 Review of axial soil impedance function

An important step to evaluate the SbSI is to calculate the SIF for the "associated" massless structure as a function of frequency. The associated structure is identical to the actual one in terms of geometry and material properties, but has no mass. Technically, the SIF is a Dirichlet-to-Neumann mapping function, which relates the displacements (at soil-structure interface) and the interacting forces that soil domain exerts on the structure.

For a given angular frequency $\omega \in \mathbb{R}^+$ from the steady-state harmonic excitation, the dynamic SIF is defined as the ratio between the force (or moment) and the resulting displacement (or rotation) at the centroid of rigid body (*Gazetas*, 1983). In this work, we focused on the axial impedance $\hat{K}_z$ computed in the frequency domain as follows:

$$\hat{K}_z(\omega) = \frac{\hat{F}_z(\omega)}{\hat{w}(\omega)}, \tag{3.1}$$

where the complex-valued functions $\hat{F}_z(\omega)$, $\hat{w}(\omega) : \mathbb{R} \to \mathbb{C}$ are the applied force and resulting uniform harmonic displacement at the centroid of the soil-structure interface. The real-valued functions $F_z(t)$, $w(t) : \mathbb{R} \to \mathbb{R}$ are their counterparts in the time domain, which are illustrated in Fig. 3.3. Because all the SIFs in this chapter are in frequency domain only, the hat superscript "ˆ" of SIFs is henceforth omitted for simplicity, $\hat{K}_z$ is rewritten as K_z.
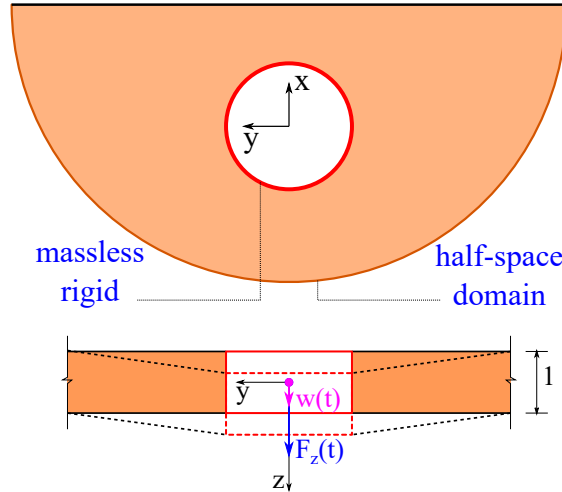
Figure 3.3: The rigid axial displacement.

The soil impedance in Eq. (3.1) is thus a complex-valued function that can be written as $K_z = \Re(K_z) + i\Im(K_z)$, where $i^2 = -1$ is the imaginary unit, $\Re(K_z)$ is the real part representing the mass inertia and stiffness, and $\Im(K_z)$ is the imaginary part reflecting the radiational and material damping of the soil domain (*Gazetas*, 1983). The complex value of SIF physically implies that the applied force and the resulting displacement are out of phase.

3.3 Analytical solution for soil impedance function of homogeneous half-space

3.3.1 Assumptions

The following assumptions were employed to obtain the analytical solution for the axial SIF:

- The soil domain is half-space, homogeneous, isotropic, and linear elastic.

- The buried structure (cylinder) is rigid, circular, massless and infinitely long.

- The cylinder and soil medium are fully bonded.

- The displacements are small.
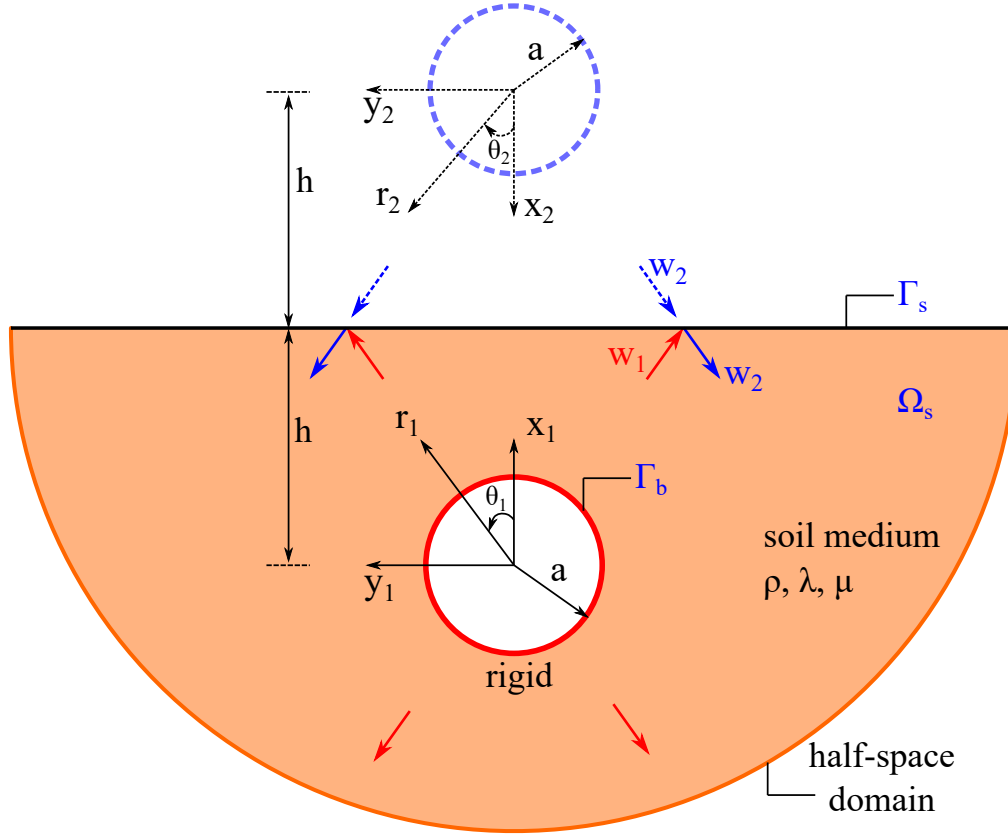
Figure 3.4: The problem geometry.

3.3.2 Governing equation

The governing equation for a general linear elastodynamics problem, in the absence of body forces, is

$$\mu \nabla^2 \boldsymbol{u} + (\lambda + \mu) \nabla (\nabla \cdot \boldsymbol{u}) = \rho \ddot{\boldsymbol{u}} \quad \text{in } \Omega_s, \tag{3.2}$$

where $\Omega_s \subseteq \mathbb{R}^3$ is the soil half-space domain, λ and μ are the Lamé constants, $\boldsymbol{u} : \Omega_s \to \mathbb{R}^3$ is the displacement vector field, and ρ is the mass density of soil medium.

To find the axial impedance, unitary displacement along z-direction $w = e^{i\omega t}$ is imposed on Γ_b, which is the circumference of the rigid cylinder. On Γ_b, $r_1 = a$, where a is the outer radius of the cylinder. Because the polarization of the imposed vibration is parallel to the lengthwise direction of the infinitely long cylinder, the reflected SH wave from the free surface and the scattered SH wave from the cylinder boundary have the same polarization. The problem falls into the category of anti-plane strain, in which only displacement along z-direction w is non-zero, in other words the displacement field $\boldsymbol{u}(u, v, w) = (0, 0, w)$. Using cylindrical coordinate (r_1, θ_1, z) and Cartesian coordinate (x_1, y_1, z) systems as shown in Fig. 3.4, the governing equation and boundary conditions for this particular problem can be

rewritten as

$$\frac{\partial^2 w}{\partial r_1^2} + \frac{1}{r_1}\frac{\partial w}{\partial r_1} + \frac{1}{r_1^2}\frac{\partial^2 w}{\partial \theta_1^2} = \frac{1}{c_\beta^2}\frac{\partial^2 w}{\partial t^2} \quad \text{in } \Omega_s, \tag{3.3}$$

$$\sigma_{xz} = 0 \qquad \text{on } \Gamma_s, \tag{3.4}$$

$$w = e^{i\omega t} \qquad \text{on } \Gamma_b, \tag{3.5}$$

where Γ_s is the soil traction-free surface and $c_\beta = \sqrt{\mu/\rho}$ is the shear wave velocity. On Γ_s, $x_1 = h$, where h is the burial depth of the cylinder.

3.3.3 Solution

For simplicity, the time factor $e^{i\omega t}$ is henceforth omitted. We first consider the case of a full-space problem, where only Eq. (3.3) needs to be satisfied. Using separation of variables in cylindrical coordinate, *Mow and Pao* (1971) proposed the following general solution

$$w_1(r_1, \theta_1) = \sum_{m=0}^{\infty} H_m^{(2)}(kr_1)\left[A_m \cos(m\theta_1) + B_m \sin(m\theta_1)\right], \tag{3.6}$$

where $k = \omega/c_\beta$ is the wave number, A_m and B_m are complex coefficients, and $m \in \mathbb{Z}$ is an integer. Note that the Hankel function of the second kind $H_m^{(2)}(kr_1)$ was used in order to satisfy the Sommerfeld radiation condition because the cylindrical SH waves scatter from the cylinder boundary.

Regarding the half-space problem, the solution is obtained from the full-space solution combined with image technique to satisfy traction-free boundary condition. The imaginary cylinder is symmetric with the actual cylinder with respect to the free surface as shown in Fig. 3.4. The cylindrical SH waves scattering from the imaginary cylinder can be written as:

$$w_2(r_2, \theta_2) = \sum_{m=0}^{\infty} H_m^{(2)}(kr_2)\left[A_m \cos(m\theta_2) + B_m \sin(m\theta_2)\right]. \tag{3.7}$$

The total displacement in the half-space soil domain is thus the superposition $w = w_1 + w_2$, for which w_1 represents the wave scattering from the vibrating cylinder, and w_2 represents the wave reflected from the half-space free surface. The general solution for the half-space problem is

$$w = \sum_{m=0}^{\infty} \left\{ \left[H_m^{(2)}(kr_1)\cos(m\theta_1) + H_m^{(2)}(kr_2)\cos(m\theta_2)\right]A_m + \left[H_m^{(2)}(kr_1)\sin(m\theta_1) + H_m^{(2)}(kr_2)\sin(m\theta_2)\right]B_m \right\}. \tag{3.8}$$

We see that due to the symmetry, at the free surface $w_1 = w_2$ and $\sigma_{xz} = \mu \partial w / \partial x_1 = 0$. The displacement field is uniquely described if the complex coefficients A_m and B_m are obtained.

The boundary condition at the cylinder circumference is used to establish a set of equations with variables A_m and B_m. Because w_1 and w_2 are written with respect to two different coordinate systems, w_2 is transformed from (r_2, θ_2) to (r_1, θ_1). Considering a point Q in the half-space, a geometrical triangle $\triangle QO_1O_2$ with lengths of sides $\{r_1, r_2, 2h\}$ is created. As shown in Fig. 3.5, the triangle $\triangle QO_1O_2$ is scaled by a factor of k, which is the wave number.
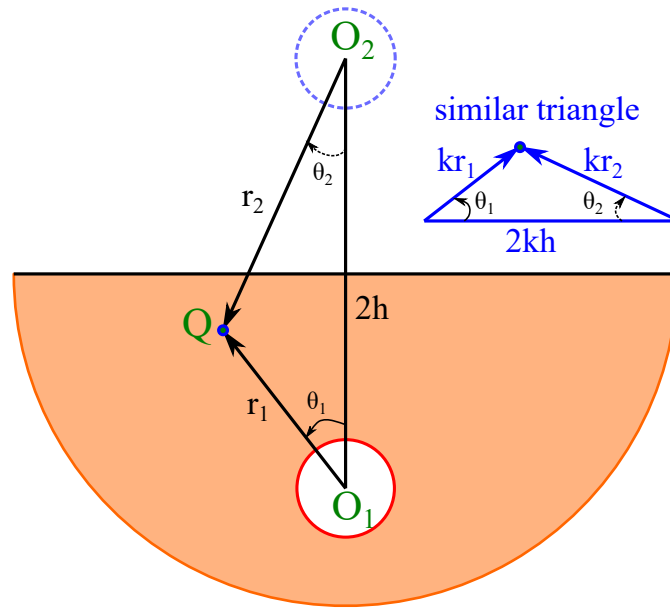
Figure 3.5: Geometry of Graf's addition theorem.

The Graf's addition theorem (*Abramowitz and Stegun*, 1948) is written for this similar triangle as

$$\mathscr{C}_n(kr_2)\, \mathscr{S}(n\theta_2) = \sum_{m=-\infty}^{\infty} \mathscr{C}_{n+m}(2kh)\, J_m(kr_1)\, \mathscr{S}(m\theta_1), \quad \text{for } |kr_1| < |2kh|, \quad (3.9)$$

where $n \in \mathbb{Z}$, $\mathscr{C}_n(\cdot)$ denotes the Bessel function or Hankel function of the first or second kind $J_n(\cdot)$, $Y_n(\cdot)$, $H_n^{(1)}(\cdot)$, $H_n^{(2)}(\cdot)$, or any nontrivial linear combination of these functions, and $\mathscr{S}(\cdot)$ denotes $\sin(\cdot)$ or $\cos(\cdot)$ function. It should be noticed that the theorem holds when $|r_1| < 2h$. From Eq. (3.9), we have

$$H_n^{(2)}(kr_2)\, \mathscr{S}(n\theta_2) = \sum_{m=-\infty}^{\infty} H_{n+m}^{(2)}(2kh)\, J_m(kr_1)\, \mathscr{S}(m\theta_1). \quad (3.10)$$

With $J_{-m}(kr_1) = (-1)^m J_m(kr_1)$, $\cos(-m\theta_1) = \cos(m\theta_1)$, and $\sin(-m\theta_1) = -\sin(m\theta_1)$, Eq. (3.10) is rewritten as

$$H_n^{(2)}(kr_2)\, \mathcal{S}(n\theta_2) = \sum_{m=0}^{\infty} J_m(kr_1)\, \mathcal{S}(m\theta_1) \left[H_{n+m}^{(2)}(2kh) \pm (-1)^m H_{n-m}^{(2)}(2kh) \right] \frac{\epsilon_m}{2},$$
(3.11)

where

$$\epsilon_m = \begin{cases} 1, & \text{for } m = 0 \\ 2, & \text{for } m \geq 1. \end{cases}$$

Let $R_{mn}^{\pm}(2kh) = \dfrac{\epsilon_m}{2}\left[H_{n+m}^{(2)}(2kh) \pm (-1)^m H_{n-m}^{(2)}(2kh) \right]$, in which plus sign $R_{mn}^{+}(2kh)$ is chosen when $\mathcal{S}(\cdot)$ denotes $\cos(\cdot)$ function, whereas minus sign $R_{mn}^{-}(2kh)$ is chosen when $\mathcal{S}(\cdot)$ denotes $\sin(\cdot)$ function. Eq. (3.11) is written as

$$H_n^{(2)}(kr_2)\, \mathcal{S}(n\theta_2) = \sum_{m=0}^{\infty} J_m(kr_1)\, \mathcal{S}(m\theta_1)\, R_{mn}^{\pm}(2kh).$$
(3.12)

Replacing index m with n in Eq. (3.7) and using relation in Eq. (3.12), we have

$$\begin{aligned}
w_2(r_2, \theta_2) &= \sum_{n=0}^{\infty} H_n^{(2)}(kr_2) \left[A_n \cos(n\theta_2) + B_n \sin(n\theta_2) \right] \\
&= \sum_{n=0}^{\infty} \left[A_n H_n^{(2)}(kr_2) \cos(n\theta_2) + B_n H_n^{(2)}(kr_2) \sin(n\theta_2) \right] \\
&= \sum_{n=0}^{\infty} \left[A_n \sum_{m=0}^{\infty} J_m(kr_1) \cos(m\theta_1)\, R_{mn}^{+}(2kh) + \right. \\
&\qquad \left. B_n \sum_{m=0}^{\infty} J_m(kr_1) \sin(m\theta_1)\, R_{mn}^{-}(2kh) \right] \\
&= \sum_{m=0}^{\infty} J_m(kr_1) \left[A_m^{*} \cos(m\theta_1) + B_m^{*} \sin(m\theta_1) \right] = w_2(r_1, \theta_1),
\end{aligned}$$
(3.13)

where

$$A_m^{*} = \sum_{n=0}^{\infty} R_{mn}^{+}(2kh) A_n,$$
(3.14)

$$B_m^{*} = \sum_{n=0}^{\infty} R_{mn}^{-}(2kh) B_n.$$
(3.15)

The total displacement (valid only in the half-space region that $r_1 < 2h$) is now written as

$$\begin{aligned}
w(r_1, \theta_1) &= w_1(r_1, \theta_1) + w_2(r_1, \theta_1) \\
&= \sum_{m=0}^{\infty} \left\{ \left[H_m^{(2)}(kr_1) A_m + J_m(kr_1) A_m^{*} \right] \cos(m\theta_1) + \right. \\
&\qquad \left. \left[H_m^{(2)}(kr_1) B_m + J_m(kr_1) B_m^{*} \right] \sin(m\theta_1) \right\}.
\end{aligned}$$
(3.16)

A unitary displacement $w = 1$ was imposed at the cylinder circumference Γ_b, where Eq. (3.16) holds because $r_1 = a < 2h$. When w is a constant, all the coefficients for sine and cosine functions in the right hand side of Eq. (3.16) are zeros, except at $m = 0$. Therefore, we have the following set of equations

$$H_0^{(2)}(ka) A_0 + J_0(ka) A_0^* = 1 \quad \text{for } m = 0, \tag{3.17}$$

$$H_m^{(2)}(ka) A_m + J_m(ka) A_m^* = 0 \quad \text{for } m \geq 1, \tag{3.18}$$

$$H_m^{(2)}(ka) B_m + J_m(ka) B_m^* = 0 \quad \text{for } m \geq 1. \tag{3.19}$$

If we now truncate $m \in \mathbb{N}$, for instance $m = N$, we have $4 \times (N + 1)$ unknown coefficients A_m, B_m, A_m^*, and B_m^*. Meanwhile, we have $2 \times (N+1)$ equations coming from traction-free condition at the free surface as in Eqs. (3.14) and (3.15). Other $2 \times (N + 1)$ equations come from the Dirichlet boundary condition at the cylinder circumference as in Eqs. (3.17), (3.18), and (3.19). Solving this system of equations, we get the complex coefficients A_m and B_m to uniquely prescribe the displacement field of the soil domain via Eq. (3.8). In this problem, the geometry and the vibrating source are symmetric with respect to the x-axis, therefore the displacement function w is an even function of θ. This reasoning leads to $B_m = B_m^* = 0$. Obviously, solving the system of equations in Eqs. (3.15) and (3.19) gives identical results. Due to the symmetry, there are $2 \times (N + 1)$ unknown coefficients A_m and A_m^* remaining.

The soil impedance per unit length at the circumference of the cylinder is

$$
\begin{aligned}
K_z(\omega) &= -\int_0^{2\pi} \sigma_{r_1 z}\big|_{r_1=a}\, a \, \mathrm{d}\theta \\
&= -\int_0^{2\pi} \mu \frac{\partial w}{\partial r_1}\bigg|_{r_1=a}\, a \, \mathrm{d}\theta \\
&= -a\mu \sum_{m=0}^{\infty} \left\{ \left[\frac{\partial H_m^{(2)}(kr_1)}{\partial r_1}\bigg|_{r_1=a} A_m + \frac{\partial J_m(kr_1)}{\partial r_1}\bigg|_{r_1=a} A_m^* \right] \int_0^{2\pi} \cos(m\theta_1)\, \mathrm{d}\theta_1 \right\} \\
&= -2\pi a\mu \left[\frac{\partial H_0^{(2)}(kr_1)}{\partial r_1}\bigg|_{r_1=a} A_0 + \frac{\partial J_0(kr_1)}{\partial r_1}\bigg|_{r_1=a} A_0^* \right] \\
&= 2\pi a\mu k \left[H_1^{(2)}(ka) A_0 + J_1(ka) A_0^* \right]. \tag{3.20}
\end{aligned}
$$

3.3.4 Truncation errors

The analytical solution is based on the infinite series expansion, which is approximated by truncating the series at a chosen order N. The value of N is determined by the series terms that do not contribute considerably to the computed displacements and stresses at the cylinder circumference. Generally, the higher the complexity of the displacements is, the more mode shapes are required, and thus the larger the value of N becomes.

We tested the rate of convergence of the solutions by solving the problem with different values of N. For instance, SIFs of burial depth $h/a = 2.36$ were obtained with $N = \{3, 4, .., 10\}$. The shear modulus, Poisson's ratio, and density of soil domain are $\mu = 4.5$ MPa, $\nu = 0.25$, and $\rho = 1800$ kg/m^3, respectively. The outside radius of the cylinder is $a = 1.28$ m. The normalized SIFs are expressed as a function of dimensionless frequency $a_0 = a\omega/c_\beta$. As shown in Fig. 3.6, for low frequency, accurate results are obtained, even with $N = 3$. For higher frequency, larger N is required to achieve satisfactory results. The SIFs with $N = 5, 8, 10$ cannot be visually distinguished, which proves the convergence of the truncating solution.
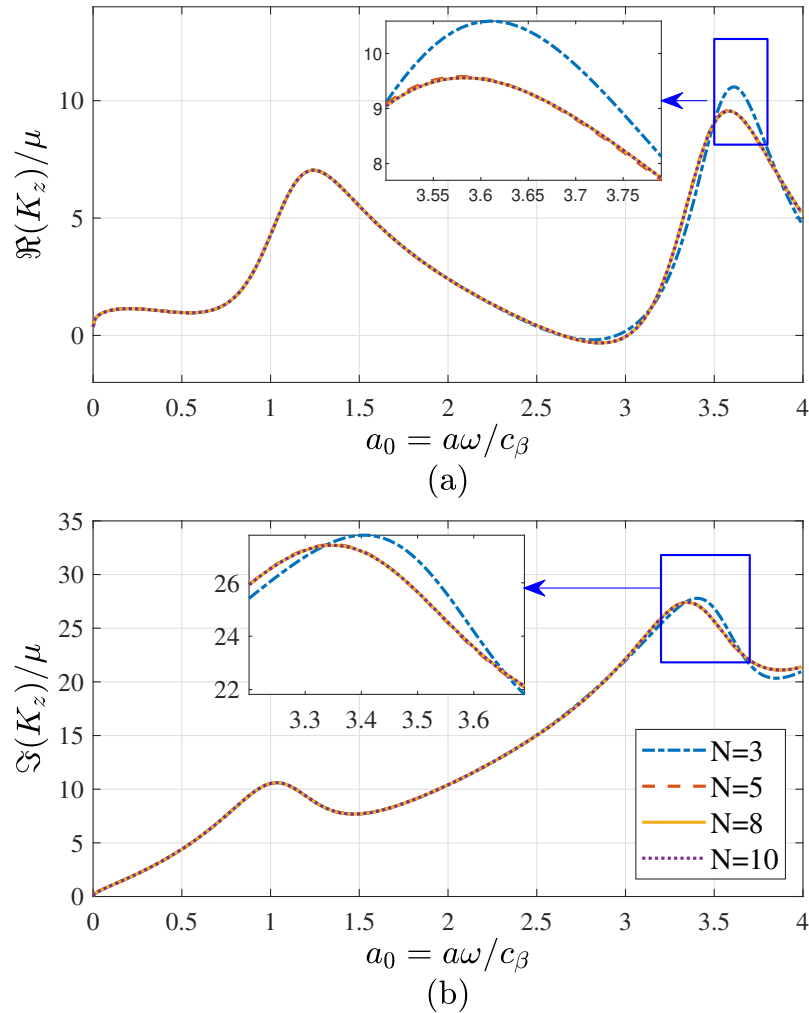
Figure 3.6: Convergence of series truncation: (a) real part; and (b) imaginary part.

To evaluate the rate of convergence, we calculated the L^2-norm of the error. The analytical solution is evaluated at dimensionless frequency $a_0^j = j\Delta a_0$, where $\Delta a_0 = 0.01$ and $j = \{1, 2, ..., 400\}$. From the previous observation, $N = 10$ can be chosen as the exact

solution. K_z^N denotes the SIF, either real or imaginary part, obtained by truncating the series at chosen order N. For each N, the L^2-norm of the error, denoted as $|E|_{L^2}$, is determined as

$$|E|_{L^2} = \frac{1}{\mu}\sqrt{\sum_{j=1}^{400}\left[K_z^N(a_0^j) - K_z^{10}(a_0^j)\right]^2 \Delta a_0}.\qquad(3.21)$$

Fig. 3.7 shows the errors for different values of N. The least-squares regression line shows that the error decays rapidly with increasing N, and the error is approximately $O(10^{-N+3})$.
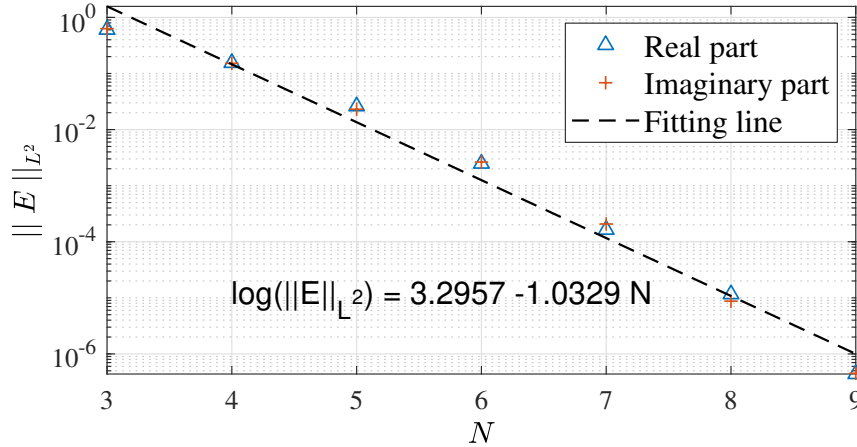
Figure 3.7: Rate of convergence.

Clearly, the truncation yielded highly accurate results for $N = 10$. Therefore, the solution with $N = 10$ was used as the reference/analytical solution from now on.

3.4 Finite element analysis for soil impedance functions of homogeneous and two-layered half-spaces

3.4.1 Numerical computation of impedance function

Seylabi et al. (2016) developed a method to extract the impedance functions of a semi-infinite half-space from a FE model. The approach is general enough that can be applied equally well to flexible interfaces as well as 3D problems. This study considers a rigid interface and an anti-plane-strain problem as in Fig. 3.8.

Recall in Eq. (3.1), the axial SIF is defined in frequency domain. Normally, the frequency domain FE solver is used to obtain the ratio of reactions to prescribed displacements, which directly yields SIF for a specific frequency. This procedure must be repeated for different frequencies to get the impedance spectra, in which the number of simulations depends on the desired resolution of the spectra. In contrast, *Seylabi et al.* (2016) showed that only one
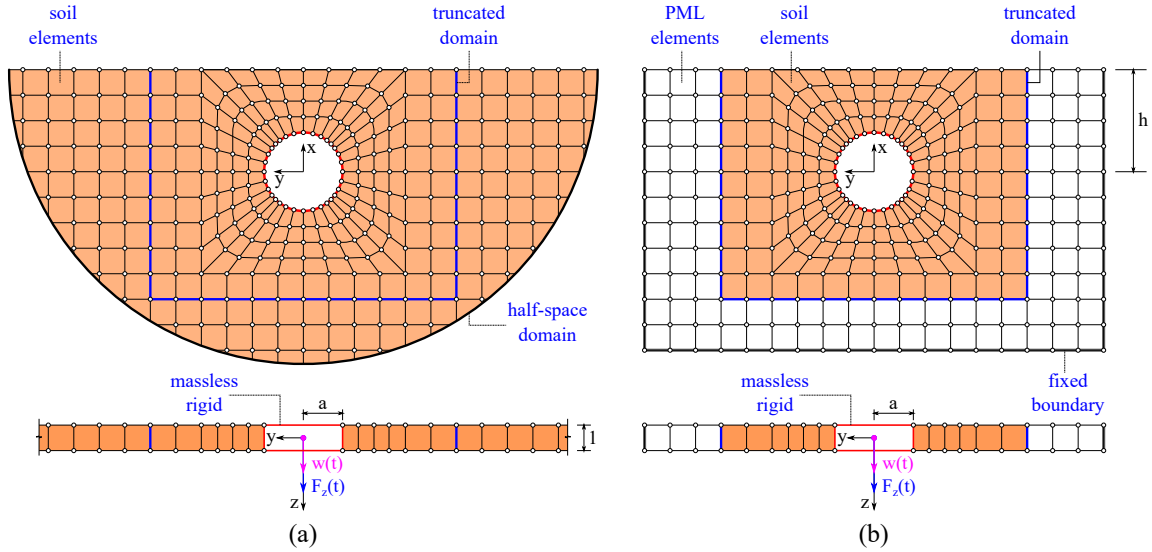
Figure 3.8: Numerical model for the estimation of SIF: (a) infinite half-space FE model; and (b) truncated half-space FE model using perfectly matched layer (PML) elements.

simulation is required to find SIF in time domain FE analysis. Therefore, we choose the latter approach to perform the SIF calculation. The motion of a rigid cylinder in an anti-plane-strain setting is shown in Figure 3.8. The SIF can be computed using the following procedure:

1. Apply the force time history $F_z(t)$ to the centroid of rigid interface. Except translational motion along the z-axis, all other degrees of freedom are constrained.

2. Record the resulting axial displacement time history $w(t)$.

3. Use Fourier transform to compute $\hat{F}_z(\omega)$.

4. Use Fourier transform to compute $\hat{w}(\omega)$.

5. Compute impedance function $K_z(\omega) = \hat{F}_z(\omega)/\hat{w}(\omega)$.

It should be noted that this is a single-degree-of-freedom problem, therefore there is not much difference between stiffness method (applying unit displacement) and flexibility method (applying unit force) because only a simple division is required instead of taking the inverse of the compliance matrix to get the stiffness matrix. Besides, it may be necessary to apply zero-padding to time signals of the applied force and resulting displacement before performing Fourier transform to increase the resolution of the calculated impedance.

3.4.2 Finite element models

3.4.2.1 Input time signal

To achieve SIF over a wide range of frequency, the energy of the input time history force should be distributed over the corresponding frequency band. A Ricker wavelet was chosen to fulfil this requirement, with the applied force in time $F(t)$ is calculated as

$$F(t) = F_0 \left[2\pi^2 f_c^2 (t - t_0)^2 - 1 \right] e^{-\pi^2 f_c^2 (t-t_0)^2} . \tag{3.22}$$

In Eq (3.22) F_0 is the amplitude of the applied force, f_c is the central frequency of the signal, and t_0 is the time when the maximum amplitude occurs. This study used $F_0 = 1$ kN, $f_c = 15$ Hz, and $t_0 = 0.2$ sec. The generated Ricker wavelet using these values is shown in Fig. 3.9. As one may see, the signal energy is distributed over a broad band from 0 to 40 Hz, which will finally yield the SIF over this frequency band.
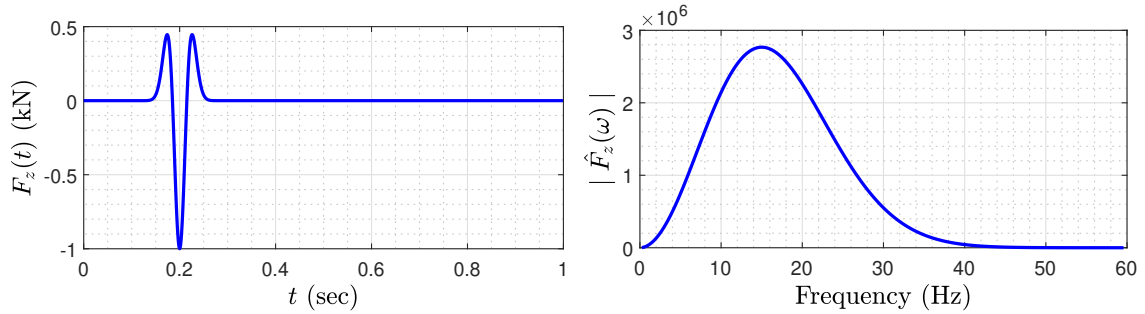
Figure 3.9: The applied force in time and frequency domain.

3.4.2.2 Spatial-temporal discretization

The FE method was used to discretize the infinite half-space model. The anti-plane-strain soil domain is truncated using absorbing boundaries conditions, provided to limit the occurrence of spurious waves that are reflected from the far-field boundaries. To avoid the fictitious energy bouncing back to the interested domain, we used PML elements (*Basu*, 2009) as shown in Fig. 3.8. The FE analyses were conducted using 3D LS-DYNA R10.0.0.

Element dimensions are chosen based on the highest frequency (f_{max}) and shear wave velocity of soil medium (c_β). Large mesh plays a role of low-pass filter and removes short-wavelength (high-frequency) energy, whereas excessively small mesh can generate numerical instability and require much more computational effort. The approximate dimension of element d_e is calculated as $d_e = \lambda_{min}/n_{epw}$, where $\lambda_{min} = c_\beta/f_{max}$ is the minimum wavelength , n_{epw} is the number of elements per wavelength. In wave propagation problem, n_{epw} is typically chosen from 6 to 10. To ensure high accuracy and computational

efficiency, we used unstructured quadrilateral grid mesh with $n_{epw} = 40$ near the cylinder circumference and $n_{epw} = 15$ near the boundary of truncated domain.

We used the explicit central difference time integration method, which is conditionally stable. Therefore, the time increment must be chosen carefully to maintain the numerical stability and accuracy. The critical time step Δt_c is based on the Courant–Friedrichs–Lewy[1] condition and calculated as $\Delta t_c = d_e/c_\alpha$, where c_α is the compression wave velocity. In this work we used a time step size of $\Delta t = 0.9\Delta t_c$. Besides, the time step is related to the sampling rate at which the resulting displacement is calculated. This sampling rate must be sufficiently high to adequately reconstruct the highest frequency in the signal. According to Nyquist–Shannon sampling theorem[2] we enforced $\Delta t < 0.5/f_{max}$.

Furthermore, termination time should be chosen to consider the SH waves bouncing back and forth between the free surface and the cylinder. The termination time must be long enough so that the cylinder displacement signal completely returns to zero. In other words, the bouncing waves must vanish, meaning that the amplitude (energy) of the bouncing waves is small enough that it can be negligible. If the termination time is short, the signal (at later time) of the bouncing waves cannot be recorded, some energy of the frequency spectrum is thus removed. That will, in turn, lead to disparities in the frequency content of the displacement signal. Fig. 3.10(a) shows an example of a 3.0-second resulting displacement in time domain for $h/a = 16$ with the effect of bouncing waves from the free surface. Whereas, Fig. 3.10(b) illustrates the frequency domain of the displacement signals, which are truncated at 1.0, 1.5, and 2.0 sec from the original displacement signal. Obviously, when the termination time is 1.0 sec, some of the displacement time histories and thus the energies are missing, causing discrepancy in frequency domain between the 1.0-second truncated signal and the 3.0-second signal. When the displacement is calculated up to 1.5 sec, the first bouncing wave is fully accounted for, and the frequency spectrum closely approaches that of the 3.0-second signal. If the termination time is 2.0 sec, the second bouncing wave also is included, the frequency domains of 2.0-second and 3.0-second signals are identical. Apparently, the displacement signal should consist of at least two bouncing waves to achieve adequate results. Moreover, the excitation force needs to be loaded and totally unloaded within termination time, which can be roughly taken as 1.0 sec. To that end, we chose termination time as $5h/c_\beta$ or 1.0 sec, whichever is larger.

For homogeneous half-space soil domain, the shear modulus, Poisson's ratio, and density

---

[1]The Courant–Friedrichs–Lewy (CFL) condition is a necessary condition for convergence of hyperbolic PDEs, which arises from studying the numerical domain of dependence.

[2]The Nyquist–Shannon sampling theorem provides a sufficient condition for the sample rate that allows a discrete sequence of samples to capture all the information from a continuous-time signal of finite bandwidth
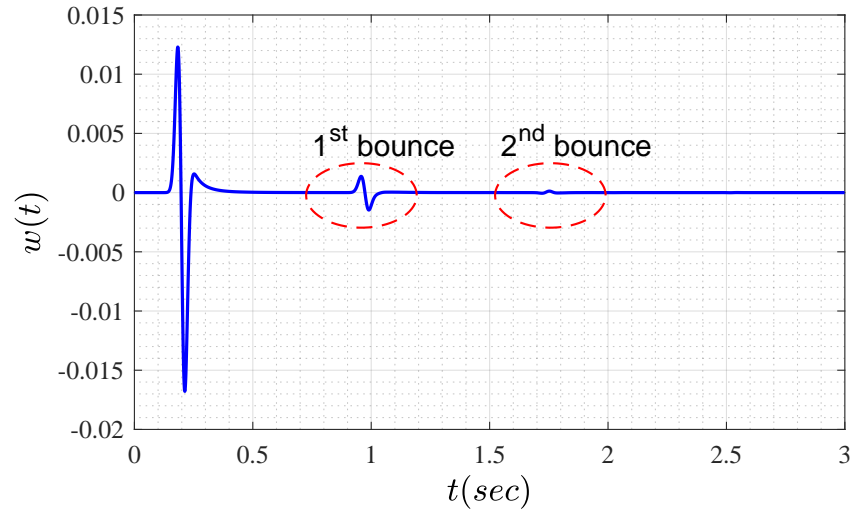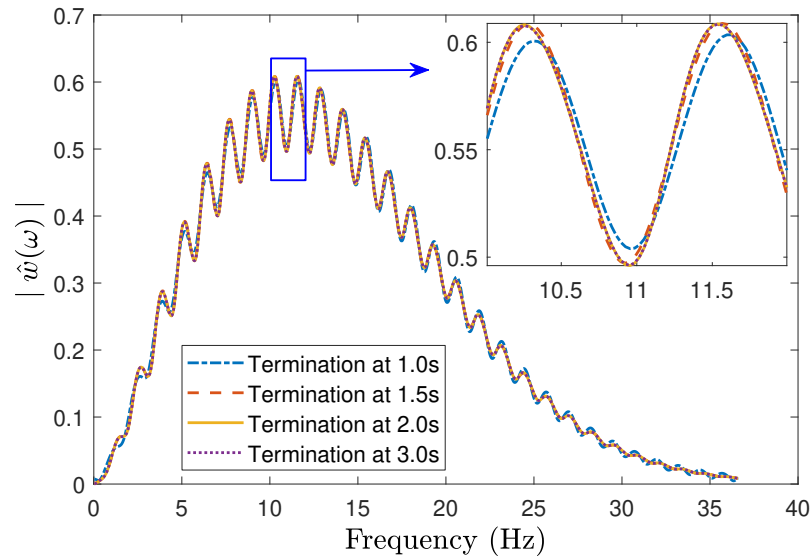
Figure 3.10: Displacement signal for $h/a = 16$ in: (a) time domain; and (b) frequency domain.

are $\mu = 4.5$ MPa, $\nu = 0.25$, and $\rho = 1800$ kg/m^3, respectively. The outside radius of the cylinder is $a = 1.28$ m.

3.5 Verification

The analytical solution derived in Subsection 3.3.3 as well as the FE analysis discussed in Subsection 3.4.1 for the axial SIFs in homogeneous half-space were compared with the impedance formula proposed by *Matsubara and Hoshiya* (2000). The cases $h/a = 2.36$

and $h/a = 5$ were chosen for verification purpose.
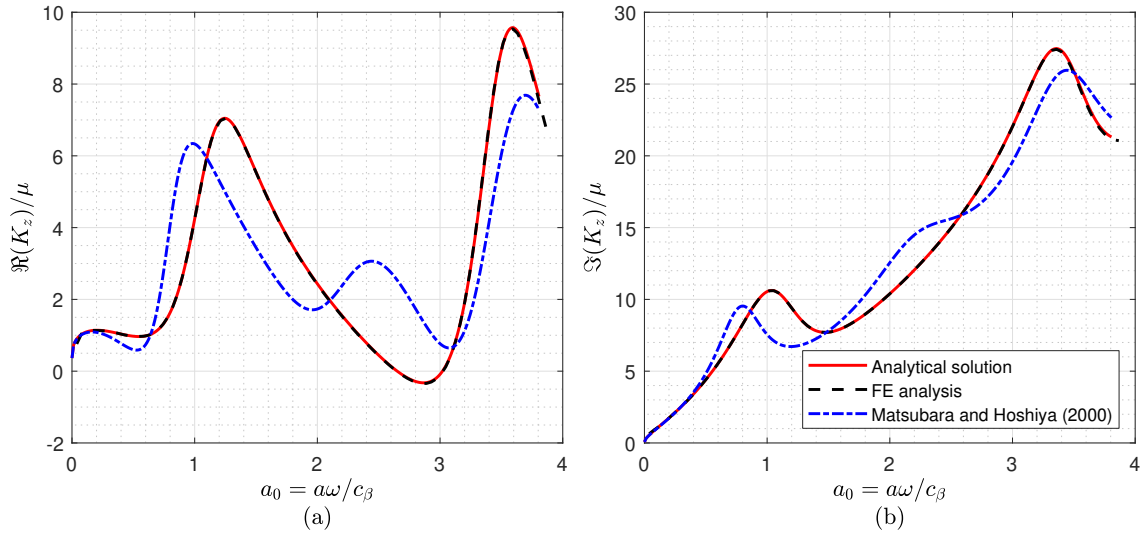
Figure 3.11: SIFs for $h/a = 2.36$: (a) real part; and (b) imaginary part.
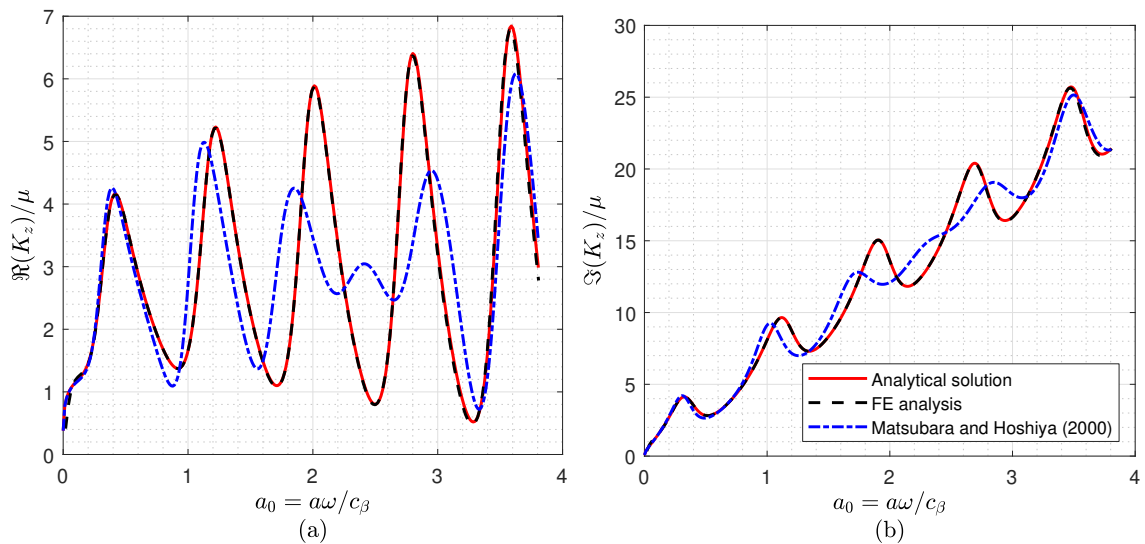
Figure 3.12: SIFs for $h/a = 5$: (a) real part; and (b) imaginary part.

Figs. 3.11 and 3.12 show that the results from analytical solution and FE analysis agree very well, whereas the results from *Matsubara and Hoshiya* (2000) are different. This discrepancy is understandable because *Matsubara and Hoshiya* solved the problem with Neumann boundary condition by applying shear stress at the soil-cylinder interface, rather than Dirichlet boundary condition as it was done in this work. Despite the mathematical correctness, their solution is an approximation in the sense that the resulting displacement was achieved by averaging the displacement of all the nodes along the circular interface

and the stiffness (rigidity) of the cylinder cannot be taken into account. Because of the averaging nature, their solution can yield reasonable SIF in case of low-frequency loading, but inaccurate SIF in high-frequency excitation. In the low-frequency excitation zones, the displacements of interface nodes are not much different, which roughly represents the rigid body motion. Hence, the results of *Matsubara and Hoshiya* coincide with the proposed analytical solutions and FE analyses, as shown in Figs. 3.11 and 3.12. But, when it comes to higher frequency excitation, the displacements of those nodes evolve differently, causing the deviation of *Matsubara and Hoshiya* solutions from the other two solutions.

3.6 Homogeneous half-space

We used the analytical solution obtained in Subsection 3.3.3 to generate SIFs for different cases of burial depth. This approach was chosen because it requires less computational effort.

Fig. 3.13 illustrates the real and imaginary parts of SIFs for $h/a = \{4, 8, 12, 16, \infty\}$. The SIF for full-space problem by *Novak et al.* (1978) also is plotted for comparison. Overall, the half-space SIFs for different burial depths oscillate about an average curve, which in this case is the SIF for the full-space. These oscillations are attributed to the reflected SH waves from the half-space free surface, which propagate through the burial depth h and strike the cylinder. The constructive or destructive interference of waves occurring within the region between the soil free surface and the cylinder leads to the amplification or reduction of the reaction at the cylinder boundary.

As a result, the characteristic of this oscillation significantly depends on h. The amplitude of the oscillation for the case $h/a = 4$ yields the largest value when it is compared against the burial depth $h/a = \{8, 12, 16\}$. When the location of the cylinder is deeper, this amplitude gradually decreases, indicating that the influence of reflected waves on the stresses at the cylinder circumference decreases. This fact makes sense, because the reflected SH waves radiate energy along their propagation paths. The further they travel, the more energy lost. Consequently, those waves with low levels of remaining energy are not strong enough to considerably interfere with the pre-existing displacements and stresses at the cylinder boundary. In terms of frequency, the SIFs oscillation closely resembles the ideally simplified problem of the interference of two point sources with equal amplitude and same phases, in which the net disturbance at a point P is proportional to $\cos{(\Delta\phi/2)}$, where $\Delta\phi$ is the phase difference between the signals arriving at P from two sources (*Towne*, 1988). If the distance between two sources is $2h$ and P coincides with one source, $\Delta\phi = 2kh$, and thus the disturbance is proportional to $\cos{(kh)}$, a sinusoidal function of wavenumber k
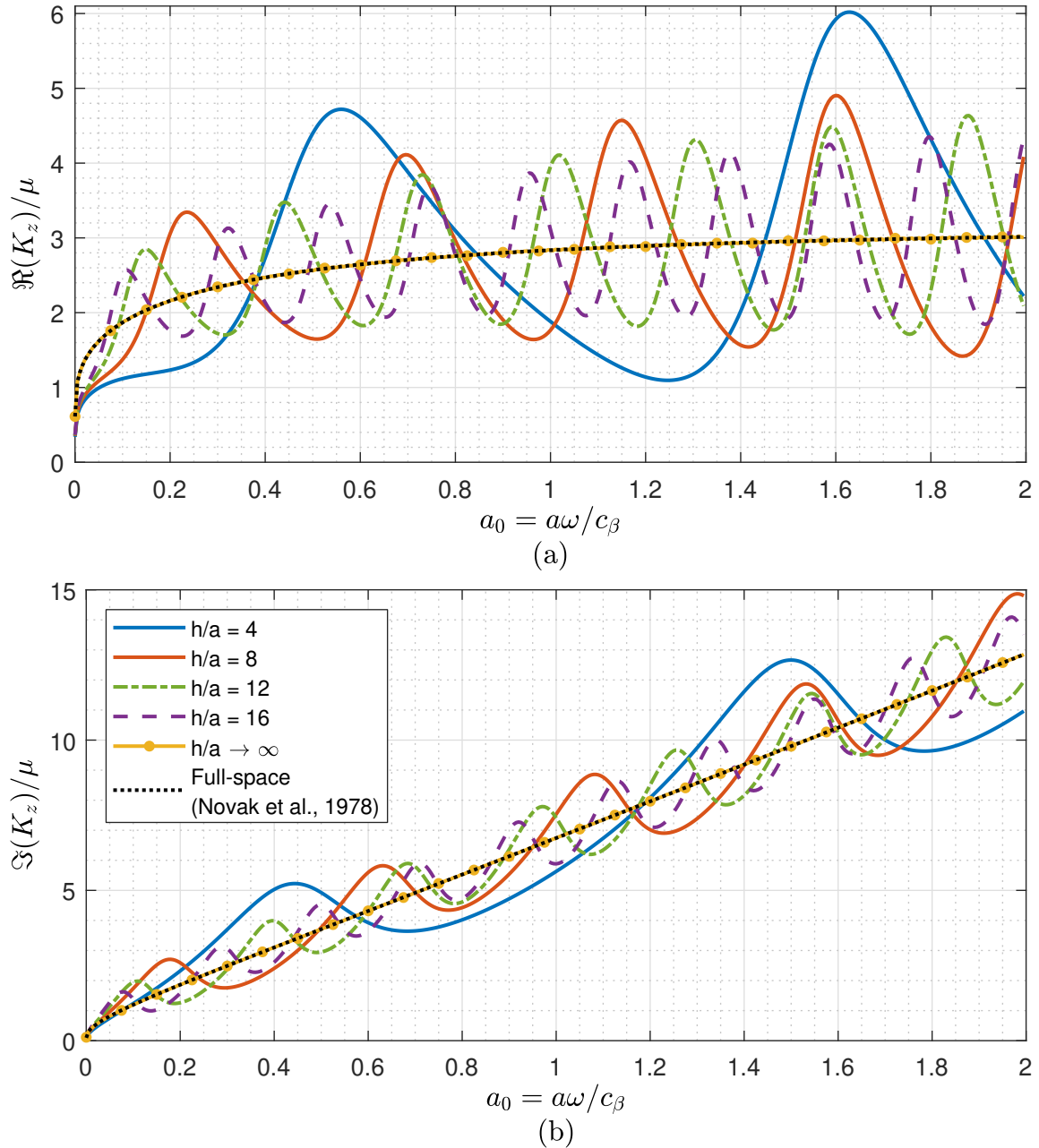
Figure 3.13: SIFs for different cases of burial depth: (a) real part; and (b) imaginary part.

with frequency h. Although the actual and imaginary cylinders have finite lengths and the wave amplitude of the imaginary cylinder is attenuated when reaching the actual cylinder boundary, the SIFs of half-space look roughly like oscillating sinusoidal functions with frequency proportional to h. The smallest burial depth $h/a = 4$ generates oscillation of SIFs with lowest frequency, whereas the larger burial depths produce oscillations with higher frequencies (Fig. 3.13). Observably, the preceding variation patterns of oscillatory amplitude and frequency occur in both real and imaginary parts of the SIFs.

Clearly, the differences between SIFs of half-space domain and that of full-space domain are considerable. Even with $h/a = 16$, the percentage difference is up to 50% in the high dimensionless frequency region. As a result, these differences must be accounted for in the design process of underground buried structures.

When h/a is very large $h/a \rightarrow \infty$, e.g., $h/a = 10^5$, the reflected waves lose almost all of their energy and virtually disappear before impinging on the cylinder. The half-space SIF should, therefore, converge to its full-space counterpart. As shown in Fig. 3.13, the SIFs for half-space when $h/a \rightarrow \infty$ perfectly match the full-space SIFs.

3.7 Two-layered half-space

In this section, we used the FE analysis approach to generate SIFs for two-layered soil stratum. The geometry of the problem is displayed in Fig. 3.14, in which h_1 and h_2 are the distances from the center of the cylinder to the surface of the soil layer 1 and layer 2, respectively. Both soil layers have same values of mass density $\rho = 1800$ kg/m^3 and Poisson's ratio $\nu = 0.25$, but different values of shear modulus, μ_1 compared with μ_2. For the soil layer 1, the shear modulus is $\mu_1 = 4.5$ MPa. The outside radius of the cylinder is $a = 1.28$ m. The effects of material contrast ratio μ_1/μ_2 and structure location h_1/a and h_2/a on the axial SIF are investigated.
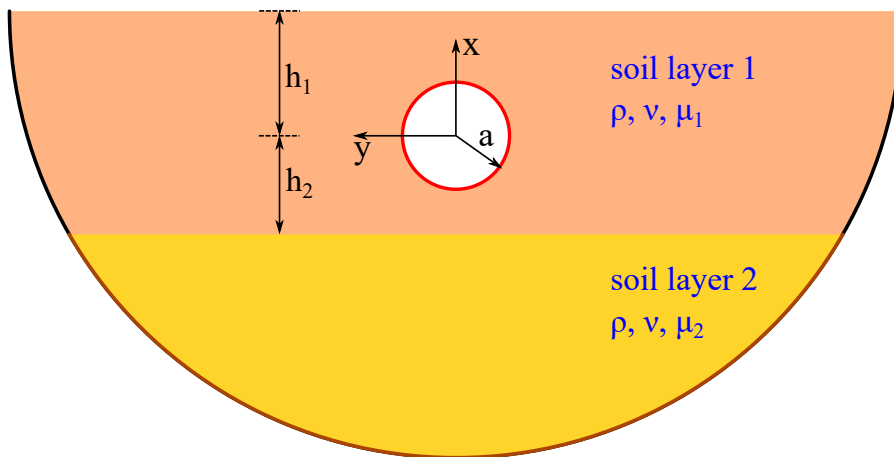
Figure 3.14: Geometry of two-layered half-space.

3.7.1 Effect of material contrast

Two configurations $h_1/a = 2h_2/a = 4$ and $h_1/a = h_2/a = 4$ are considered to investigate the effect of material contrast. Figs. 3.15 and 3.16 show the normalized real and imaginary parts of SIFs for a material contrast $\mu_1/\mu_2 = \{0.10, 0.25, 0.50, 0.75, 1.00\}$ as a function

of dimensionless frequency $a_0 = a\omega/c_{\beta 1}$, where $c_{\beta 1} = \sqrt{\mu_1/\rho}$ is the shear wave velocity of soil layer 1. In these figures, the analytical results for homogeneous half-space (i.e., $\mu_1/\mu_2 = 1.00$) also were displayed in black dashed-line. In general, the material contrast affects the SIFs in a similar manner in two cases of burial depth, where the SIFs of two-layered soil domains show some deviations from that of the homogeneous half-space because of the reflection from the interface between soil layers. The smallest material contrast ratio $\mu_1/\mu_2 = 0.10$ produces the largest deviation. When this ratio becomes larger, the impedance curve becomes closer to that of the homogeneous half-space. This is not particularly surprising because a smaller contrast ratio implies a higher percentage of energy entrapment in layer 1, and lower energy leakage into layer 2. The reflected waves from the soil layer interface, consequently, strike the cylinder harder and generate more variations in SIFs. When μ_1/μ_2 becomes larger and approaches 1, the energy entrapment becomes smaller and totally escapes from the top soil layer, the SIF of two-layered domain finally coincides with that of homogeneous half-space.
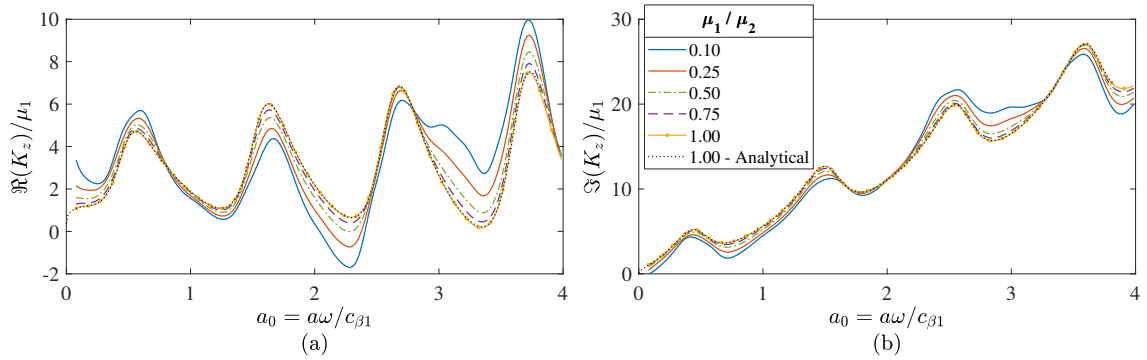
Figure 3.15: SIFs for $h_1/a = 4$ and $h_2/a = 2$ depending on material contrast ratio: (a) real part; and (b) imaginary part.
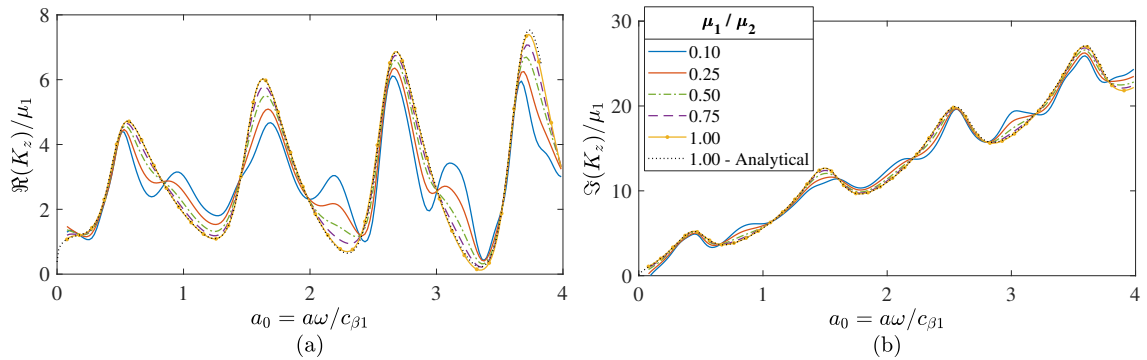
Figure 3.16: SIFs for $h_1/a = 4$ and $h_2/a = 4$ depending on material contrast ratio: (a) real part; and (b) imaginary part.

		$\frac{\mu_1}{\mu_2} = 0.10$	$\frac{\mu_1}{\mu_2} = 0.25$	$\frac{\mu_1}{\mu_2} = 0.50$	$\frac{\mu_1}{\mu_2} = 0.75$	$\frac{\mu_1}{\mu_2} = 1.00$
$h_1/a = 4$	$h_2/a = 2$	5.67	3.47	1.73	0.71	0
	$h_2/a = 4$	3.64	2.29	1.17	0.49	0
	$h_2/a = 8$	2.70	1.71	0.88	0.37	0
	$h_2/a = 16$	2.03	1.29	0.66	0.28	0
$h_1/a = 8$	$h_2/a = 2$	5.67	3.52	1.76	0.73	0
	$h_2/a = 4$	3.73	2.34	1.19	0.49	0
	$h_2/a = 8$	2.95	1.86	0.96	0.40	0
	$h_2/a = 16$	2.02	1.29	0.66	0.28	0

Table 3.1: Dimensionless area $\mathcal{A}$ between SIF curves of two-layered domain and that of homogeneous half-space.

Furthermore, to quantify the difference between the SIF of a two-layered domain and that of a homogeneous half-space, we calculated the dimensionless area bounded by the curves of real parts of these two SIFs. In a two-layered domain problem, the dimensionless area $\mathcal{A}$ of the SIF curve is defined as

$$\mathcal{A} = \frac{1}{\mu_1} \int_{0.05}^{4} \left| \Re\left(K_z\right) - \Re\left(K_z^{ho}\right) \right| da_0, \tag{3.23}$$

where K_z is the SIF of a two-layered domain with $\mu_1/\mu_2 = \{0.10, 0.25, 0.50, 0.75\}$ and K_z^{ho} is the SIF of homogeneous half-space with $\mu_1/\mu_2 = 1.00$. Note that the geometry h_1/a must be the same for generating K_z and K_z^{ho}. Table 3.1 presents the values of $\mathcal{A}$ for different configurations, in which large $\mathcal{A}$ means large difference in the SIF between two-layered domain and homogeneous half-space, and vice versa. The values of $\mathcal{A}$ are considerably larger when $\mu_1/\mu_2 = \{0.10, 0.25\}$. Whereas, there are only slight differences in SIFs between homogeneous half-space and two-layered domains if the material contrast ratio is less than 0.5. This observation is consistent with the energy entrapment explained previously.

3.7.2 Effect of structure location

The ratio h_1/a is physically related to the effect of the reflection from the free surface, while the ratio h_2/a is associated with the reflection from the interface between two soil layers. The effect of h_1/a on SIFs was already explained in Section 3.6, hence the effect of h_2/a on SIFs is analyzed in this section.

Table 3.1 also shows the general effect of cylinder location on the SIFs of a two-layered domain. For each material contrast ratio μ_1/μ_2 and burial depth h_1/a, the dimensionless area $\mathcal{A}$ gradually decreases with increased values of h_2/a. This implies the two-layered domain SIFs are approaching the homogeneous half-space SIFs. The SH waves reflected from the soil layer interface dissipate energy along their propagation paths, similarly to the reflected ones from the free surface. When h_2/a is larger, the impact of soil interface reflection on the cylinder is weaker and eventually becomes insignificant. Figs. 3.17 and 3.18 show the SIFs for $h_1/a = 4$ and $h_1/a = 8$, respectively. For each burial depth, five lines are plotted, four of two-layered domain with $h_2/a = \{2, 4, 8, 16\}$ and $\mu_1/\mu_2 = 0.25$ and another of homogeneous half-space $\mu_1/\mu_2 = 1.00$ where h_2 plays no role. Evidently, the distance h_2/a has a similar effect on the SIFs as the burial depth h_1/a, in which an increase in h_2 leads to an increase in frequency but a decrease in amplitude of the fluctuation of two-layered domain SIF about an average curve. For the SIF of a two-layered domain, the average curve is the SIF of the corresponding homogeneous half-space, which has the same value of h_1/a. This similarity is as expected because both effects are related to phase difference and energy loss during wave propagation. When $h_2/a = 16$, the SIFs of two-layered domains fluctuate with highest frequency but smallest amplitude around the SIF of corresponding homogeneous half-space. Accordingly, two-layered SIFs can be replaced with that of corresponding homogeneous half-space for practical design purposes when h_2/a is large enough, e.g., $h_2/a \geq 16$.
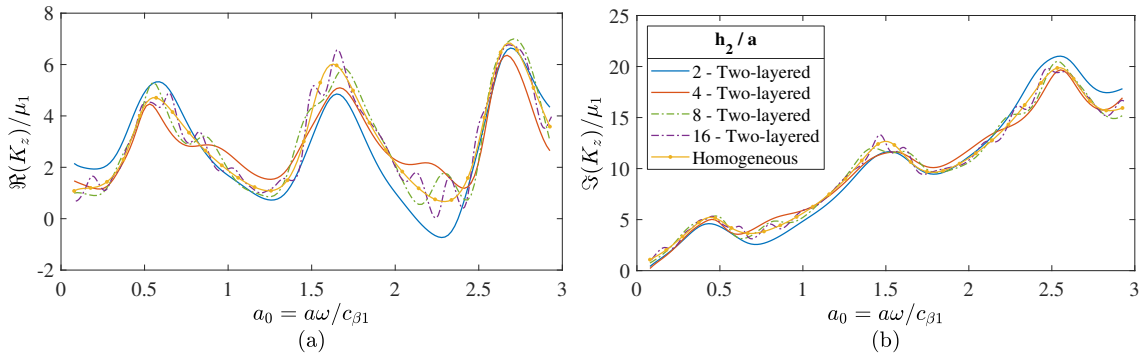
Figure 3.17: SIFs for $h_1/a = 4$ in two-layered domain ($\mu_1/\mu_2 = 0.25$) and homogeneous half-space ($\mu_1/\mu_2 = 1.00$): (a) real part; and (b) imaginary part.

3.8 Conclusions

This chapter presents an analytical solution to compute the axial SIFs of buried structures in homogeneous elastic half-space. The mixed-boundary-value problem was solved in the frequency domain using Hankel–Fourier series expansion and Graf's addition theorem. We
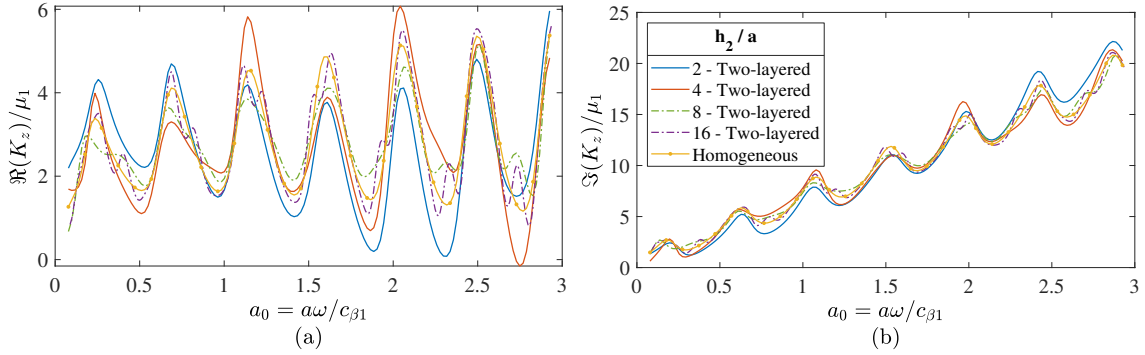
Figure 3.18: SIFs for $h_1/a = 8$ in two-layered domain ($\mu_1/\mu_2 = 0.25$) and homogeneous half-space ($\mu_1/\mu_2 = 1.00$): (a) real part; and (b) imaginary part.

also used a numerical approach based on FE analysis in time domain to generate the axial SIFs for those structures in homogeneous and layered elastic half-space. For homogeneous half-space, results of the devised analytical solution showed a complete agreement with those of the FE analysis. In summary, our study showed/confirmed that

1. In SSI problems of buried structures, the frequency dependence of SIFs is more pronounced than in the case of either shallow or deep foundations because of the wave interference occurring within the region between the soil free surface and the structures. This phenomenon must be considered in the design process of buried structures, in particular for spatially distributed ones.

2. Overall, the SIF of a buried structure depends mostly on the excitation frequency, the shear modulus of soil domain, and the burial depth and dimension of the structure. In a layered soil domain, the SIF depends also on material contrast and the distance from the structure to the interface between soil layers.

3. We showed that a number of $N = 10$ modes in the Hankel–Fourier series are enough to accurately approximate the SIF of a buried structure. Moreover, we showed that the error of the truncation of infinite series decays rapidly with increasing N, and the error is approximately $O(10^{-N+3})$.

4. The SIFs of homogeneous half-space oscillate around the SIFs of homogeneous full-space because of the reflection from the free surface. When the burial depth increases, this oscillation undergoes an increase in frequency but a decrease in amplitude. The half-space SIFs converge to full-space SIFs if the burial depth is very large.

5. Analogously, the SIFs of two-layered half-space oscillate around the SIFs of corresponding homogeneous half-space because of the reflection from the interface be-

tween soil layers. The distance from cylinder center to soil layer interface h_2 affects SIFs in a similar manner that the burial depth h_1 does.

6. The difference between SIFs of two-layered half-space and that of corresponding homogeneous half-space depends primarily on the material contrast μ_1/μ_2 and the distance from cylinder center to soil layer interface h_2. This discrepancy becomes larger when smaller value of material contrast μ_1/μ_2 (high energy entrapment) and smaller value of h_2 (less energy dissipated along wave propagation path) are considered.

7. If $\mu_1/\mu_2 \geq 0.50$ or $h_2/a \geq 16$, the SIFs of a two-layered half-space can be replaced with that of the corresponding homogeneous half-space for practical design purpose.

Despite some limitations, namely the applicability for rigid (or nearly rigid) circular structures and for elastic domains with small displacements, this study is an important step toward building a reduced-order model to investigate SbSI problems. Our work provides useful information about initial spring stiffness and dashpot damping coefficient in axial direction, which we envision integrating in large-scale SbSI models, e.g., reduced-order model to study soil-pipeline interaction presented in *Nguyen and Asimaki* (2018, 2020); *Asimaki et al.* (2019).

Dynamic in-plane soil impedance functions for rigid circular structures buried in elastic half-space

Contents of this chapter

4.1   Introduction

As mentioned in Chapter 3, it is crucial to accurately calculate the SIFs, taking into account the energy reflected from the free surface of a half-space domain. Chapter 3 presents the results for dynamic SIFs in axial direction. In order to complement the results in three-dimensional space, this chapter studies the dynamic in-plane SIFs.

In this chapter, we derive an analytical solution for the dynamic in-plane SIFs of an infinitely long rigid cylinder buried in homogeneous elastic half-space. We solved a mixed-boundary-value problem, where a harmonic displacement is prescribed at the structure boundary and traction-free condition is satisfied at the free surface. The analytical approach yields closed-form solutions with high accuracy and relatively simple numerical implementation, providing the benchmark to verify other approximate solutions. However, the applicability of this method is in general limited to simple geometries with linear elastic or viscoelastic material. In this regard, the computational approach is applicable to most practical problems with more complex geometries and material nonlinearities. We used high-fidelity numerical models to accurately extract the dynamic in-plane SIFs, which can be generalized to any geometry of underground structure or soil strata. FE analyses were used to perform the SIFs calculation for homogeneous and two-layered half-spaces. Finally, we conducted a parametric study to investigate the effects of geometric and mechanical factors, such as burial depth, Poisson's ratio, material contrast, and structure location, on the dynamic in-plane SIFs of homogeneous and two-layered half-spaces.

The remainder of this chapter is organized as follows: In Section 4.2, we reviewed some basics of the dynamic in-plane SIFs. In Section 4.3, we used Hankel– and Bessel–Fourier series expansion of the displacement potentials, together with numerical evaluation of the contour integrals to derive the analytical solution for homogeneous half-space. In Section 4.4, we also described the FE modeling procedure to generate the dynamic in-plane SIFs for homogeneous and two-layered half-spaces. In Section 4.5, we verified the results obtained by analytical and FE approaches for homogeneous half-space. Section 4.6 presents the effect of cylinder burial depth and Poisson's ratio on the SIFs of homogeneous half-space, while Section 4.7 shows the impact of material contrast and structure location on SIFs of two-layer half-space. Concluding remarks were provided in Section 4.8.

4.2   Review of in-plane soil impedance functions

To investigate the SbSI problems, an important task is to compute the SIF for the "associated" massless structure as a function of frequency. The "associated" structure is identical to the actual one in terms of geometry and material properties, but has no mass. Technically,

the SIF describes the relationship between displacements (at soil-structure interface) and interacting forces that soil domain exerts on structure. For a given steady-state harmonic excitation, the dynamic SIF is defined as the ratio between the force (or moment) and the resulting displacement (or rotation) at the centroid of rigid body (*Gazetas*, 1983).

The motion of a rigid cylinder interface in an in-plane setting is shown in Fig. 4.1. It is defined by three degrees of freedom: the horizontal, the vertical, and rotational motions denoted here by $\hat{u}_{x1}$, $\hat{u}_{y1}$, and $\hat{\theta}_1$, respectively. The force-displacement relations for $\hat{\boldsymbol{F}}(\omega) \in \mathbb{C}^3$, $\hat{\mathbb{K}}(\omega) \in \mathbb{C}^{3\times3}$, and $\hat{\boldsymbol{u}}(\omega) \in \mathbb{C}^3$, over the rigid interface, in the frequency domain can be written as

$$\hat{\boldsymbol{F}}(\omega) = \hat{\mathbb{K}}(\omega)\,\hat{\boldsymbol{u}}(\omega)\,, \tag{4.1}$$

where $\omega \in \mathbb{R}$ is the angular frequency, $\hat{\boldsymbol{F}}(\omega)$ is the applied force vector, $\hat{\mathbb{K}}(\omega)$ is the soil impedance matrix, and $\hat{\boldsymbol{u}}(\omega)$ is the displacement vector at the centroid of the cylinder. Equation (4.1) can be written in matrix form as

$$\begin{bmatrix} \hat{F}_{y1} \\ \hat{F}_{x1} \\ \hat{M}/a \end{bmatrix} = \begin{bmatrix} \hat{K}_{yy} & 0 & 0 \\ 0 & \hat{K}_{xx} & \hat{K}_{x\theta} \\ 0 & \hat{K}_{\theta x} & \hat{K}_{\theta\theta} \end{bmatrix} \begin{bmatrix} \hat{u}_{y1} \\ \hat{u}_{x1} \\ a\,\hat{\theta}_1 \end{bmatrix}, \tag{4.2}$$

where $\hat{F}_{x1}$ and $\hat{F}_{y1}$ are the resultant applied forces in x_1 and y_1 directions, respectively. The characteristic length a, i.e., the outside radius of the cylinder, is used for normalizing $\hat{M}$ and $\hat{\theta}_1$ which denote the moment and the rotation angle with respect to the centroid of the cylinder. Each component of the symmetric impedance matrix $\hat{\mathbb{K}}(\omega)$ is a complex-valued function, where the real part represents the mass inertia and stiffness, while the imaginary part reflects the radiational and material damping of the soil domain (*Gazetas*, 1983). The complex value of SIF physically implies that there is time delay between the applied force and the resulting displacement. Because all the SIFs in this work are in frequency domain only, the hat superscript "^" of SIFs is henceforth omitted for simplicity, for instance, $\hat{K}_{yy}$ is rewritten as K_{yy}.

4.3 Analytical solution for soil impedance functions of homogeneous half-space

4.3.1 Assumptions

We used the following assumptions to devise the analytical solution for the SIFs:
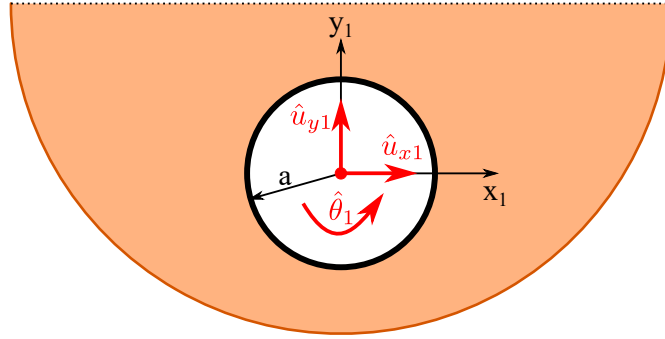
Figure 4.1: Rigid cylinder kinematics for the definition of SIFs.

- The soil domain is half-space, homogeneous, isotropic, and linear elastic.

- The buried structure (cylinder) is rigid, circular, massless, and infinitely long.

- The cylinder-soil interface is fully bonded.

- The displacements and strains are small.

4.3.2 Governing equation
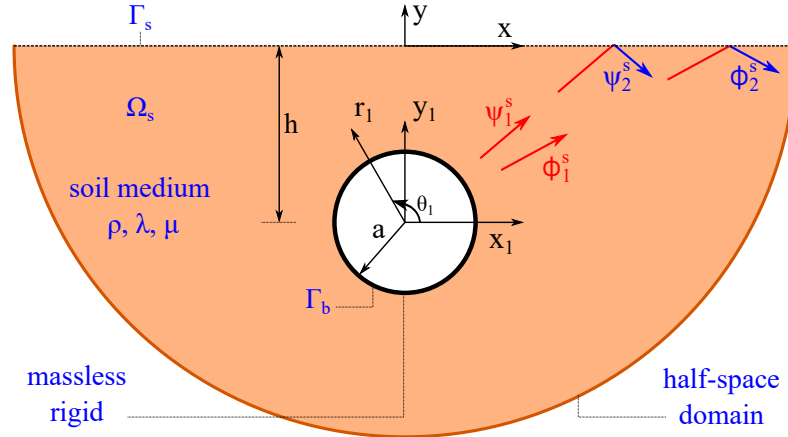
Figure 4.2: The problem configuration.

The governing equation for a general linear elastodynamics problem (*Kausel*, 2006; *Graff*, 2012), in the absence of body forces, is

$$\mu \nabla^2 \boldsymbol{u} + (\lambda + \mu) \nabla (\nabla \cdot \boldsymbol{u}) = \rho \ddot{\boldsymbol{u}} \quad \text{in } \Omega_s, \tag{4.3}$$

where $\Omega_s \subseteq \mathbb{R}^3$ is the soil half-space domain, λ and μ are the Lamé constants, $\boldsymbol{u} : \Omega_s \to \mathbb{R}^3$ is the displacement vector field, and ρ is the mass density of soil medium.

Using Helmholtz decomposition (*Helmholtz*, 1858), the displacement vector field is written as $\boldsymbol{u} = \nabla\phi + \nabla \times \boldsymbol{\psi}$, where ϕ is a scalar potential, $\boldsymbol{\psi}$ is a vector potential satisfying $\nabla \cdot \boldsymbol{\psi} = 0$. Eq. (4.3) turns into two uncoupled equations $c_\alpha^2 \nabla^2 \phi = \ddot{\phi}$ and $c_\beta^2 \nabla^2 \boldsymbol{\psi} = \ddot{\boldsymbol{\psi}}$ (*Graff*, 2012), where $c_\alpha = \sqrt{(\lambda + 2\mu)/\rho}$ and $c_\beta = \sqrt{\mu/\rho}$ are the compression and shear wave velocities, respectively. For plane-strain cases, only out-of-plane component ψ of vector $\boldsymbol{\psi}$ is non-zero, hence the equation of vector potential $\boldsymbol{\psi}$ reduces to $c_\beta^2 \nabla^2 \psi = \ddot{\psi}$.

Fig. 4.2 shows the geometry of the problem with the cylindrical coordinate (r_1, θ_1, z) and Cartesian coordinate (x_1, y_1, z), (x, y, z) systems. The governing equation and traction-free boundary condition can be expressed as

$$\frac{\partial^2 \phi}{\partial r_1^2} + \frac{1}{r_1}\frac{\partial \phi}{\partial r_1} + \frac{1}{r_1^2}\frac{\partial^2 \phi}{\partial \theta_1^2} = \frac{1}{c_\alpha^2}\frac{\partial^2 \phi}{\partial t^2} \qquad \text{in } \Omega_s , \tag{4.4}$$

$$\frac{\partial^2 \psi}{\partial r_1^2} + \frac{1}{r_1}\frac{\partial \psi}{\partial r_1} + \frac{1}{r_1^2}\frac{\partial^2 \psi}{\partial \theta_1^2} = \frac{1}{c_\beta^2}\frac{\partial^2 \psi}{\partial t^2} \qquad \text{in } \Omega_s , \tag{4.5}$$

$$\sigma_{yx} = \sigma_{yy} = 0 \qquad \text{on } \Gamma_s , \tag{4.6}$$

where Γ_s is the free surface of soil medium. On Γ_s, $y_1 = h$, where h is the burial depth of the cylinder.

To find the in-plane SIFs, a harmonic unitary displacement is imposed on Γ_b, which is the circumference of the rigid cylinder. On Γ_b, $r_1 = a$, where a is the outer radius of the cylinder. To find the values of K_{yy}, K_{xx}, and $K_{\theta x}$, the Dirichlet boundary conditions are

$$u_{x1} = u_{y1} = e^{-i\omega t} \qquad \text{on } \Gamma_b , \tag{4.7}$$

$$\hat{\theta}_1 = 0 \qquad \text{on } \Gamma_b . \tag{4.8}$$

To find the values of $K_{x\theta}$ and $K_{\theta\theta}$, the Dirichlet boundary conditions are

$$u_{x1} = u_{y1} = 0 \qquad \text{on } \Gamma_b , \tag{4.9}$$

$$\hat{\theta}_1 = e^{-i\omega t} \qquad \text{on } \Gamma_b . \tag{4.10}$$

4.3.3 Displacement potentials

For simplicity, the time factor $e^{-i\omega t}$ is henceforth omitted. Using separation of variables in cylindrical coordinate, *Mow and Pao* (1971) proposed a general form of solution for the scalar displacement potential

$$\phi(r_1, \theta_1) = \sum_{n=-\infty}^{\infty} \left[C_{1n} H_n^{(1)}(k_\alpha r_1) + C_{2n} H_n^{(2)}(k_\alpha r_1) \right] e^{in\theta_1}, \tag{4.11}$$

where $k_\alpha = \omega/c_\alpha$ is the wavenumber, C_{1n} and C_{2n} are complex coefficients. Either Hankel functions $H_n^{(1)}(k_\alpha r_1)$, $H_n^{(2)}(k_\alpha r_1)$ or Bessel functions $J_n(k_\alpha r_1)$, $Y_n(k_\alpha r_1)$ are possible forms, which ones are chosen depending on the ease of algebraic calculation. The solution for ψ has similar form, except that k_α is replaced with $k_\beta = \omega/c_\beta$.

The presence of the buried cylinder results in P- and SV-waves scattering from the structure interface. These scattered waves are represented by the Hankel functions of the first kind, which satisfy the Sommerfeld's radiation condition and correspond to the outgoing wave (recall that time factor is $e^{-i\omega t}$). The potentials of the scattering P- and SV-waves are

$$\phi_1^s(r_1, \theta_1) = \sum_{n=-\infty}^{\infty} A_{1n} H_n^{(1)}(k_\alpha r_1) e^{in\theta_1}, \tag{4.12}$$

$$\psi_1^s(r_1, \theta_1) = \sum_{n=-\infty}^{\infty} B_{1n} H_n^{(1)}(k_\beta r_1) e^{in\theta_1}. \tag{4.13}$$

The P- and SV-waves propagate to the half-space free surface and then they get reflected. The reflection waves are represented by the Bessel functions of the first kind, which are finite at the origin. The potentials of the reflected P- and SV-waves are

$$\phi_2^s(r_1, \theta_1) = \sum_{n=-\infty}^{\infty} A_{2n} J_n(k_\alpha r_1) e^{in\theta_1}, \tag{4.14}$$

$$\psi_2^s(r_1, \theta_1) = \sum_{n=-\infty}^{\infty} B_{2n} J_n(k_\beta r_1) e^{in\theta_1}. \tag{4.15}$$

The total displacement potentials of P- and SV-waves in the homogeneous half-space are

$$\phi(r_1, \theta_1) = \phi_1^s(r_1, \theta_1) + \phi_2^s(r_1, \theta_1) = \sum_{n=-\infty}^{\infty} \left[A_{1n} H_n^{(1)}(k_\alpha r_1) + A_{2n} J_n(k_\alpha r_1) \right] e^{in\theta_1}, \tag{4.16}$$

$$\psi(r_1, \theta_1) = \psi_1^s(r_1, \theta_1) + \psi_2^s(r_1, \theta_1) = \sum_{n=-\infty}^{\infty} \left[B_{1n} H_n^{(1)}(k_\beta r_1) + B_{2n} J_n(k_\beta r_1) \right] e^{in\theta_1}. \tag{4.17}$$

The displacement field is uniquely described if we can determine the complex coefficients A_{1n}, B_{1n}, A_{2n}, and B_{2n}.

4.3.4 Traction-free condition at $y = 0$

Lin et al. (2010) used the inverse Fourier transform from wavenumber domain into spatial domain to represent a Hankel function:

$$H_n^{(1)}(k_0 r_1) e^{in\theta_1} = \int_{-\infty}^{\infty} \left[\left(\frac{i^{-n}}{i\pi\nu_0} \right) \left(\frac{k - \nu_0}{k_0} \right)^n \right] e^{ikx_1 - \nu_0|y_1|} dk, \tag{4.18}$$

where $v_0 = \sqrt{k^2 - k_0^2}$ and (k_0, v_0) represents either (k_α, v_α) or (k_β, v_β). To apply the zero-stress boundary condition, they transformed the representation of scattering and reflecting wave potentials in the domain $-h \le y \le 0$ (or $0 \le y_1 \le h$) from cylindrical to rectangular coordinates as follows

$$\phi_1^s(r_1, \theta_1) = \sum_{n=-\infty}^{\infty} A_{1n} H_n^{(1)}(k_\alpha r_1) e^{in\theta_1} = \phi_1^s(x, y) = \int_{-\infty}^{\infty} a_1(k) e^{ikx - v_\alpha y} dk, \quad (4.19)$$

$$\psi_1^s(r_1, \theta_1) = \sum_{n=-\infty}^{\infty} B_{1n} H_n^{(1)}(k_\beta r_1) e^{in\theta_1} = \psi_1^s(x, y) = \int_{-\infty}^{\infty} b_1(k) e^{ikx - v_\beta y} dk, \quad (4.20)$$

$$\phi_2^s(r_1, \theta_1) = \sum_{n=-\infty}^{\infty} A_{2n} J_n(k_\alpha r_1) e^{in\theta_1} = \phi_2^s(x, y) = \int_{-\infty}^{\infty} a_2(k) e^{ikx + v_\alpha y} dk, \quad (4.21)$$

$$\psi_2^s(r_1, \theta_1) = \sum_{n=-\infty}^{\infty} B_{2n} J_n(k_\beta r_1) e^{in\theta_1} = \psi_2^s(x, y) = \int_{-\infty}^{\infty} b_2(k) e^{ikx + v_\beta y} dk, \quad (4.22)$$

where

$$\begin{Bmatrix} a_1(k) \\ b_1(k) \end{Bmatrix} = \sum_{n=-\infty}^{\infty} \frac{i^{-n}}{i\pi} \begin{bmatrix} \zeta_{\alpha n}(h)/v_\alpha & 0 \\ 0 & \zeta_{\beta n}(h)/v_\beta \end{bmatrix} \begin{Bmatrix} A_{1n} \\ B_{1n} \end{Bmatrix}, \quad (4.23)$$

$$\begin{Bmatrix} A_{2n} \\ B_{2n} \end{Bmatrix} = \int_{-\infty}^{\infty} i^n \begin{bmatrix} \zeta_{\alpha n}(h) & 0 \\ 0 & \zeta_{\beta n}(h) \end{bmatrix} \begin{Bmatrix} a_2(k) \\ b_2(k) \end{Bmatrix} dk, \quad (4.24)$$

$$\zeta_{\alpha n}(h) = \left(\frac{k - v_\alpha}{k_\alpha}\right)^n e^{-v_\alpha h}, \quad (4.25)$$

$$\zeta_{\beta n}(h) = \left(\frac{k - v_\beta}{k_\beta}\right)^n e^{-v_\beta h}. \quad (4.26)$$

At the free surface $y = 0$ (or $y_1 = h$), zero-stress condition is written as

$$\begin{Bmatrix} \sigma_{yy} \\ \sigma_{xy} \end{Bmatrix}\Bigg|_{y=0} = \begin{Bmatrix} \lambda \nabla^2 \phi + 2\mu \left(\dfrac{\partial^2 \phi}{\partial y^2} - \dfrac{\partial^2 \psi}{\partial x \partial y}\right) \\ \mu \left(\dfrac{2\partial^2 \phi}{\partial x \partial y} + \dfrac{\partial^2 \psi}{\partial y^2} - \dfrac{\partial^2 \psi}{\partial x^2}\right) \end{Bmatrix}\Bigg|_{y=0} = \begin{Bmatrix} 0 \\ 0 \end{Bmatrix}. \quad (4.27)$$

Plugging Eqs. (4.19), (4.20), (4.21), and (4.22) into Eq. (4.27) to yield the relation between $(a_1(k), b_1(k))$ and $(a_2(k), b_2(k))$, in combination with Eqs. (4.23) and (4.24), we obtain a system of equations (*Lin et al.*, 2010):

$$\begin{Bmatrix} A_{2n} \\ B_{2n} \end{Bmatrix} = \sum_{m=-\infty}^{\infty} \mathbb{J}(m, n) \begin{Bmatrix} A_{1m} \\ B_{1m} \end{Bmatrix}, \quad (4.28)$$

where

$$\mathbb{J}(\boldsymbol{m},\boldsymbol{n}) = \frac{i^{n-m}}{i\pi} \int_{-\infty}^{\infty} \frac{1}{R(k)} \begin{bmatrix} P_{11}\zeta_{\alpha n}\zeta_{\alpha m}/\nu_{\alpha} & P_{12}\zeta_{\alpha n}\zeta_{\beta m}/\nu_{\beta} \\ P_{21}\zeta_{\beta n}\zeta_{\alpha m}/\nu_{\alpha} & P_{22}\zeta_{\beta n}\zeta_{\beta m}/\nu_{\beta} \end{bmatrix} dk , \qquad (4.29)$$

$$R(k) = (2k^2 - k_\beta^2)^2 - 4k^2\nu_\alpha\nu_\beta ,$$

$$P_{11} = P_{22} = -\left((2k^2 - k_\beta^2)^2 + 4k^2\nu_\alpha\nu_\beta\right) ,$$

$$P_{12} = -4ik(2k^2 - k_\beta^2)\nu_\beta ,$$

$$P_{21} = 4ik(2k^2 - k_\beta^2)\nu_\alpha ,$$

in which $R(k)$ is the familiar Rayleigh function.

4.3.5   Dirichlet boundary condition at cylinder interface

From the displacement potentials in Eqs. (4.16) and (4.17), the displacements are calculated as follows

$$\begin{Bmatrix} u_{r1} \\ u_{\theta 1} \end{Bmatrix} = \begin{Bmatrix} \dfrac{\partial\phi}{\partial r_1} + \dfrac{1}{r_1}\dfrac{\partial\psi}{\partial\theta_1} \\ \dfrac{1}{r_1}\dfrac{\partial\phi}{\partial\theta_1} - \dfrac{\partial\psi}{\partial r_1} \end{Bmatrix} = \sum_{n=-\infty}^{\infty} \mathbb{M}(\boldsymbol{n}) \begin{Bmatrix} A_{1n} \\ A_{2n} \\ B_{1n} \\ B_{2n} \end{Bmatrix} e^{in\theta_1} , \qquad (4.30)$$

where

$$\mathbb{M}(\boldsymbol{n}) = \begin{bmatrix} \partial/\partial r_1 & in/r_1 \\ in/r_1 & -\partial/\partial r_1 \end{bmatrix} \begin{bmatrix} H_n^{(1)}(k_\alpha r_1) & J_n(k_\alpha r_1) & 0 & 0 \\ 0 & 0 & H_n^{(1)}(k_\beta r_1) & J_n(k_\beta r_1) \end{bmatrix} . \qquad (4.31)$$

To find the impedance components K_{yy}, K_{xx}, and $K_{\theta x}$, boundary conditions as in Eqs. (4.7) and (4.8) are considered, which is a unitary displacement $u_{x1} = u_{y1} = 1$ being imposed at the circumference ($r_1 = a$) of the cylinder. Coordinate transformation gives

$$\begin{Bmatrix} u_{r1} \\ u_{\theta 1} \end{Bmatrix}\Bigg|_{r_1=a} = \begin{bmatrix} \cos\theta_1 & \sin\theta_1 \\ -\sin\theta_1 & \cos\theta_1 \end{bmatrix} \begin{Bmatrix} u_{x1} \\ u_{y1} \end{Bmatrix}\Bigg|_{r_1=a} = \begin{Bmatrix} \cos\theta_1 + \sin\theta_1 \\ \cos\theta_1 - \sin\theta_1 \end{Bmatrix}$$

$$= \frac{1}{2}\begin{Bmatrix} (1+i)e^{-i\theta_1} + (1-i)e^{i\theta_1} \\ (1-i)e^{-i\theta_1} + (1+i)e^{i\theta_1} \end{Bmatrix} . \qquad (4.32)$$

At $r_1 = a$, matching each coefficient to the $e^{in\theta_1}$ term in Eqs. (4.30) and (4.32), we obtain a system of equations

$$\mathbb{M}(n)|_{r_1=a} \begin{Bmatrix} A_{1n} \\ A_{2n} \\ B_{1n} \\ B_{2n} \end{Bmatrix} = \frac{1}{2} \begin{Bmatrix} (1+i)\delta_{(-1)(n)} + (1-i)\delta_{(1)(n)} \\ (1-i)\delta_{(-1)(n)} + (1+i)\delta_{(1)(n)} \end{Bmatrix} \quad \text{for each } n \in \mathbb{Z}, \quad (4.33)$$

where $\delta_{(-1)(n)}$ and $\delta_{(1)(n)}$ are the Kronecker delta functions.

To find the impedance components $K_{x\theta}$ and $K_{\theta\theta}$, boundary conditions as in Eqs. (4.9) and (4.10) are considered, which is a unitary torsional angle $\theta_1 = 1$ being imposed. Because $u_{\theta 1} = r_1\theta_1$, we have

$$\begin{Bmatrix} u_{r1} \\ u_{\theta 1} \end{Bmatrix}\Bigg|_{r_1=a} = \begin{Bmatrix} 0 \\ a \end{Bmatrix}. \quad (4.34)$$

At $r_1 = a$, matching each coefficient to the $e^{in\theta_1}$ terms in Eqs. (4.30) and (4.34), we have a system of equations

$$\mathbb{M}(n)|_{r_1=a} \begin{Bmatrix} A_{1n} \\ A_{2n} \\ B_{1n} \\ B_{2n} \end{Bmatrix} = \begin{Bmatrix} 0 \\ a\delta_{(0)(n)} \end{Bmatrix} \quad \text{for each } n \in \mathbb{Z}, \quad (4.35)$$

where $\delta_{(0)(n)}$ is the Kronecker delta function.

If the infinite series are truncated with $n \in [-N, N]$, we have $4 \times (2N+1)$ unknown coefficients A_{1n}, B_{1n}, A_{2n}, and B_{2n}. $2 \times (2N+1)$ equations come from the zeros-stress boundary condition in Eq. (4.28) while other $2 \times (2N+1)$ equations come from the Dirichlet boundary condition in Eq. (4.33) or (4.35). Solving this system of equations, we uniquely determine the displacement and stress fields of the soil domain.

4.3.6 Calculation of in-plane soil impedance functions

The stresses in the soil domain are computed as

$$
\left\{ \begin{array}{c} \sigma_{rr} \\ \sigma_{r\theta} \end{array} \right\} = \left\{ \begin{array}{c} \left(\lambda \nabla^2 \phi + 2\mu \dfrac{\partial^2 \phi}{\partial r_1^2} \right) + \dfrac{2\mu}{r_1^2} \left(r_1 \dfrac{\partial^2 \psi}{\partial r_1 \partial \theta_1} - \dfrac{\partial \psi}{\partial \theta_1} \right) \\[4mm] \dfrac{2\mu}{r_1^2} \left(r_1 \dfrac{\partial^2 \phi}{\partial r_1 \partial \theta_1} - \dfrac{\partial \phi}{\partial \theta_1} \right) + \mu \left(\dfrac{1}{r_1^2} \dfrac{\partial^2 \psi}{\partial \theta_1^2} + \dfrac{1}{r_1} \dfrac{\partial \psi}{\partial r_1} - \dfrac{\partial^2 \psi}{\partial r_1^2} \right) \end{array} \right\}.
\tag{4.36}
$$

After solving the system of equations for A_{1n}, B_{1n}, A_{2n}, and B_{2n}, then substituting the displacement potentials in Eqs. (4.16) and (4.17) into Eq. (4.36) yields

$$
\left\{ \begin{array}{c} \sigma_{rr} \\ \sigma_{r\theta} \end{array} \right\} = \frac{2\mu}{r_1^2} \sum_{n=-\infty}^{\infty} \begin{bmatrix} S_n^c & S_n^s \\ T_n^c & T_n^s \end{bmatrix} \left\{ \begin{array}{c} \cos{(n\theta_1)} \\ \sin{(n\theta_1)} \end{array} \right\},
\tag{4.37}
$$

where

$$
\left\{ \begin{array}{c} S_n^c \\ T_n^s \end{array} \right\} = \mathbb{E}_+^{(3)} \left(r_1, n \right) \left\{ \begin{array}{c} A_{1n} \\ i B_{1n} \end{array} \right\} + \mathbb{E}_+^{(1)} \left(r_1, n \right) \left\{ \begin{array}{c} A_{2n} \\ i B_{2n} \end{array} \right\},
\tag{4.38}
$$

$$
\left\{ \begin{array}{c} S_n^s \\ T_n^c \end{array} \right\} = \mathbb{E}_-^{(3)} \left(r_1, n \right) \left\{ \begin{array}{c} i A_{1n} \\ B_{1n} \end{array} \right\} + \mathbb{E}_-^{(1)} \left(r_1, n \right) \left\{ \begin{array}{c} i A_{2n} \\ B_{2n} \end{array} \right\}.
\tag{4.39}
$$

For $j = \{1, 3\}$, according to *Mow and Pao* (1971), we have

$$
\mathbb{E}_\pm^{(j)} \left(r_1, n \right) = \begin{bmatrix} E_{11,n}^{(j)} & \pm E_{12,n}^{(j)} \\[2mm] \pm E_{21,n}^{(j)} & E_{22,n}^{(j)} \end{bmatrix},
\tag{4.40}
$$

where

$$
\begin{aligned}
E_{11,n}^{(j)} &= \left(n^2 + n - k_\beta^2 r_1^2 / 2 \right) \mathscr{C}_n^{(j)}(k_\alpha r_1) - k_\alpha r_1 \mathscr{C}_{n-1}^{(j)}(k_\alpha r_1), \\
E_{12,n}^{(j)} &= -\left(n^2 + n \right) \mathscr{C}_n^{(j)}(k_\beta r_1) + n k_\beta r_1 \mathscr{C}_{n-1}^{(j)}(k_\beta r_1), \\
E_{21,n}^{(j)} &= \left(n^2 + n \right) \mathscr{C}_n^{(j)}(k_\alpha r_1) - n k_\alpha r_1 \mathscr{C}_{n-1}^{(j)}(k_\alpha r_1), \\
E_{22,n}^{(j)} &= -\left(n^2 + n - k_\beta^2 r_1^2 / 2 \right) \mathscr{C}_n^{(j)}(k_\beta r_1) + k_\beta r_1 \mathscr{C}_{n-1}^{(j)}(k_\beta r_1),
\end{aligned}
\tag{4.41}
$$

with $\mathscr{C}_n^{(j)}$ representing the Bessel and Hankel functions: $\mathscr{C}_n^{(1)} = J_n$ and $\mathscr{C}_n^{(3)} = H_n^{(1)}$.

The resultant forces and moment per unit length at the centroid of the cylinder are computed by integrating the stresses at the cylinder boundary

$$F_{x1} = \int_{-\pi}^{\pi} (\sigma_{rr} \cos \theta_1 - \sigma_{r\theta} \sin \theta_1)|_{r_1=a} \, a \mathrm{d}\theta_1 \,,$$

$$F_{y1} = \int_{-\pi}^{\pi} (\sigma_{rr} \sin \theta_1 + \sigma_{r\theta} \cos \theta_1)|_{r_1=a} \, a \mathrm{d}\theta_1 \,,$$

$$M = \int_{-\pi}^{\pi} \sigma_{r\theta}|_{r_1=a} \, a^2 \mathrm{d}\theta_1 \,. \tag{4.42}$$

Substituting Eq. (4.37) into Eq. (4.42) and using the orthogonality property of sine and cosine, we obtain after integration

$$F_{x1} = \frac{2\pi\mu}{a} \left(S_{-1}^c + S_1^c + T_{-1}^s - T_1^s \right) \,,$$

$$F_{y1} = \frac{2\pi\mu}{a} \left(-S_{-1}^s + S_1^s + T_{-1}^c + T_1^c \right) \,,$$

$$M = 4\pi\mu T_0^c \,. \tag{4.43}$$

Clearly, only the modes with $n = \pm 1$ contribute to resultant forces F_{x1} and F_{y1}, whereas only the mode with $n = 0$ contributes to resultant moment M. Note that F_{x1}, F_{y1}, and M are complex numbers.

Solving the problem with boundary conditions in Eqs. (4.7) and (4.8), we get $K_{yy} = F_{y1}$, $K_{xx} = F_{x1}$, and $K_{\theta x} = M/a$. Whereas, solving the problem with boundary conditions in Eqs. (4.9) and (4.10), we get $K_{x\theta} = F_{x1}/a$ and $K_{\theta\theta} = M/a^2$.

4.3.7 Integration contour

The primary task here is to evaluate the integrals appeared in the matrix $\mathbb{J}(m, n)$ in Eq. (4.29), which are technically the inverse Fourier transform from wavenumber domain into spatial domain. The main difficulty in the integral evaluation arises from the existence of branch points and poles. The branch points are due to the square roots $\nu_0 = \sqrt{k^2 - k_0^2}$ where (k_0, ν_0) represents either (k_α, ν_α) or (k_β, ν_β). The poles, meanwhile, arise from the roots of Rayleigh function $R(k) = (2k^2 - k_\beta^2)^2 - 4k^2\nu_\alpha\nu_\beta$, denoted as $\pm k_R$.

To evaluate the integral, contour integration along the real axis should be performed in the complex k-plane. Due to branch points, a physical Riemann surface with branch cuts must be defined to make the integrands unique. To this end, we let $\nu_0 = \nu_r + i\nu_i$, $k = k_r + ik_i$, $k_0 = \xi_r + i\xi_i$, where $\nu_r, \nu_i, k_r, k_i, \xi_r, \xi_i \in \mathbb{R}$ and $\xi_r, \xi_i > 0$. We then plug these relations into

$v_0 = \sqrt{k^2 - k_0^2}$, square and equalize the real and imaginary parts to obtain

$$v_r^2 - v_i^2 = k_r^2 - k_i^2 - \xi_r^2 + \xi_i^2, \tag{4.44}$$

$$v_r v_i = k_r k_i - \xi_r \xi_i. \tag{4.45}$$

From the representation of Hankel function in Eq. (4.18), the physical and causal reasoning lead to $v_r > 0$ (the wave cannot grow exponentially) and $v_i < 0$ (outgoing cylindrical wave, recall that the time factor is $e^{-i\omega t}$). Physical Riemann sheet requires $v_r > 0$, with the branch cuts defined by $v_r = 0$ (*DeSanto*, 1992), then Eq. (4.45) yields $k_r k_i = \xi_r \xi_i$. The branch cuts lie on two hyperbolas passing through the branch points $\pm k_0$. With $v_r = 0$ and $v_i < 0$, Eq. (4.44) leads to $k_r^2 - k_i^2 - \xi_r^2 + \xi_i^2 < 0$, thus we choose the branches of hyperbolas having k_i approaching $\pm\infty$, which are displayed in solid lines in Fig. 4.3(a).
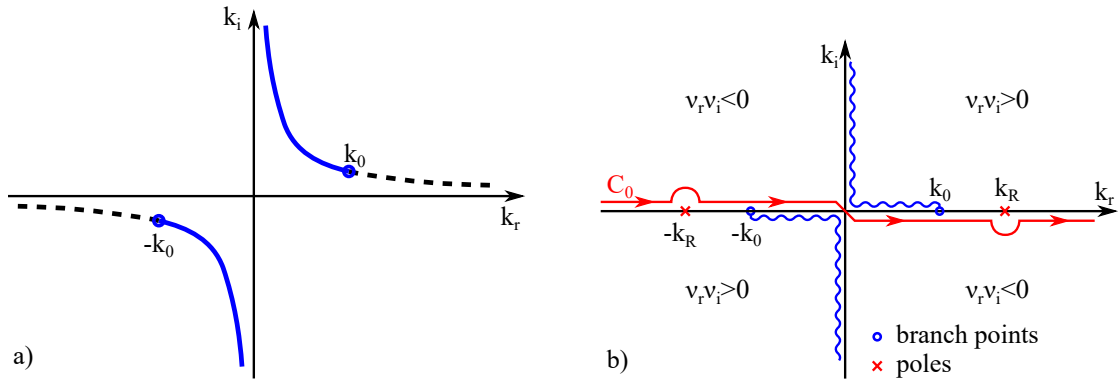
Figure 4.3: The branch cuts and the integration contour.

In the limit at $\xi_i \to 0$, the branch points and branch cuts are shown in Fig. 4.3(b). In the first and third quadrants, $k_r k_i - \xi_r \xi_i > 0$, Eq. (4.45) results in $v_r v_i > 0$. Whereas in the second and fourth quadrants, $k_r k_i - \xi_r \xi_i < 0$, thus $v_r v_i < 0$. The proper regions satisfying physical and causal reasoning must have $v_r v_i < 0$, therefore, the contour C_0 for the integration lies on the second and fourth quadrants (see Fig. 4.3b). Along the real axis, the single-value function of v_0 on the physical Riemann surface is defined as:

$$v_0 = \begin{cases} \sqrt{k^2 - k_0^2} & \text{for } |k| > k_0 \\ -i\sqrt{k_0^2 - k^2} & \text{for } |k| < k_0 \end{cases}. \tag{4.46}$$

4.3.8   Direct evaluation of the integral

Because the branch cuts are not straightforward and Jordan's Lemma does not hold, there is no benefit trying to close the contour and indirectly evaluate the integrals in Eq. (4.29)

via residue theorem. Instead, we calculated the integrals directly along the real axis of wavenumber. The singularities caused by the branch points $\pm k_\alpha$ and $\pm k_\beta$ were removed by changing of variables. *Lin et al.* (2010) used L'Hopital's rule to approximate the principle value of the integral around Rayleigh poles $\pm k_R$, considering a discontinuous integration path along the real axis of wavenumber. However, the integration path should be a continuous one on the complex-plane of the wavenumber k, and thus the integral around Rayleigh poles was incorrectly estimated by using the principle value. This study used Cauchy's residue theorem to compute the integral along the semi-circles centered at Rayleigh poles $\pm k_R$ (Fig. 4.3b).
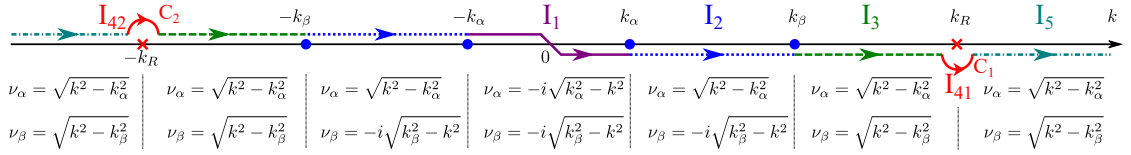
Figure 4.4: The integration components.

One element of $\mathbb{J}(m, n)$ was chosen to illustrate the calculation procedure:

$$J_{11} = \int_{-\infty}^{\infty} \frac{1}{R(k)} \frac{P_{11}\zeta_{\alpha n}\zeta_{\alpha m}}{\nu_\alpha} dk .$$ (4.47)

Fig. 4.4 displays the integration components over different regions with corresponding values of ν_α and ν_β. Eq. (4.47) is rewritten as

$$J_{11} = \left(\int_{-\infty}^{-k_R-\delta} + \int_{C_2} + \int_{-k_R+\delta}^{-k_\beta} + \int_{-k_\beta}^{-k_\alpha} + \int_{-k_\alpha}^{k_\alpha} + \int_{k_\alpha}^{k_\beta} + \int_{k_\beta}^{k_R-\delta} + \int_{C_1} + \int_{k_R+\delta}^{\infty} \right) (\cdot)$$

$$= \underbrace{\int_{-k_\alpha}^{k_\alpha} (\cdot)}_{I_1} + \underbrace{\left(\int_{-k_\beta}^{-k_\alpha} + \int_{k_\alpha}^{k_\beta} \right) (\cdot)}_{I_2} + \underbrace{\left(\int_{-k_R+\delta}^{-k_\beta} + \int_{k_\beta}^{k_R-\delta} \right) (\cdot)}_{I_3} + \underbrace{\int_{C_1} (\cdot)}_{I_{41}} + \underbrace{\int_{C_2} (\cdot)}_{I_{42}} +$$

$$\underbrace{\left(\int_{-\infty}^{-k_R-\delta} + \int_{k_R+\delta}^{\infty} \right) (\cdot)}_{I_5}$$

$$= I_1 + I_2 + I_3 + I_{41} + I_{42} + I_5 ,$$ (4.48)

where C_1 and C_2 are semi-circles with very small radius δ.

For I_1, $\nu_\alpha = -i\sqrt{k_\alpha^2 - k^2}$ and $\nu_\beta = -i\sqrt{k_\beta^2 - k^2}$. Let $\xi = k/k_\alpha$ and $r_0 = k_\beta/k_\alpha$, I_1 is

rewritten as

$$I_1 = \int_{-1}^{1} \frac{-i}{\sqrt{1-\xi^2}} \frac{\left(2\xi^2 - r_0^2\right)^2 - 4\xi^2\sqrt{1-\xi^2}\sqrt{r_0^2 - \xi^2}}{\left(2\xi^2 - r_0^2\right)^2 + 4\xi^2\sqrt{1-\xi^2}\sqrt{r_0^2 - \xi^2}} \left(\xi + i\sqrt{1-\xi^2}\right)^{n+m} e^{i2hk_\alpha\sqrt{1-\xi^2}} \mathrm{d}\xi .$$

(4.49)

I_1 has weight function $1/\sqrt{1-\xi^2}$ and normally can be evaluated with Gauss–Chebyshev quadrature rule. This study used nested Gauss–Kronrod quadrature rule (*Kronrod*, 1965), which is computationally cheaper because the higher-order estimates are computed by reusing the function values at nodes of the lower-order estimates. The nested rule also provides the approximation error by computing the difference between higher- and lower-order estimates.

For I_2, simple algebraic manipulation yields

$$I_2 = \int_{k_\alpha}^{k_\beta} -\frac{\left(2k^2 - k_\beta^2\right)^2 + 4k^2 v_\alpha v_\beta}{\left(2k^2 - k_\beta^2\right)^2 - 4k^2 v_\alpha v_\beta} \frac{e^{-2hv_\alpha}}{v_\alpha} \left[\left(\frac{k - v_\alpha}{k_\alpha}\right)^{n+m} + \left(\frac{-k - v_\alpha}{k_\alpha}\right)^{n+m}\right] \mathrm{d}k , \quad (4.50)$$

where $v_\alpha = \sqrt{k^2 - k_\alpha^2}$ and $v_\beta = -i\sqrt{k_\beta^2 - k^2}$. The singularity at k_α is removed by change of variable. We let $v = \sqrt{k^2 - k_\alpha^2} = v_\alpha$. Thus, $k = \sqrt{v^2 + k_\alpha^2}$ and $\mathrm{d}k = \frac{v\mathrm{d}v}{\sqrt{v^2 + k_\alpha^2}}$. I_2 is then expressed as

$$I_2 = \int_0^{\sqrt{k_\beta^2 - k_\alpha^2}} -\frac{\left[2\left(v^2 + k_\alpha^2\right) - k_\beta^2\right]^2 + 4\left(v^2 + k_\alpha^2\right) v \left(-i\sqrt{k_\beta^2 - v^2 - k_\alpha^2}\right)}{\left[2\left(v^2 + k_\alpha^2\right) - k_\beta^2\right]^2 - 4\left(v^2 + k_\alpha^2\right) v \left(-i\sqrt{k_\beta^2 - v^2 - k_\alpha^2}\right)} \times$$
$$e^{-2hv} \left[\left(\frac{\sqrt{v^2 + k_\alpha^2} - v}{k_\alpha}\right)^{n+m} + \left(\frac{-\sqrt{v^2 + k_\alpha^2} - v}{k_\alpha}\right)^{n+m}\right] \frac{\mathrm{d}v}{\sqrt{v^2 + k_\alpha^2}} , \quad (4.51)$$

and subsequently computed by Gauss–Kronrod quadrature rule.

For I_3, I_{41}, I_{42}, and I_5, $v_\alpha = \sqrt{k^2 - k_\alpha^2}$ and $v_\beta = \sqrt{k^2 - k_\beta^2}$. There is no singularity in the integrand of I_3 , thus no further manipulation is required and I_3 was calculated directly by Gauss–Kronrod quadrature rule. As regards the improper integral I_5, numerical calculations showed that it is convergent and the integral exists, therefore it was estimated also by Gauss–Kronrod quadrature rule. Whereas, the counterclockwise integral I_{41} and clockwise integral I_{42} were computed by Cauchy's residue theorem as

$$I_{41} = i\pi a_{-1} , \quad (4.52)$$

$$I_{42} = -i\pi a_{-1}^* , \quad (4.53)$$

where a_{-1} and a^*_{-1} are the residues at the simple poles k_R and $-k_R$, respectively. They are computed as

$$a_{-1} = \left(\frac{1}{\partial R(k)/\partial k} \frac{P_{11} \zeta_{\alpha n} \zeta_{\alpha m}}{\nu_\alpha} \right) \Bigg|_{k=k_R}, \tag{4.54}$$

$$a^*_{-1} = \left(\frac{1}{\partial R(k)/\partial k} \frac{P_{11} \zeta_{\alpha n} \zeta_{\alpha m}}{\nu_\alpha} \right) \Bigg|_{k=-k_R}. \tag{4.55}$$

Other elements of $\mathbb{J}(m, n)$ were calculated in a similar manner.

In this study, the absolute and relative error tolerance in the Gauss–Kronrod quadrature rule are 10^{-10} and 10^{-6}, respectively. The radius of two semi-circles C_1 and C_2 are $\delta = 10^{-8}$ m.

For cylinders with very large burial depth h, the integrals I_1 and I_2 in Eq. (4.48) contain exponential functions with large imaginary exponents and evolve into high oscillatory integrals. Such high oscillatory integrals cannot be evaluated using classical Gaussian quadrature rule because of the highly computational cost. Instead, we used the asymptotic method, presented in Appendix A.

4.3.9 Truncation errors

The analytical solution is based on the Hankel– and Bessel–Fourier infinite series expansion. We truncated the series at a chosen value of N and solved a system of equations of $4 \times (2N+1)$ unknown coefficients to obtain the approximated solution. The value of N is determined by the series terms that have negligible effect on the computed displacement and stress fields. When N is larger, the approximated solution converges to the exact solution of SIFs.

We tested the convergence rate of the solution with respect to N for the case: $h/a = 2.36$, $\mu = 4.5$ MPa, $\nu = 0.25$, $\rho = 1800$ kg/m^3, and $a = 1.28$ m. Fig. 4.5 shows the normalized impedance K_{xx} calculated with different value of N as a function of dimensionless frequency $a_0 = a\omega/c_\beta$. Observably, the solutions converge quickly with increasing value of N, in which those obtained with $N = 5$, $N = 8$, and $N = 10$ are visually indistinguishable.

To quantify the rate of convergence, we computed the L^2-norm of the error $|E|_{L^2}$, expressed as

$$|E|_{L^2} = \frac{1}{\mu} \sqrt{\sum_{j=10}^{400} \left[K^N(a_0^j) - K^{10}(a_0^j) \right]^2 \Delta a_0}, \tag{4.56}$$

where $K^N(a_0^j)$ is the value of the impedance component $\{K_{yy}, K_{xx}, K_{\theta\theta}, K_{x\theta}, K_{\theta x}\}$, either real or imaginary part, obtained by truncating the series at N. $K^N(a_0^j)$ is evaluated at $a_0^j = j\Delta a_0$, where $\Delta a_0 = 0.01$. From the previous observation, solution with $N = 10$,
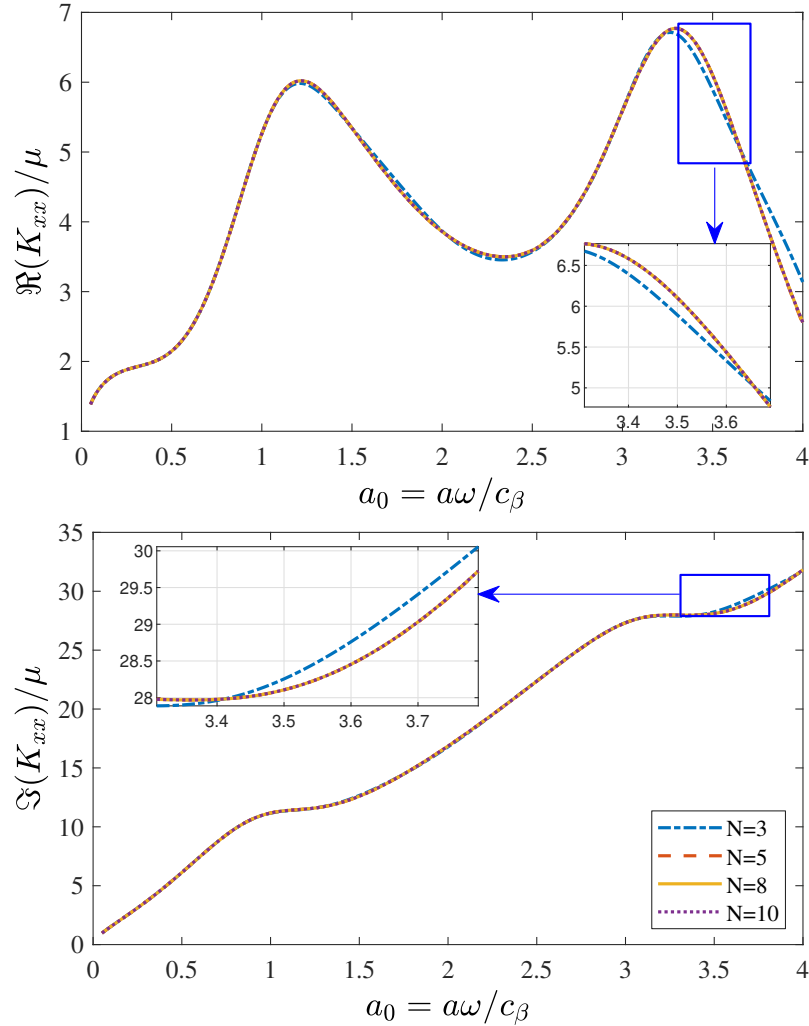
Figure 4.5: Convergence of series truncation for real and imaginary parts of K_{xx}.

denoted as $K^{10}(a_0^j)$, was chosen as the exact solution. Fig. 4.6 shows the errors of real and imaginary parts of five impedance components for different values of N (10 error values for each N). The least-squares regression line illustrates that the error decays rapidly with increasing N. Besides, the truncation yielded highly accurate results with $N = 8$ and, therefore, it was used as the reference/analytical solution from now on.

4.4 Finite element analysis for soil impedance functions of homogeneous and two-layered half-spaces

4.4.1 Numerical computation of in-plane soil impedance functions

Seylabi et al. (2016) developed a method to extract the impedance functions of a semi-infinite half-space from a FE model in time domain. The approach is general enough to be
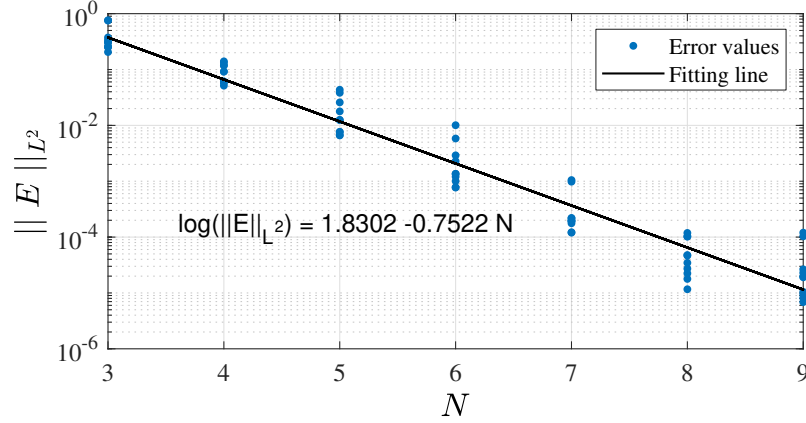
Figure 4.6: Rate of convergence.

applied equally well to flexible interfaces as well as three-dimensional problems. This study considered a rigid interface and a two-dimensional plane-strain problem as in Fig. 4.7.

(a)   (b)
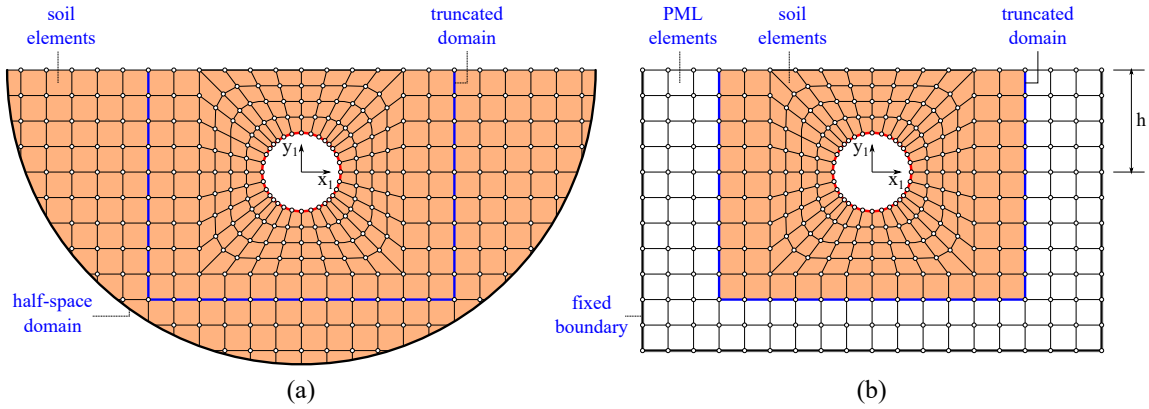
Figure 4.7: Numerical model for the estimation of SIFs: (a) infinite half-space FE model; and (b) truncated half-space FE model using PML elements.

We used flexibility method to compute the compliance matrix, in which force-displacement relations are expressed in matrix form in frequency domain as

$$
\begin{bmatrix}
\hat{G}_{yy} & 0 & 0 \\
0 & \hat{G}_{xx} & \hat{G}_{x\theta} \\
0 & \hat{G}_{\theta x} & \hat{G}_{\theta\theta}
\end{bmatrix}
\begin{bmatrix}
\hat{F}_{y1} \\
\hat{F}_{x1} \\
\hat{M}/a
\end{bmatrix}
=
\begin{bmatrix}
\hat{u}_{y1} \\
\hat{u}_{x1} \\
a\,\hat{\theta}_1
\end{bmatrix},
\tag{4.57}
$$

Each component of the compliance matrix was computed using a time domain FE analysis. To do so, we applied force time histories $F_{y1}(t)$, $F_{x1}(t)$, and $M(t)$, and recorded the resulting displacements $u_{y1}(t)$, $u_{x1}(t)$ and the rotation $\theta_1(t)$. The following procedure should be performed:

1. Apply $F_{y1}(t) \neq 0$, $F_{x1}(t) = 0$, and $M(t) = 0$; then record $u_{y1}(t)$. Use Fourier transform (FT) to compute $\hat{F}_{y1}$ and $\hat{u}_{y1}$. Compute $\hat{G}_{yy} = \hat{u}_{y1}/\hat{F}_{y1}$.

2. Apply $F_{y1}(t) = 0$, $F_{x1}(t) \neq 0$, and $M(t) = 0$; then record $u_{x1}(t)$ and $\theta_1(t)$. Use FT to compute $\hat{F}_{x1}$, $\hat{u}_{x1}$ and $\hat{\theta}_1$. Compute $\hat{G}_{xx} = \hat{u}_{x1}/\hat{F}_{x1}$ and $\hat{G}_{\theta x} = a\hat{\theta}_1/\hat{F}_{x1}$.

3. Apply $F_{y1}(t) = 0$, $F_{x1}(t) = 0$, and $M(t) \neq 0$; then record $u_{x1}(t)$ and $\theta_1(t)$. Use FT to compute $\hat{M}$, $\hat{u}_{x1}$ and $\hat{\theta}_1$. Compute $\hat{G}_{x\theta} = a\hat{u}_{x1}/\hat{M}$ and $\hat{G}_{\theta\theta} = a^2\hat{\theta}_1/\hat{M}$.

4. Inverse compliance matrix to obtain impedance matrix.

Note that it may be necessary to apply zero-padding to time signals of the applied force and resulting displacement before performing FT to increase the resolution of the calculated impedance.

4.4.2   Finite element models

4.4.2.1   Input signal for time domain analyses

To achieve SIF over a wide range of frequency, the energy of the input force (or moment) signal should be distributed over the corresponding frequency band. A Ricker wavelet was chosen to fulfil this requirement, with the applied force (or moment) time histories $F(t)$ calculated as

$$F(t) = F_0 \left[2\pi^2 f_c^2 (t - t_0)^2 - 1 \right] e^{-\pi^2 f_c^2 (t-t_0)^2}, \qquad (4.58)$$

where F_0 is the amplitude of the applied force (or moment), f_c is the central frequency of the signal, and t_0 is the time when the maximum amplitude occurs. This study used $F_0 = 1$ kN (or kN.cm), $f_c = 15$ Hz, and $t_0 = 0.2$ sec. The generated Ricker wavelet using these values is shown in Fig. 4.8. As one may see, the signal energy is distributed over a broad band from 0 to 40 Hz, which will eventually yield the SIF over this frequency band.
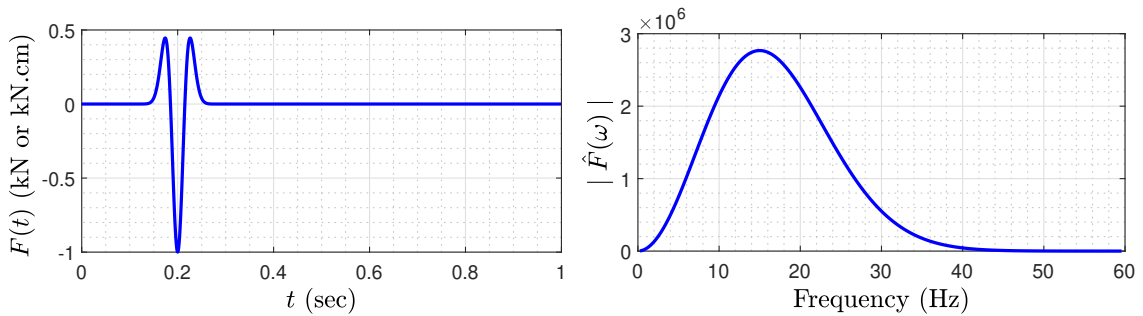
Figure 4.8: The applied force (or moment) in time and frequency domain.

4.4.2.2 Spatial-temporal discretization

The plane-strain infinite half-space was discretized and truncated by FE approach in combination with absorbing boundaries. To avoid the spurious waves reflected from the far-field boundaries, we used PML elements (*Basu*, 2009) as in Fig. 4.7. The analyses were conducted with 3D LS-DYNA R10.0.0 solver.

In wave propagation problems, large mesh size removes short-wavelength (high-frequency) energy, whereas excessively small size results in high computational cost and numerical instability. Therefore, the element dimension d_e must be chosen appropriately as $d_e = \lambda_{min}/n_{epw}$, where λ_{min} is the minimum wavelength and n_{epw} is the number of elements per wavelength. The minimum wavelength is calculated as $\lambda_{min} = c_\beta/f_{max}$, where f_{max} is the highest frequency of the interested signal. Previous studies have used at least $n_{epw} = 10$ to adequately simulate the wave problems (*Seron et al.*, 1996). To achieve higher accuracy while maintaining the computational efficiency, we adopted unstructured quadrilateral grid mesh having $n_{epw} = 40$ near the cylinder boundary and $n_{epw} = 15$ near the boundary of the truncated domain.

Time integration was evaluated with the explicit central difference scheme, in which the critical time step Δt_c was chosen based on the Courant–Friedrichs–Lewy condition $\Delta t_c = d_e/c_\alpha$. This study used a time step size of $\Delta t = 0.9\Delta t_c$. Moreover, the sampling rate of discrete displacements computed at each time step should be sufficiently dense to capture all the information of the interested signal up to the highest frequency. According to Nyquist–Shannon sampling theorem, we enforced $\Delta t < 0.5/f_{max}$.

Furthermore, termination time should be long enough to include the P- and SV-waves bouncing back and forth between the free surface and the cylinder boundary until they become negligible. To stress the importance of the later statement, we consider a cylinder with outside radius of $a = 1.28$ m, a shear modulus, Poisson's ratio, and density of homogeneous half-space of $\mu = 4.5$ MPa, $\nu = 0.25$, and $\rho = 1800$ kg/m^3, respectively. In Fig. 4.9, we present a possible error in the frequency spectrum of displacement time history due to insufficiently recorded response. Fig. 4.9(a) shows a 3.0-second resulting displacement in time domain for $h/a = 16$, while Fig. 4.9(b) shows the frequency domain of the displacement signals truncated at 1.0, 1.5, 2.0, and 3.0 sec from the original signal. Clearly, the 1.0-second truncated signal misses some energy from the first and second bounce of P- and SV-waves from the free surface, causing the discrepancy in the frequency content. When the displacement is recorded up to 1.5 and 2.0 sec, the first and second bounce, respectively, are completely accounted for, the frequency spectra closely approach that of the 3.0-second signal. Because P-waves are faster than SV-waves, the termination time
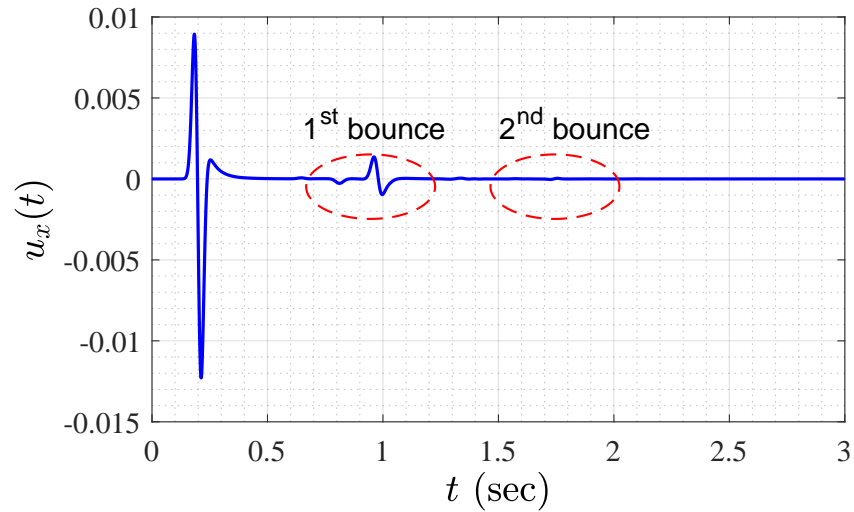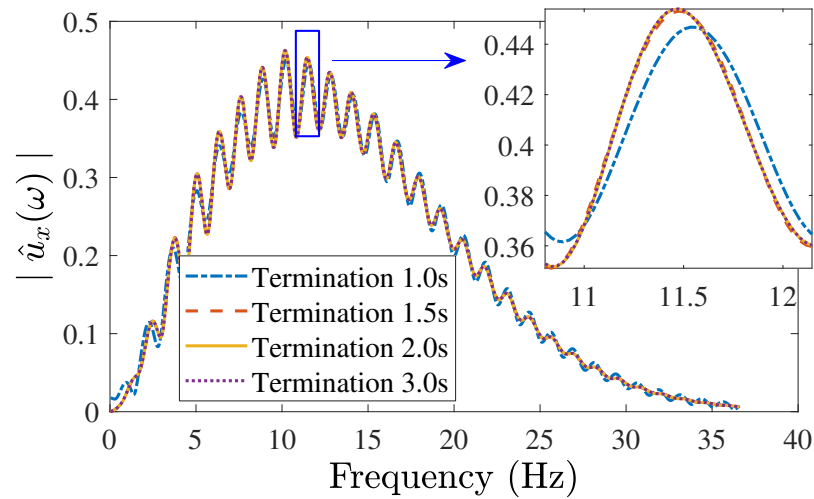
Figure 4.9: Displacement signal for $h/a = 16$ in: (a) time domain; and (b) frequency domain.

should be enough for the displacement signal to consist at least two bounces of SV-waves. Whereas, the excitation force needs to be loaded and totally unloaded within termination time, roughly taken as 1.0 sec. Therefore, termination time was chosen as $5h/c_\beta$ or 1.0 sec, whichever is larger.

4.5 Verification

For the FE analyses in Section 4.5 and Section 4.6, the input parameters are as follows: the outside radius of the cylinder is $a = 1.28$ m; the shear modulus, Poisson's ratio, and density

of homogeneous half-space are taken as $\mu = 4.5$ MPa, $\nu = 0.25$, and $\rho = 1800$ kg/m^3, respectively, unless otherwise noticed.

Case 1: $h/a = 2.36$. The analytical solution in Section 4.3 and the FE analysis in Section 4.4 for the SIFs of homogeneous half-space were compared with the results by *Seylabi et al.* (2016). Fig. 4.10 shows that those results agree very well. $K_{\theta x} = K_{x\theta}$ was verified and therefore it was unnecessary to plot $K_{\theta x}$.

Case 2: $h/a \to \infty$. Fig. 4.11 shows the SIFs obtained by the analytical solution in Section 4.3 for $h/a \to \infty$, e.g., $h/a = 10^6$. It also shows the horizontal impedance K_h and torsional impedance K_t of plane-strain full-space problems, proposed by *Novak et al.* (1978). When the burial depth is very large, the reflected P- and SV-waves from the free surface have negligible effect on the cylinder. As expected, the half-space problem converges to the full-space problem with $K_{yy} = K_{xx} = K_h$ and $K_{\theta\theta} = K_t$. Meanwhile, there is no coupling between horizontal and torsional motions because of the symmetry of geometry and applied load, leading to $K_{x\theta} = K_{\theta x} = 0$ as shown in the graphs.

4.6 Homogeneous half-space

We used the analytical solution in Section 4.3 to investigate the effect of burial depth and Poisson's ratio on the SIFs of homogeneous linear half-space.

4.6.1 Effect of burial depth

Fig. 4.12 shows the real and imaginary parts of SIF components K_{xx}, K_{yy}, $K_{\theta\theta}$, and $K_{x\theta}$ for $h/a = \{4, 8, 12, 16, \infty\}$ and Poisson's ratio $\nu = 0.25$. SIFs of homogeneous full-space by *Novak et al.* (1978) also are plotted for comparison.

Overall, the SIF components of half-space oscillate about their counterparts of full-space. These oscillations are attributed to the reflected P- and SV-waves from the half-space free surface, in which wave interference within the region between the cylinder and free surface leads to the constructive and destructive effects of the SIFs. Therefore, the characteristic of this oscillation substantially depends on the burial depth h. For each of the impedance components in Fig. 4.12, the amplitude of the oscillation gradually decreases with the increasing burial depth. It is because the reflected waves dissipate their energy while propagating and could not considerably alter the pre-existing displacement and stress fields around the cylinder. Besides, the frequency of oscillation is lowest in case of smallest burial depth $h/a = 4$. At the cylinder boundary Γ_b, the phase difference between the vibrating source (the imposed vibration at Γ_b) and the reflected waves from the free surface is larger with larger burial depth, causing the SIFs to oscillate with higher frequencies.
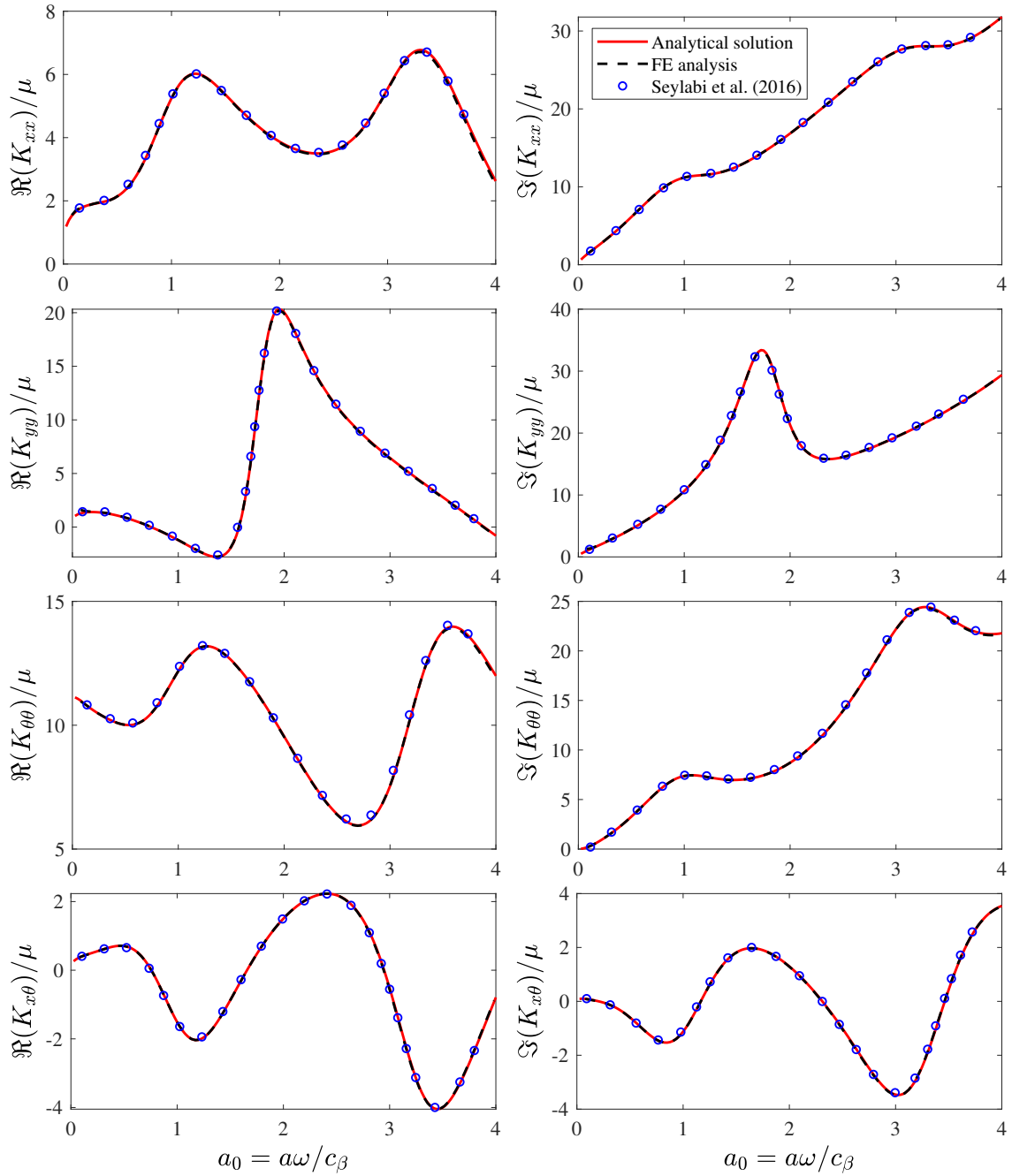
Figure 4.10: The SIFs for $h/a = 2.36$.

When $h/a \to \infty$, e.g., $h/a = 10^6$, the effect of reflected waves is negligible, each of the SIF components K_{xx}, K_{yy}, or $K_{\theta\theta}$ converges to its full-space counterpart, as displayed in Fig. 4.12.

One case of burial depth $h/a = 4$, where the largest constructive and destructive effects occur, is analyzed. The constructive effect might induce an increase in translational impedance
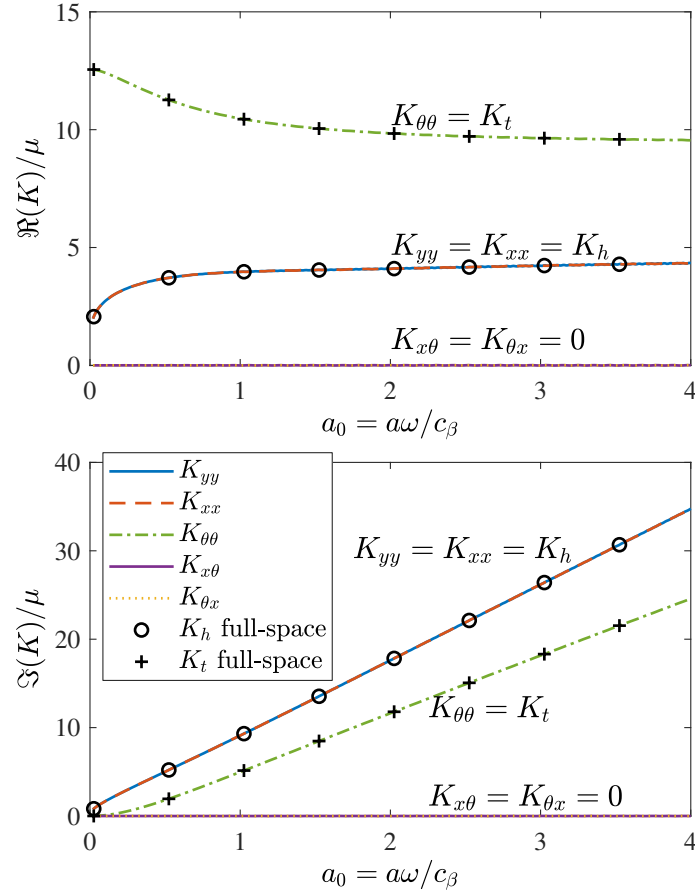
Figure 4.11: The SIFs for $h/a \to \infty$.

$\Re(K_{xx})$ and $\Re(K_{yy})$ up to approximately 3 times and 2.5 times, respectively, compared with that of full-space domain. Whereas, a smaller increase, up to 1.5 times, is observed for torsional impedance $\Re(K_{\theta\theta})$. Similar trend occurs in other cases of burial depth, in which the constructive and destructive effects are more pronounced for translational impedance than for torsional one. Accordingly, the translational impedance is more sensitive to the burial depth.

For each impedance component K_{xx}, K_{yy}, and $K_{\theta\theta}$, the fluctuation amplitude of real part around corresponding full-space impedance is more considerable than that of imaginary part. It indicates that the burial depth impacts the real part (soil stiffness) to a greater extent than the imaginary part (dashpot damping coefficient). However, the fluctuation amplitude is similar in both real and imaginary parts for $K_{x\theta}$, demonstrating the same level of impact that burial depth has on those real and imaginary parts.

Additionally, because of half-space configuration, there is geometric coupling behavior between translational motion along x-axis and torsional motion about the centroid of the
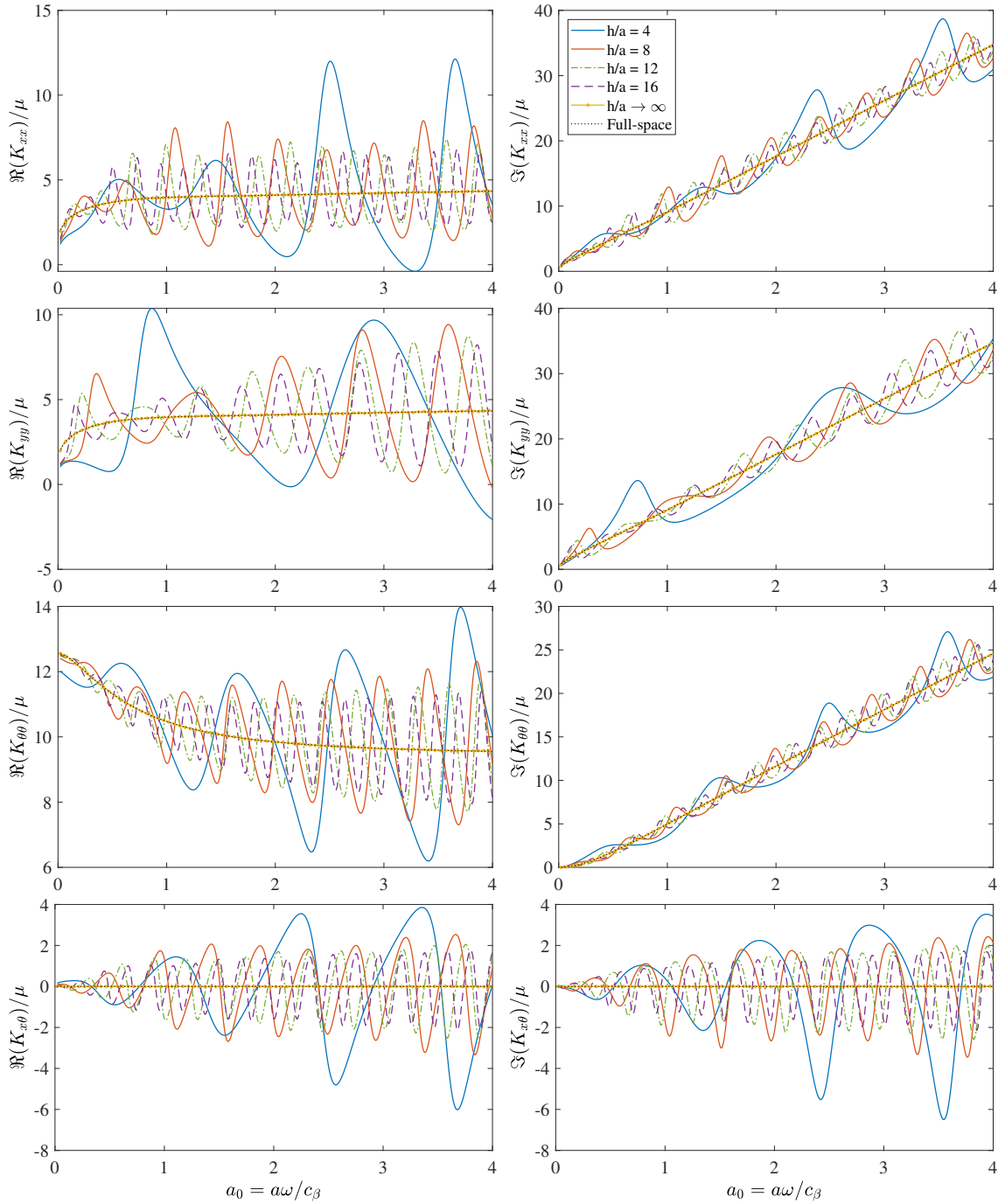
Figure 4.12: The SIFs for $\nu = 0.25$ and different values of burial depth h/a.

cylinder, indicated by non-zero values of $K_{x\theta} = K_{\theta x}$. For a particular configuration of h/a, the real and imaginary parts of coupling components are generally much smaller than that of translational and torsional components. Besides, the coupling is small in low-frequency regime, e.g., $a_0 < 0.5$, but becomes considerable with higher frequency. When burial depth is very large, the geometry becomes symmetric with respect to x-axis, and thus the coupling

disappears $K_{x\theta} = K_{\theta x} = 0$, which is similar to the full-space problem.

4.6.2 Effect of Poisson's ratio

In this section, we investigated the sensitivity of SIFs to Poisson's ratio. Fig. 4.13 shows the SIFs for different values of Poisson's ratio $\nu = \{0.25, 0.30, 0.35, 0.40, 0.45\}$ and $h/a = 4$. While the Poisson's ratio significantly affects the translational impedance K_{xx} and K_{yy}, it has almost no impact on the torsional impedance $K_{\theta\theta}$. This phenomenon is associated with the type of wave propagating in the half-space. The translational impedance is mostly related to the propagation of P-wave whose velocity is a function of Poisson's ratio. Whereas, the torsional impedance is mainly associated with the propagation of SV-wave whose velocity does not depend on Poisson's ratio. Besides, in low dimensionless frequency regime, e.g., $a_0 < 0.5$, the variation in Poisson's ratio does not have any significant effect on SIF components K_{xx}, K_{yy}, $K_{\theta\theta}$, and $K_{x\theta}$. When the frequency is larger, the translational impedance K_{xx} and K_{yy} are more sensitive to the variation of Poisson's ratio compared with the case of lower frequency.

4.7 Two-layered half-space

In this section, we used the FE approach described in Section 4.4 to generate SIFs for two-layered soil stratum. The geometry of the problem is displayed in Fig. 4.14, in which h_1 and h_2 are the distances from the center of the cylinder to the top of soil layer 1 and layer 2, respectively.

To investigate the effect of two-layered half-space, we consider both soil layers to have same values of mass density $\rho = 1800$ kg/m^3 and Poisson's ratio $\nu = 0.25$, but different values of shear modulus, μ_1 compared with μ_2. In addition, to quantify the discrepancy between the in-plane SIFs of a two-layered domain and that of a homogeneous half-space, we calculated the dimensionless area $\mathcal{A}$ bounded by these two curves. Without loss of generality, we considered the real part of K_{yy} with the area $\mathcal{A}$ expressed as

$$\mathcal{A} = \frac{1}{\mu_1} \int_{0.1}^{4} \left| \Re\left(K_{yy}\right) - \Re\left(K_{yy}^{ho}\right) \right| da_0, \tag{4.59}$$

where K_{yy} is the impedance component of a two-layered domain and K_{yy}^{ho} is the component of the corresponding homogeneous half-space. This dimensionless area $\mathcal{A}$ is physically illustrated by the shaded area in Fig. 4.15, and its values are quantified in Table 4.1 for different configurations of h_1/a, h_2/a, and μ_1/μ_2 with fixed values of $\mu_1 = 4.5$ MPa and $a = 1.28$ m.
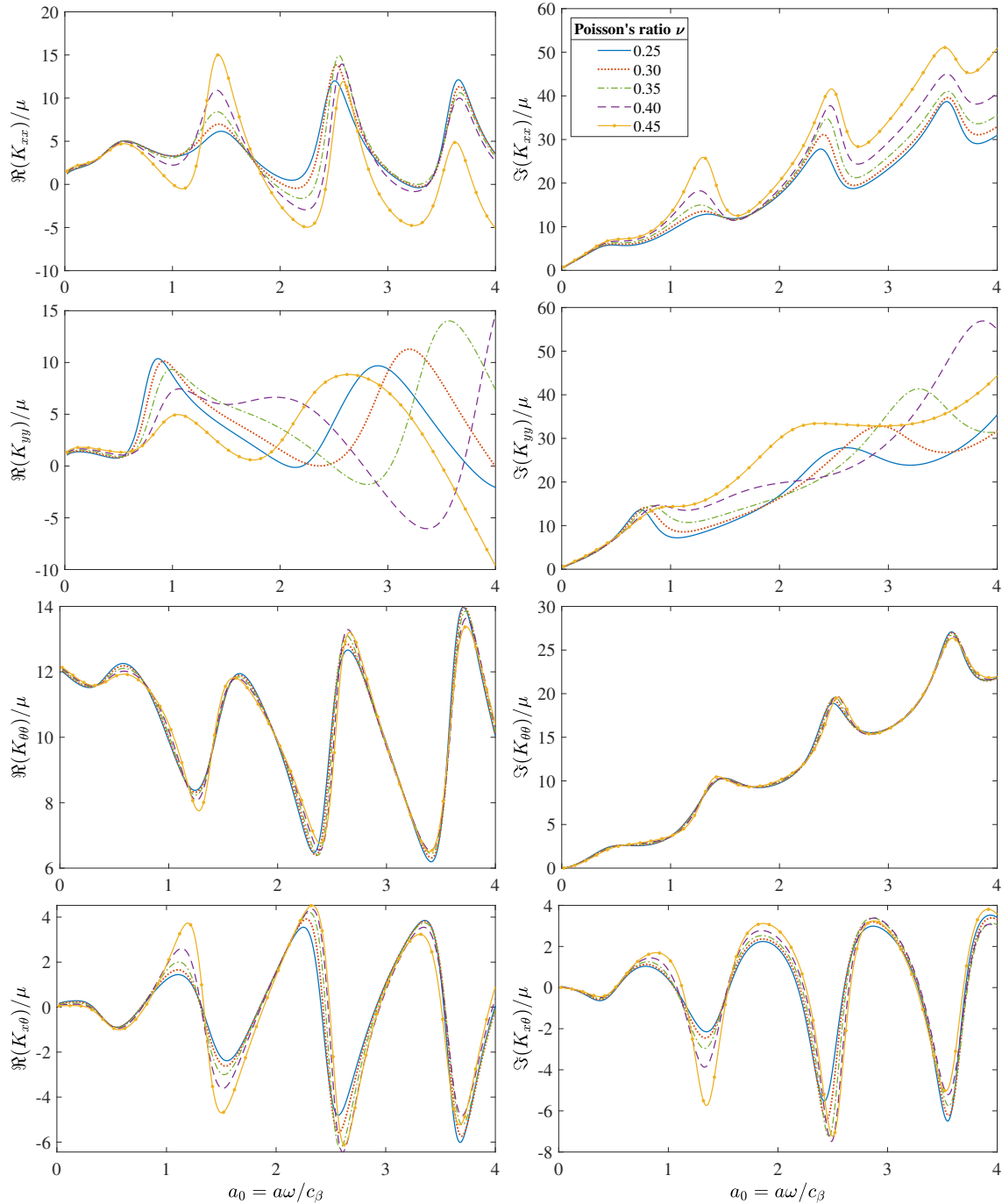
Figure 4.13: The SIFs for $h/a = 4$ and different values of Poisson's ratio.

The SIFs of two-layered domain depend on the burial depth h_1, distance from the cylinder to the soil layers interface h_2, soil Poisson's ratio ν, and material contrast μ_1/μ_2. The effect of h_1 and ν on two-layered domain impedance follows a same mechanism with the homogeneous case and thus is not presented here. We focused on the effect of material contrast ratio μ_1/μ_2 and structure location h_2/a.
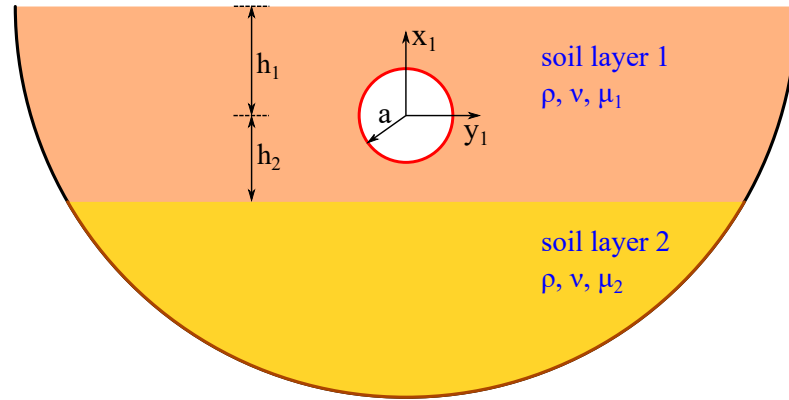
Figure 4.14: Geometry of two-layered half-space.
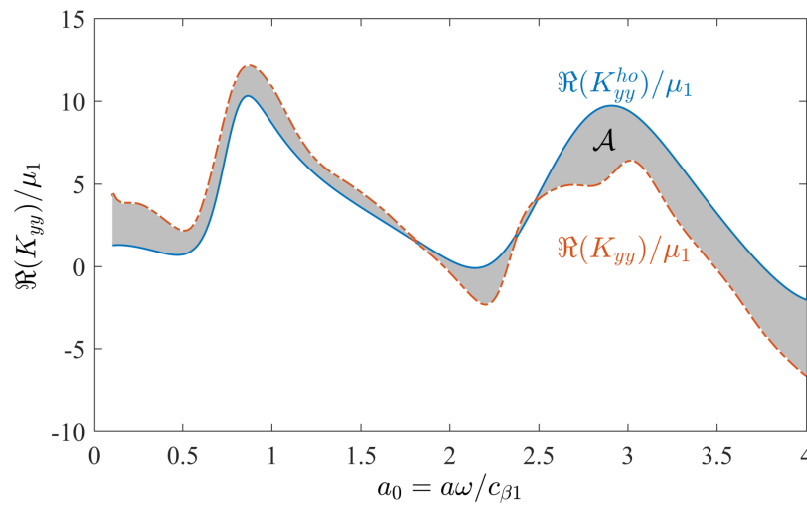
Figure 4.15: Physical illustration of the dimensionless area.

4.7.1 Effect of material contrast

Effect of material contrast was investigated for $h_1/a = 4$ and $h_2/a = 2$. Fig. 4.16 shows the normalized real and imaginary parts of SIFs for the material contrast $\mu_1/\mu_2 = \{0.10, 0.25, 0.50, 0.75, 1.00\}$ as a function of dimensionless frequency $a_0 = a\omega/c_{\beta 1}$, where $c_{\beta 1} = \sqrt{\mu_1/\rho}$ is the shear wave velocity of soil layer 1. In these figures, the analytical results for homogeneous half-space, i.e., $\mu_1/\mu_2 = 1.00$, were also displayed in black dashed-line. The results for homogeneous half-space by FE method agree well with that by analytical solution, once again confirming the accuracy of both approaches.

Overall, both real and imaginary parts of K_{xx}, K_{yy}, $K_{\theta\theta}$, and $K_{x\theta}$ of two-layered domain deviate from that of homogeneous half-space because of the P- and SV-waves reflected from the interface between two soil layers, resulting in the dependence of deviation on the material contrast between these layers. When the soil layer 1, a.k.a the slow medium, is

		$\frac{\mu_1}{\mu_2} = 0.10$	$\frac{\mu_1}{\mu_2} = 0.25$	$\frac{\mu_1}{\mu_2} = 0.50$	$\frac{\mu_1}{\mu_2} = 0.75$	$\frac{\mu_1}{\mu_2} = 1.00$
$h_1/a = 4$	$h_2/a = 2$	11.86	7.92	4.19	1.77	0
	$h_2/a = 4$	7.24	4.53	2.30	0.96	0
	$h_2/a = 8$	4.93	3.11	1.57	0.67	0
	$h_2/a = 16$	3.44	2.18	1.11	0.48	0
$h_1/a = 8$	$h_2/a = 2$	11.70	7.81	4.12	1.75	0
	$h_2/a = 4$	6.98	4.38	2.22	0.94	0
	$h_2/a = 8$	4.76	3.01	1.55	0.64	0
	$h_2/a = 16$	3.41	2.17	1.13	0.49	0

Table 4.1: Dimensionless area $\mathcal{A}$ between $\mathfrak{R}(K_{yy})/\mu_1$ curve of two-layered domain and that of homogeneous half-space.

much softer than soil layer 2, a.k.a the fast medium, the amplitude of the reflection is much larger, meaning that much larger energy is trapped in the soil layer 1 to alter the cylinder response. Accordingly, for all SIF components, the smallest contrast ratio $\mu_1/\mu_2 = 0.10$ generates furthest deviation. When the material contrast ratio μ_1/μ_2 becomes larger, the amplitude of waves reflected from the soil interface is smaller. The SIFs of two-layered domain correspondingly approach and, in case $\mu_1/\mu_2 = 1.00$, coincide with that of homogeneous half-space, as shown in Fig. 4.16. This fact is indicated also by the values of the dimensionless area $\mathcal{A}$ in Table 4.1, which reflect the difference in $\mathfrak{R}\left(K_{yy}\right)$ between a two-layered domain and a homogeneous half-space. For each row of the table, i.e., for each case of $(h_1/a,\ h_2/a)$, the values of $\mathcal{A}$ decrease with increasing ratio μ_1/μ_2 and $\mathcal{A} = 0$ when $\mu_1/\mu_2 = 1.00$.

However, the deviation is not intense, implying that the SIFs are not very sensible to material contrast. Especially when $\mu_1/\mu_2 \geq 0.50$, as indicated in Table 4.1, the SIFs of a two-layered domain are very similar to that of the corresponding homogeneous case, allowing us to use the latter for practical design purposes.

4.7.2 Effect of structure location

To what extent the reflected waves from the half-space free surface and from the soil layers interface impact the SIFs mainly depends on the ratios h_1/a and h_2/a, respectively. The effect of h_1/a on SIFs was investigated in Subsection 4.6.1, hence only the effect of h_2/a on SIFs is analyzed in this section. Fig. 4.17 shows the SIFs for $h_1/a = 4$, $\mu_1/\mu_2 = 0.25$,
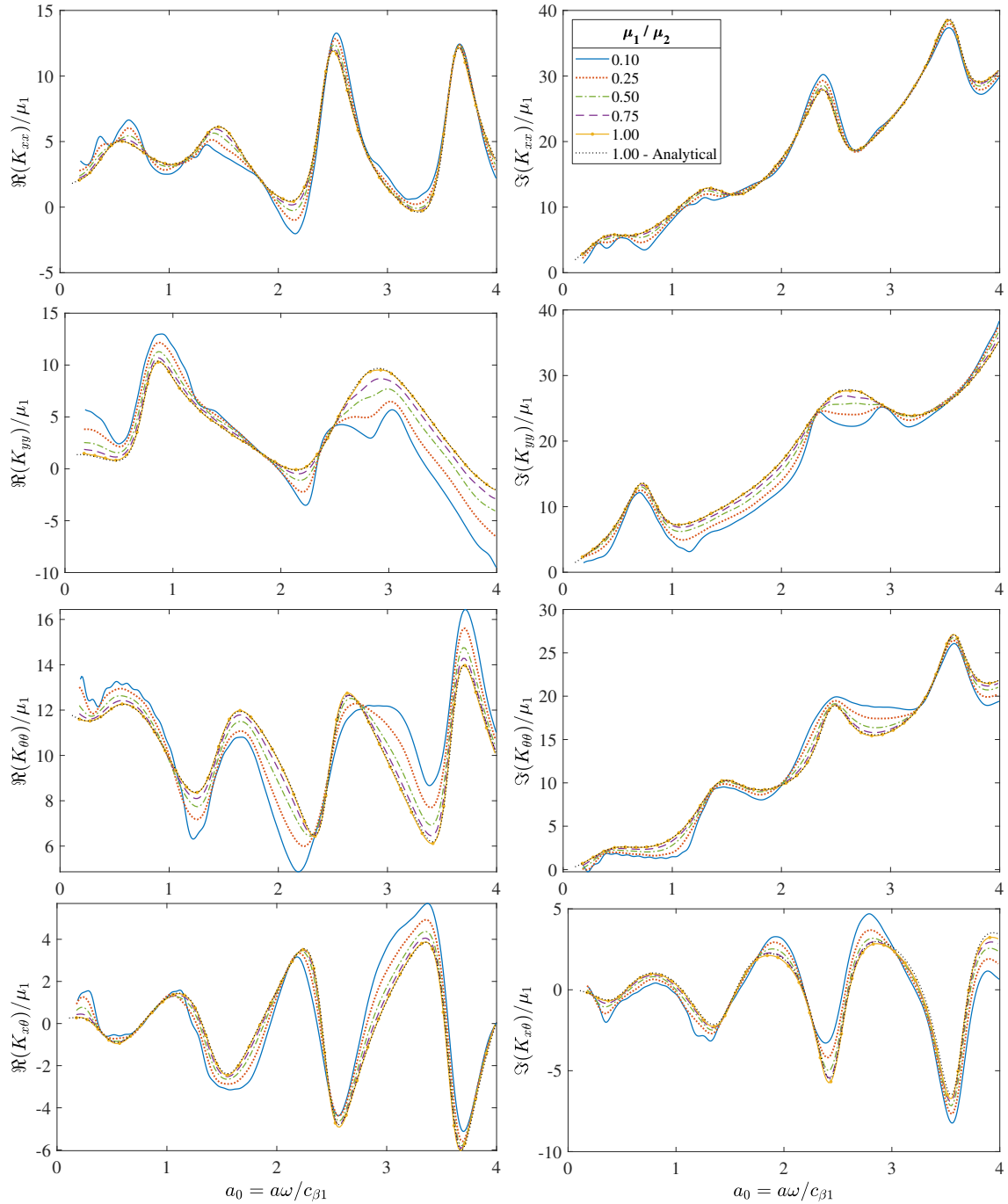
Figure 4.16: SIFs for $h_1/a = 4$ and $h_2/a = 2$ depending on material contrast ratio μ_1/μ_2.

and different cases of $h_2/a = \{2, 4, 8, 16\}$. It also shows the SIFs of the corresponding homogeneous half-space with the same ratio $h_1/a = 4$ for comparison.

Generally, all of SIF components K_{xx}, K_{yy}, $K_{\theta\theta}$, and $K_{x\theta}$, either real or imaginary parts, show a deviation from that of the corresponding homogeneous half-space, as a result of the reflection from the soil layers interface. This deviation is largest for the smallest value of
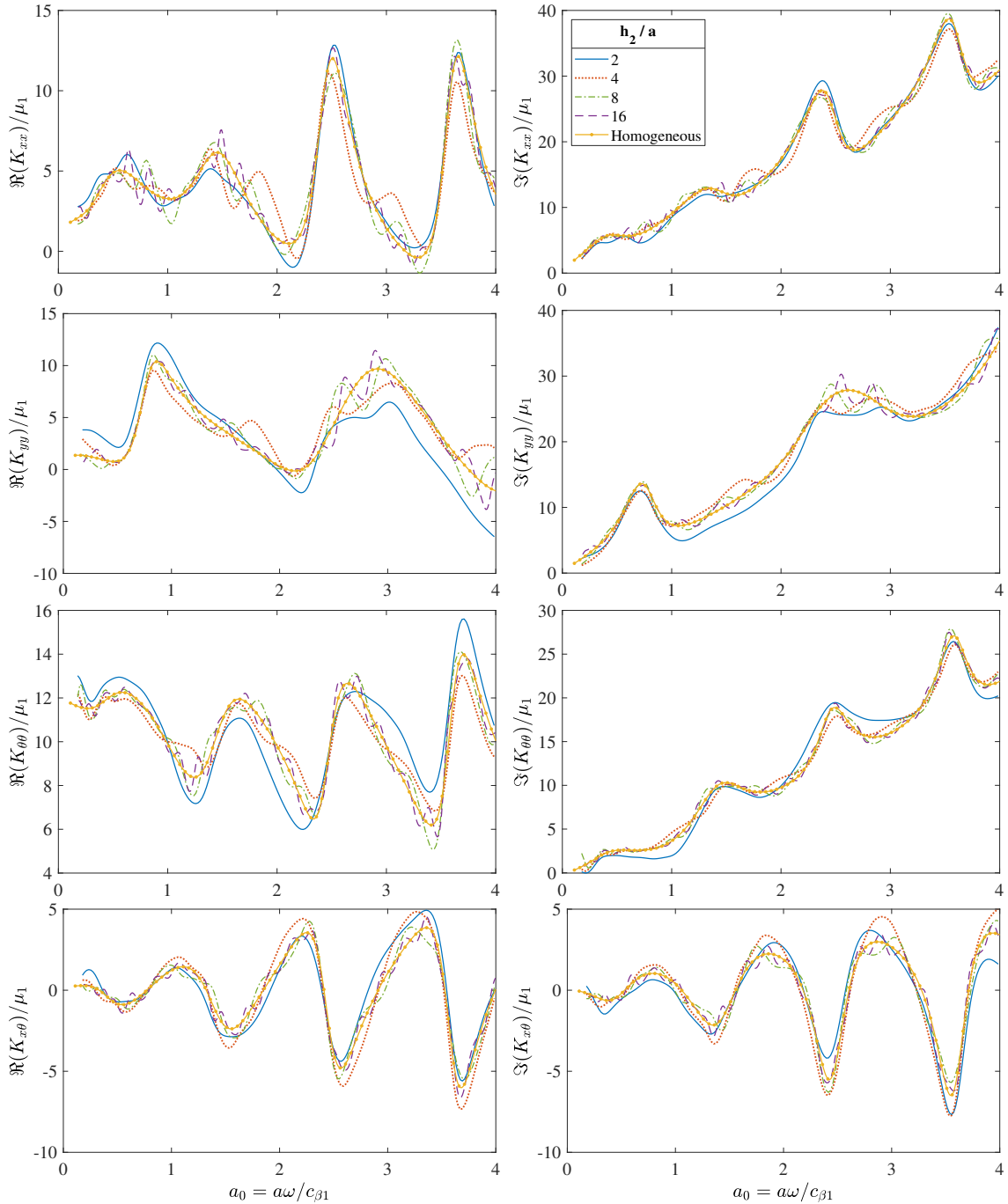
Figure 4.17: SIFs for $h_1/a = 4$ in two-layered domain ($\mu_1/\mu_2 = 0.25$) and homogeneous half-space ($\mu_1/\mu_2 = 1.00$).

h_2/a, because the least energy of the reflected waves is dissipated along the shortest path of propagation from the soil layers interface to the cylinder. When h_2/a is larger, more energy is dissipated when P- and SV- waves travel from the soil interface to the cylinder. Therefore, the impact of soil interface reflection on the cylinder is weaker and the two-layered domain

SIFs are approaching the homogeneous half-space SIFs. The values of dimensionless area $\mathcal{A}$ in Table 4.1 reflect this fact as well. For each column of the table, i.e., for each case of $(h_1/a, \mu_1/\mu_2)$, $\mathcal{A}$ decreases with increasing value of h_2/a, meaning less difference in $\mathfrak{R}\left(K_{yy}\right)$ between a two-layered domain and a homogeneous half-space.

For practical design, the effect of reflected waves from the soil interface can be negligible because the SIFs of a two-layered domain and that of the corresponding homogeneous half-space are very similar, especially when $h_2/a \geq 8$.

4.8 Conclusions

This chapter provides a closed-form solution for the dynamic in-plane SIFs of an infinitely long rigid circular structure buried in linear elastic half-space. The derived analytical result provides practitioners with high-fidelity values of spring stiffness and dashpot damping coefficient that can be used in seismic design of spatially distributed underground structures. The solution assumed both a homogeneous elastic half-space, and a harmonic displacement at the structure boundary with traction-free boundary condition at the free surface. In such a solution, the displacement potentials were expressed as Hankel– and Bessel–Fourier series expansion and the contour integrals on the physical Riemann sheet were numerically evaluated by nested Gauss–Kronrod quadrature rule and Cauchy's residue theorem. In addition, we used FE analyses in time domain and the FT technique to compute the dynamic compliance matrices, which were subsequently inverted to obtain dynamic SIFs of the rigid cylinder in homogeneous and two-layered linear elastic half-spaces. Parametric studies were performed to examine the effect of geometric and mechanical factors on that dynamic SIFs. In summary, our study showed/confirmed that

1. A number of $N = 8$ modes in the Hankel– and Bessel–Fourier series are sufficient to accurately approximate the SIFs of a buried structure in homogeneous half-space. Moreover, we showed that L^2-norm of the error due to the series truncation decays rapidly with increasing N, approximately $O(10^{2-N})$.

2. For homogeneous elastic half-space, results obtained by analytical and numerical approaches showed a complete agreement with each other. As expected, when the burial depth h/a is very large, the half-space SIFs converge to the solution of *Novak et al.* (1978) for full-space SIFs.

3. Overall, all the SIF components K_{xx}, K_{yy}, $K_{\theta\theta}$, and $K_{x\theta}$ depend on the excitation frequency, the shear modulus and Poisson's ratio of soil domain, the burial depth, and

the structure dimension. In a layered soil domain, they depend also on the material contrast and the distance from the structure to the interface between soil layers.

4. Because of the asymmetric geometry, there is coupling behavior between translational motion along x-axis and torsional motion about the cylinder centroid, indicated by non-zero values of $K_{x\theta} = K_{\theta x}$. The coupling impedance is generally much smaller than translational and torsional impedance. Also, the coupling impedance is small in low-frequency regime, e.g., $a_0 < 0.5$, while being considerable in higher frequency regime. When $h/a \to \infty$, the geometry becomes symmetric, and thus $K_{x\theta} = K_{\theta x} \to 0$, similar to the full-space problems.

5. All the SIF components of homogeneous half-space oscillate about their counterparts of homogeneous full-space, because of the constructive and destructive effects of wave interference in the region between cylinder location and free surface. With increasing burial depth h/a, the oscillation amplitude gradually decreases while the oscillation frequency gradually increases. The translational impedance K_{xx} and K_{yy} are more sensitive to the variation of burial depth than the torsional impedance $K_{\theta\theta}$. Besides, for K_{xx}, K_{yy}, and $K_{\theta\theta}$, the effect of burial depth variation on the real part (spring stiffness) is stronger than that on the imaginary part (dashpot damping coefficient).

6. The translational impedance K_{xx} and K_{yy} depend significantly on Poisson's ratio of the soil domain, while the torsional impedance $K_{\theta\theta}$ almost does not. Moreover, in low-frequency regions, e.g., $a_0 < 0.5$, variation in Poisson's ratio does not have any noticeable effect on all SIF components.

7. In two-layered half-space, all SIF components K_{xx}, K_{yy}, $K_{\theta\theta}$, and $K_{x\theta}$ deviate from that of the corresponding homogeneous half-space because of the reflected P- and SV-waves from the soil layers interface. This deviation depends on the material contrast ratio μ_1/μ_2, in which the smallest ratio yields furthest deviation because the energy entrapment in the top soil layer is largest.

8. In two-layered half-space, the distance h_2 from cylinder centroid to soil layers interface affects SIFs in a similar manner that the burial depth h_1 does, because both h_1 and h_2 are linked to the energy dissipation along propagation path and the phase difference between vibrating sources.

9. If $\mu_1/\mu_2 \geq 0.50$ or $h_2/a \geq 8$, the SIFs of a two-layered half-space can be approximately replaced with that of the corresponding homogeneous half-space for practical design purpose.

Despite some limitations, namely the applicability for rigid (or nearly rigid) circular structures and for elastic domains with small displacements, this study is an important step toward building a reduced-order model to investigate SbSI problems. Our work provides useful information about initial in-plane spring stiffness and dashpot damping coefficient, which we envision integrating in large-scale SbSI models, e.g., reduced-order model to study soil-pipeline interaction presented in *Nguyen and Asimaki* (2018, 2020); *Asimaki et al.* (2019).

C h a p t e r   5

Application: Reduced-order modeling of buried pipe subjected to the propagation of Rayleigh surface wave

Contents of this chapter

5.1   Introduction

Spatial variation of earthquake ground motion (SVEGM) is interpreted as the differences in seismic ground motion, e.g., amplitude, frequency, and phase, measured at different locations along the structure dimensions. This variation is mainly attributed to: (1) wave passage effect in which the seismic wave arrives at different times at different recording stations because of the finite wave velocity, (2) incoherence effect caused by the extended source and the inhomogeneities along the propagation path, and (3) local site effect which is the differences in local soil conditions at each stations. Given the spatial extent of the buried pipeline networks, it is very important to consider the SVEGM in seismic design of such structures to safeguard the structural integrity.

This chapter presents an application of the SIFs derived in Chapters 3 and 4 to build a reduced-order model to analyze the SPI problems. Fig. 5.1 illustrates the configuration of the problem, in which a straight pipe is subjected to the propagation of Rayleigh surface wave. The buried pipe and two soil domains are assumed to be linear elastic materials.

Two cases of SVEGM are investigated: (1) wave propagation time delay when the pipe is buried in a homogeneous half-space and (2) wave propagation time delay and local site effect when the pipe is buried in a heterogeneous half-space, e.g., an ellipse basin.
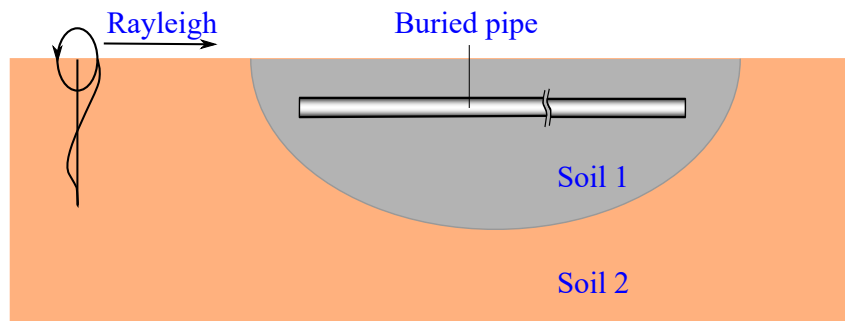
Figure 5.1: Schematic geometry of a buried pipe subjected to the Rayleigh surface wave.

5.2   Models for soil-pipe interaction analysis

5.2.1   Model neglecting soil-pipe interaction

Pipe is assumed to be much softer than soil and cannot provide any resistance to ground motions. Hence, the pipe perfectly conforms to free-field ground motions, which are the soil displacements induced by the propagation of seismic waves in the absence of excavation and structures. The free-field ground motions can be computed by either analytical solutions or numerical simulations.

5.2.1.1 Rayleigh surface wave in a homogeneous half-space by analytical expression

Let ω is the angular frequency, c_α, c_β, and c_R are the phase velocities of compressional, shear, and Rayleigh waves, respectively. $k_\alpha = \omega/c_\alpha$, $k_\beta = \omega/c_\beta$, and $k_R = \omega/c_R$ are the corresponding wavenumbers. The displacements along x and y axes of Rayleigh surface wave, denoted as u_x and u_y, are expressed as (*Viktorov*, 1967)

$$u_x = A k_R \left(e^{q_R y} - \frac{2 q_R s_R}{k_R^2 + s_R^2} e^{s_R y} \right) \sin \left(k_R x - \omega t \right) , \tag{5.1}$$

$$u_y = -A q_R \left(e^{q_R y} - \frac{2 k_R^2}{k_R^2 + s_R^2} e^{s_R y} \right) \cos \left(k_R x - \omega t \right) , \tag{5.2}$$

where A is an arbitrary constant, $q_R = \sqrt{k_R^2 - k_\alpha^2}$, $s_R = \sqrt{k_R^2 - k_\beta^2}$, and t is time.

5.2.1.2 Rayleigh surface wave in a heterogeneous half-space by finite element simulation

For basin configuration, the harmonic Rayleigh surface wave propagates from left to right, originates from stiff soil (soil 2) and reaches softer soil (soil 1). The reflection at the basin circumference and the wave interference inside the basin make the problem become more complex. The free-field ground motions inside the basin can be computed by FE analyses.
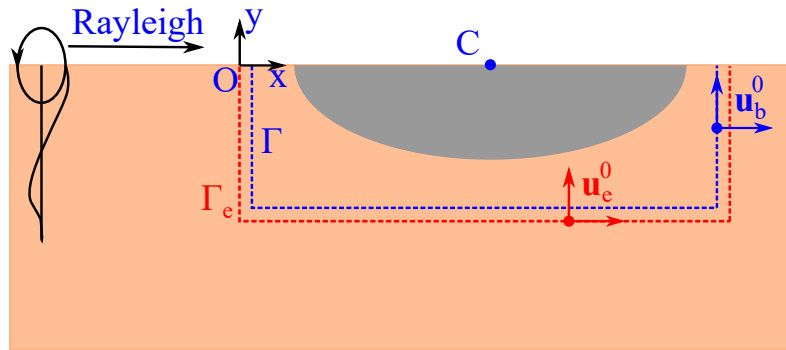
Figure 5.2: Geometry of the truncated domain with boundaries Γ and Γ_e.

In FE analyses, the effective input forces are defined as equivalent input forces which are applied to generate a predetermined displacement field. We used the domain reduction method proposed by *Bielak et al.* (2003) to compute the effective input forces of the predetermined Rayleigh surface wave displacement field of soil 2. The configuration of the truncated domain is shown in Fig. 5.2. The effective input forces P_b^{eff} and P_e^{eff} applied on

the boundaries Γ and Γ_e at each time step are governed by

$$P_b^{\text{eff}} = -M_{\text{be}}\ddot{u}_e^0 - K_{\text{be}}u_e^0,$$ (5.3)

$$P_e^{\text{eff}} = M_{\text{eb}}\ddot{u}_b^0 + K_{\text{eb}}u_b^0,$$ (5.4)

where M_{be} and M_{eb} are the off-diagonal quadrants of the mass matrices assembled from the single layer of finite elements between two boundaries Γ and Γ_e, and K_{be} and K_{eb} are the off-diagonal quadrants of the corresponding stiffness matrices. For lumped mass, M_{be} and M_{eb} would be zero. u_b^0 and u_e^0 are the predetermined displacement vector of nodes on Γ and Γ_e, respectively.

The Fourier transform of an unwindowed sinusoidal function with frequency ω is non-zero only at $\pm\omega$. However, for the FE analyses, we consider the signal only within a finite interval of time while implying zero values outside that time interval, which is equivalent to multiplying the waveform with a rectangular function, leading to the spectral leakage phenomenon. It is therefore necessary to use a windowing technique to distribute the leakage spectrally, allowing interesting features of the signal to be observed. Moreover, the tapering property of the window function prevents numerical artifact induced by a sudden application of non-zero value of signal at the beginning of the FE analyses. The N-point Tukey (a.k.a tapered cosine) window technique is used in this study, defined by

$$w(t) = \begin{cases} \dfrac{1}{2}\left\{1 + \cos\left[\dfrac{2\pi}{\alpha}(t - \alpha/2)\right]\right\}, & \text{for } 0 \le t < \dfrac{\alpha}{2} \\ 1, & \text{for } \dfrac{\alpha}{2} \le t < 1 - \dfrac{\alpha}{2} \\ \dfrac{1}{2}\left\{1 + \cos\left[\dfrac{2\pi}{\alpha}(t - 1 + \alpha/2)\right]\right\}, & \text{for } 1 - \dfrac{\alpha}{2} \le t < 1 \end{cases}$$ (5.5)

where t is an N-point linearly spaced time vector. The parameter α is the ratio of cosine-tapered section length to the entire window length, henceforth taken as $\alpha = 0.5$.
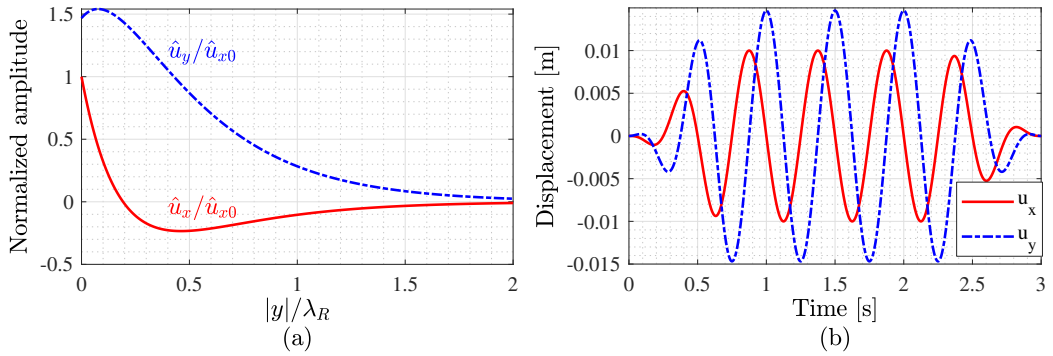
Figure 5.3: Displacements of Rayleigh waves as a function of: (a) depth; and (b) time.

The pattern of the Rayleigh wave displacements is illustrated in Fig. 5.3(a). The displacement amplitudes $\hat{u}_x$ and $\hat{u}_y$, normalized with $\hat{u}_{x0}$, are plotted as a function of dimensionless depth $|y|/\lambda_R$, where $\hat{u}_{x0}$ is the amplitude of x-displacement at the ground surface $y = 0$ and $\lambda_R = 2\pi c_R/\omega$ is the wavelength of Rayleigh wave. Fig. 5.3(b) shows time histories of the displacement components at the point $(x, y) = (0, 0)$, which are the multiplication of harmonic Rayleigh wave in Eqs. (5.1), (5.2) and Tukey window in Eq (5.5).

The x- and y-components of the vectors $\boldsymbol{u}_b^0$ and $\boldsymbol{u}_e^0$ are predetermined with Eqs. (5.1), (5.2), and (5.5). We consider the Rayleigh wave propagates along the positive x-axis, starting at point $O(0, 0)$. Because of the finite wave velocity, u_x and u_y at a point are zero when the waves have not reached that point yet, i.e., when $t < k_R x/\omega$.

We wrote a subroutine incorporated into LS-DYNA solver to generate the Rayleigh surface wave propagation. The fidelity of this subroutine was verified for a case of Rayleigh wave propagating through a homogeneous elastic half-space soil domain, where analytical solution is available via Eqs. (5.1), (5.2), and (5.5). The input parameters for the verification problem are as follows: $\omega = 2\pi$ rad/s; the Poisson's ratio, mass density, and shear modulus of soil domain are $\nu = 0.25$, $\rho = 1800$ kg/m^3, and $\mu = 4.5$ MPa, respectively; and the scalar A in Eqs. (5.1) and (5.2) is $A = 0.5193$. For FE analysis, the number of elements per wavelength is chosen as $n_{epw} = 50$, while the time step size is based on the Courant–Friedrichs–Lewy condition.
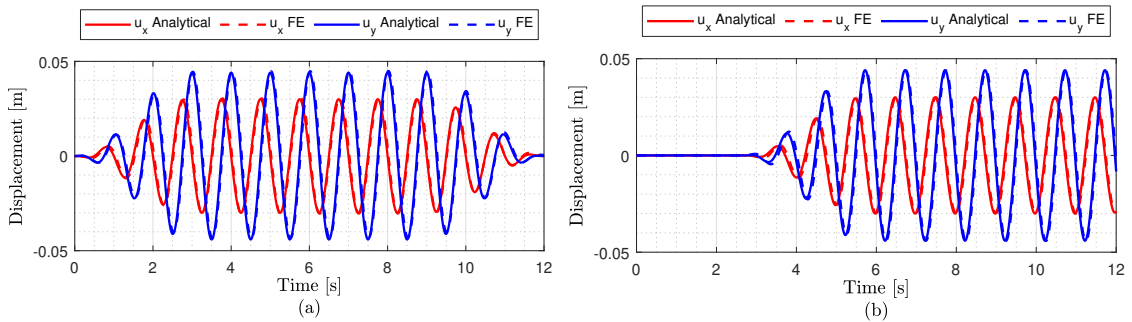
Figure 5.4: u_x and u_y computed by analytical solution and by FE approach with incorporated subroutine: (a) at point $O(0, 0)$; and (b) at point $C(125, 0)$.

Fig. 5.4 shows the displacements at two points O and C, computed by analytical solution via Eqs. (5.1), (5.2), and (5.5), and by FE approach with incorporated subroutine. The results by these two approaches agree well with each other. Meanwhile, Fig. 5.5 illustrates the displacement field contours of Rayleigh surface wave propagation at time $t = 7.25$ second. Observably, for both u_x and u_y, the wave envelopes travel from left to right without
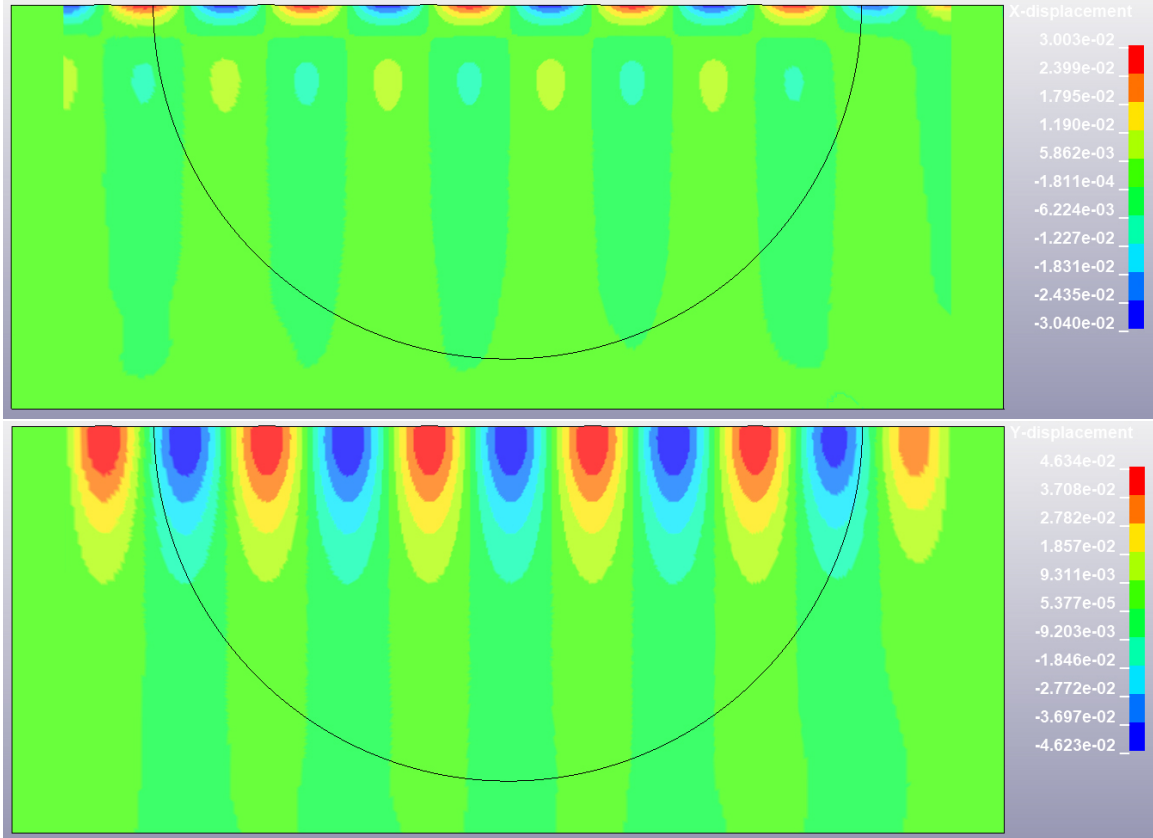
Figure 5.5: u_x and u_y displacement fields at $t = 7.25$ s.

dispersion, which is expected for fundamental mode of Rayleigh wave in homogeneous elastic half-space soil medium.

5.2.2 Model considering soil-pipe interaction with free-field input

The reduced-order model for SPI analysis is shown in Fig. 5.6, in which the pipe is modeled as beam elements[1] and the surrounding soil is replaced by a set of springs and dashpots formulated to represent its macroscopic reaction to differential deformations between soil and pipe.

The spring stiffness and dashpot coefficient per unit length along x-axis, k_x and c_x, and along y-axis, k_y and c_y, are computed as

$$k_{\mathrm{j}} = \mathfrak{R}\left(K_{\mathrm{jj}}\right), \tag{5.6}$$

$$c_{\mathrm{j}} = \mathfrak{I}\left(K_{\mathrm{jj}}\right)/\omega, \tag{5.7}$$

---

[1]In the context of this chapter, a beam element refers to a beam-column element that resists both axial force and bending moment. Each node of the beam has one rotational and two translational degrees of freedom.
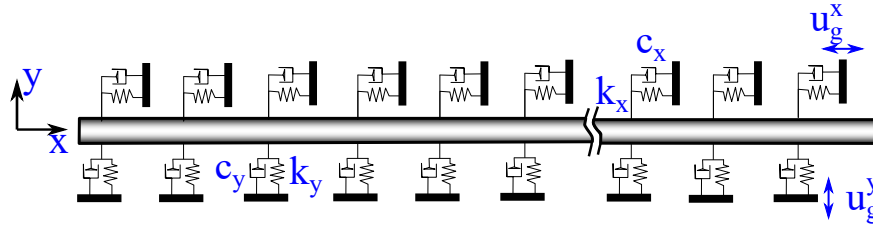
Figure 5.6: Schematic of pipe analysis.

where j = x or y, $\mathfrak{R}$ and $\mathfrak{I}$ represent the real and imaginary parts. The SIFs along axial and vertical directions, K_{xx} and K_{yy}, were computed previously in Chapters 3 and 4 as a function of excitation frequency ω, shear modulus and Poisson's ratio of soil domain, burial depth and radius of the buried pipe.

The free-field ground motions u_g^x and u_g^y, obtained in the same way as in Subsection 5.2.1, are applied at the ends of springs and dashpots as seismic excitation. The analysis was performed using OPENSEES framework.

5.2.3 Models based on substructure and finite element methods

5.2.3.1 Review of substructure method for soil-structure interaction analysis in case of building structures
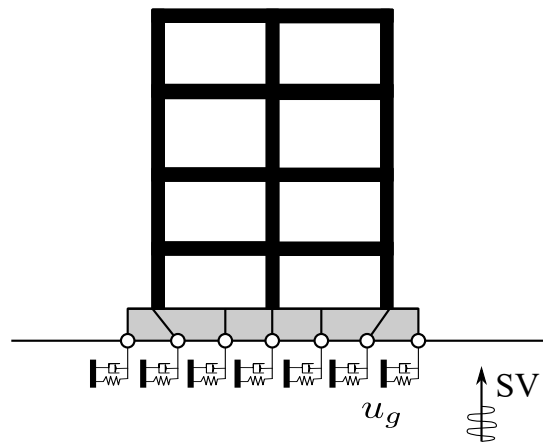
Figure 5.7: Building structure resting on spring-dashpot systems.

Until the early 1970s, many of soil-structure interaction models were restricted to systems with foundation resting on the surface of a homogeneous half-space and the seismic ground motions being invariant in horizontal planes, e.g., the ground motions of vertically propagating SV waves. As shown in Fig. 5.7, to analyze the structures, the continuum domain of soil was replaced with spring-dashpot systems which were subsequently excited with

free-field ground motions. The assumption of free-field input motions in this configuration was sufficient and rigorous (*Kausel*, 2010). However, for structures with embedded foundations, considerable disparities were observed between the results of the classical method with free-field input motions and those of direct numerical simulations, such as finite elements.
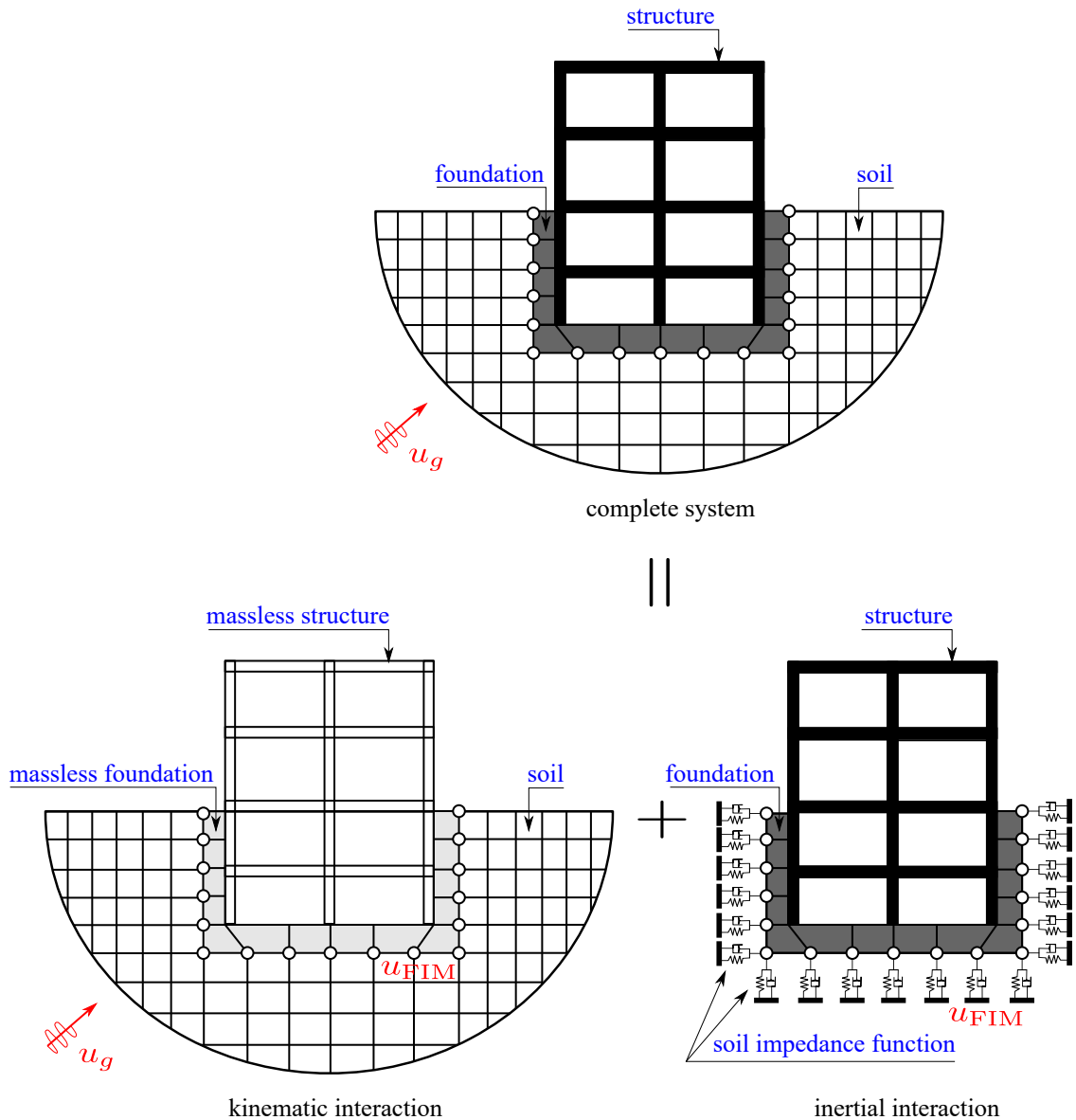
Figure 5.8: Schematic of substructure method.

To accomplish fully consistent comparisons between those two methods, *Kausel et al.* (1978) proposed a three-step solution based on superposition theorem. It is referred to as substructure method in the guidelines of U.S. National Institute of Standards and Technology

(*NIST*, 2012). Fig. 5.8 shows the schematic of substructure method, which includes three main steps:

1. Computing the foundation input motion (FIM), which is the motion of foundation that accounts for the stiffness and geometry of the foundation. Notice that the FIM is obtained by solving the problem of massless structure and massless foundation subjected to the same seismic excitation as the direct model. This FIM generally differs from the free-field motion, representing the effects of kinematic interaction.

2. Computing the SIF.

3. Computing the response of real structure and foundation, supported on the frequency-dependent springs and dashpots (SIF), and subjected to the FIM at the base of spring-dashpot systems.

It might appear that the substructure method has no advantage in the computational cost compared with the direct FE simulation, because the former generally requires FE analyses for the determination of FIM and SIF. However, the FIM can be obtained by transfer functions available in the literature for various foundation configurations considering kinematic interaction effects. Meanwhile, the corresponding SIF is available in the literature as well. Those predetermined values of FIM and SIF significantly reduce the computational time because we need to deal with only the system of structure and foundation, instead of the whole soil-structure-foundation system. This enables the practitioners to conduct extensive studies to account for the uncertainties in seismic design of the infrastructures.

5.2.3.2 Soil-pipe interaction model based on substructure method

The soil and pipe are true 3D elements. A 3D FE model can analyze the axial, bending, and hoop stresses of pipe or the local buckling and ovalization of pipe cross sections, or account for the 3D seismic excitation. However, in case of in-plane excitation and only axial and bending demands of pipe are desired, researchers and practitioners commonly resort to a 2D FE model in which the pipe is modeled by beam elements.

Fig. 5.9 shows the configuration of 2D FE model in direct method for analyzing SPI problem using LS-DYNA R10.0.0 solver. The effective input forces P_b^{eff} and P_e^{eff}, obtained in the same way as in Subsection 5.2.1, were applied on Γ and Γ_e at each time step via the incorporated subroutine. The pipe was modeled as beam elements with the soil-pipe interface being fully bonded. The outside domain Ω^+ is the residual displacement field, which is the relative displacement with respect to the reference free-field displacement. This residual

displacement is usually small and is absorbed by the Lysmer–Kuhlemeyer dashpots (*Lysmer and Kuhlemeyer*, 1969) placed at the outside boundary, preventing fictitious reflection waves from propagating back to the truncated domain.
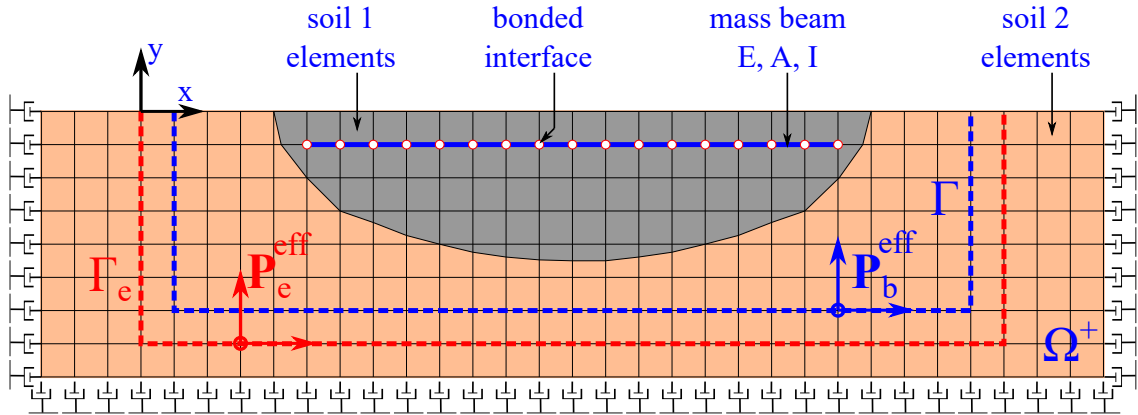
Figure 5.9: Schematic of direct method for SPI problem.
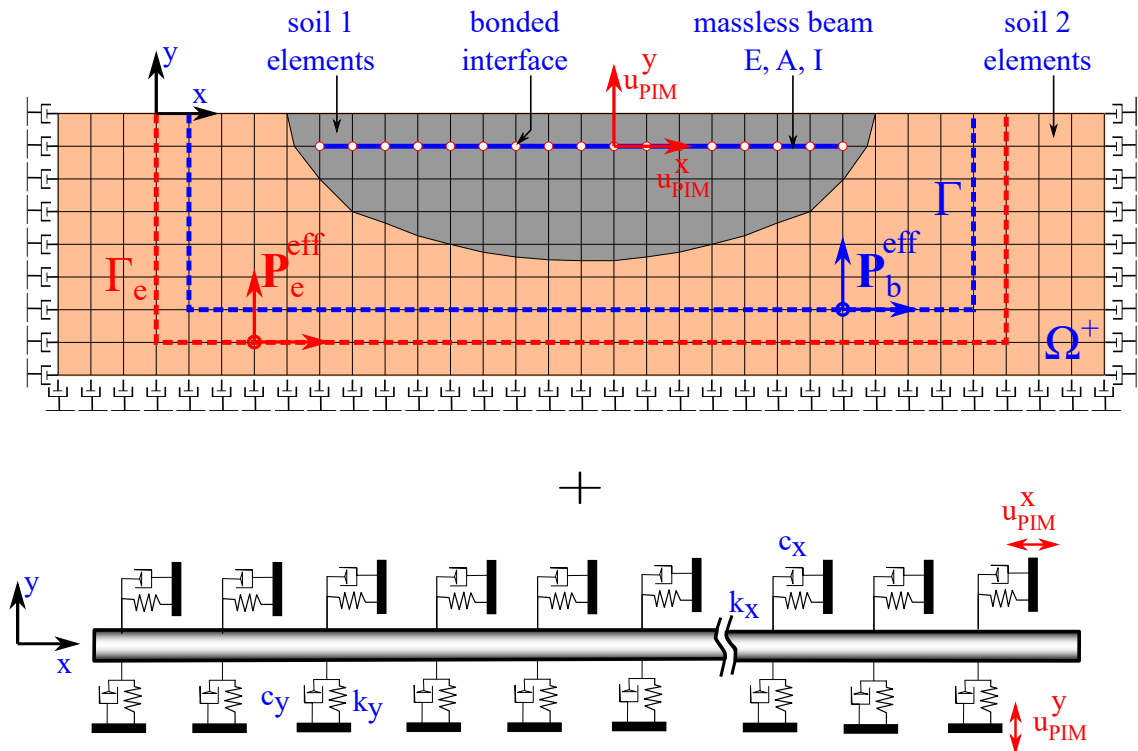
Figure 5.10: Schematic of substructure method for SPI problem.

The reduced-order model based on substructure approach for the SPI analysis is shown in Fig. 5.10. The pipe input motion (PIM) is the motion at the pipe nodes that accounts for

the stiffness and geometry of the pipe structure. Such motion applies for the condition of pipe structure having no mass, and generally differs from the free-field motion. This type of motion is identical with the FIM in substructure method, representing the effects of kinematic interaction. The FE model to compute PIM is identical with that in direct method, except that the pipe has no mass. The time histories of x- and y-components of the PIM, denoted as u_{PIM}^x and u_{PIM}^y, were recorded at each pipe node. The PIMs were subsequently applied at the bases of spring-dashpot systems as seismic excitation and the pipe analysis was performed using OPENSEES framework.

The spring stiffness and dashpot coefficient are computed from the SIF. It should be noticed that the SIFs obtained in Chapters 3 and 4 are for the vertical plane perpendicular to the pipe axis and therefore are consistent with the 3D FE model of soil-pipe system. For the 2D FE model of the direct model presented here, the SIF should be calculated for the vertical plane consisting of the pipe axis, i.e., the xy-plane, thereby making the results of substructure and direct models consistent. However, we can use the SIF obtained in Chapters 3 and 4 as an approximation, which eventually yields satisfactory results as shown later in Section 5.3.

5.3   Results and comparisons

The geometry of the 2D problem analyzed is shown in Fig. 5.11. We considered an ellipse basin with major radius r_1 and minor radius r_2. Soil 1 and soil 2 media have the same values of mass density ρ and Poisson's ratio ν, but different values of shear modulus, μ_1 compared with μ_2. The radius, thickness, length, and burial depth of the pipe are a, t, L, and h, respectively. Three control points CP_1, CP_2, and CP_3 for verification purpose were chosen as depicted.
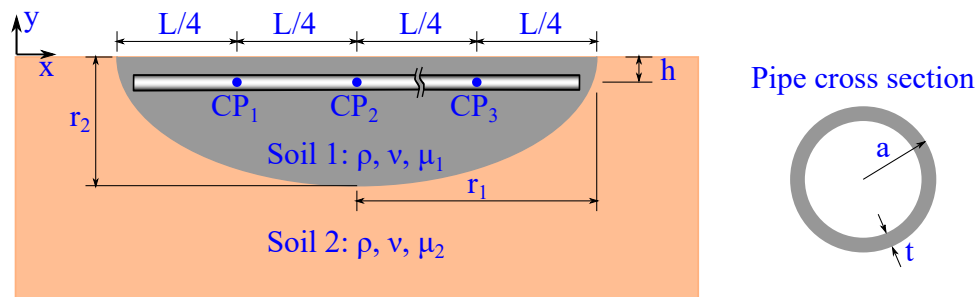
Figure 5.11: Geometry of the problem analyzed.

We conducted the investigation by: a model neglecting SPI (M1), a reduced-order model considering SPI with free-field input (M2), a reduced-order model considering SPI with PIM based on substructure method (M3), and a direct model using 2D FE analyses (M4).

Category	Parameter	Case 1	Case 2	Unit
Basin shape	r_1	100	100	[m]
	r_2	50	50	[m]
Rayleigh wave	f_c	1	1	[Hz]
	A	0.1731	0.1731	-
Soil media	ρ	1800	1800	[kg/m^3]
	ν	0.25	0.25	-
	μ_1	4.5	1.125	[MPa]
	μ_2	4.5	4.5	[MPa]
Pipe	a	0.5	0.5	[m]
	t	0.025	0.025	[m]
	h	2	2	[m]
	L	199.84	199.84	[m]
	ρ_s	7850	7850	[kg/m^3]
	ν_s	0.3	0.3	-
	E_s	200	200	[GPa]
Springs and dashpots	k_x/μ_1	1.10	1.20	-
	$c_x\omega/\mu_1$	0.06	1.35	-
	k_y/μ_1	1.37	1.37	-
	$c_y\omega/\mu_1$	0.90	1.50	-

Table 5.1: Input parameters for case 1 (homogeneous medium) and case 2 (heterogeneous medium).

Two cases were considered: pipe buried in a homogeneous soil medium with $\mu_1/\mu_2 = 1.00$ (case 1), and pipe buried in an heterogeneous soil medium with $\mu_1/\mu_2 = 0.25$ (case 2). The input parameters for two cases are presented in Table 5.1. The scalar A in Eqs. (5.1) and (5.2) was chosen so that the amplitude of u_x of free-field Rayleigh wave at point $O(0,0)$ is 0.01 m. Moreover, in case of heterogeneous medium, the vertical distance between pipe centroid and the soil layer interface (h_2 distance in Subsections 3.7.2 and 4.7.2) is very large compared with the pipe radius a, enabling us to use the SIFs of the corresponding homogeneous as an approximation. Therefore, for both case 1 and case 2, we used information from Figs. 3.13

and 4.12, with $h/a = 4$, to find the values of k_x, c_x, k_y, and c_y. Note that these are values per unit length of pipe.
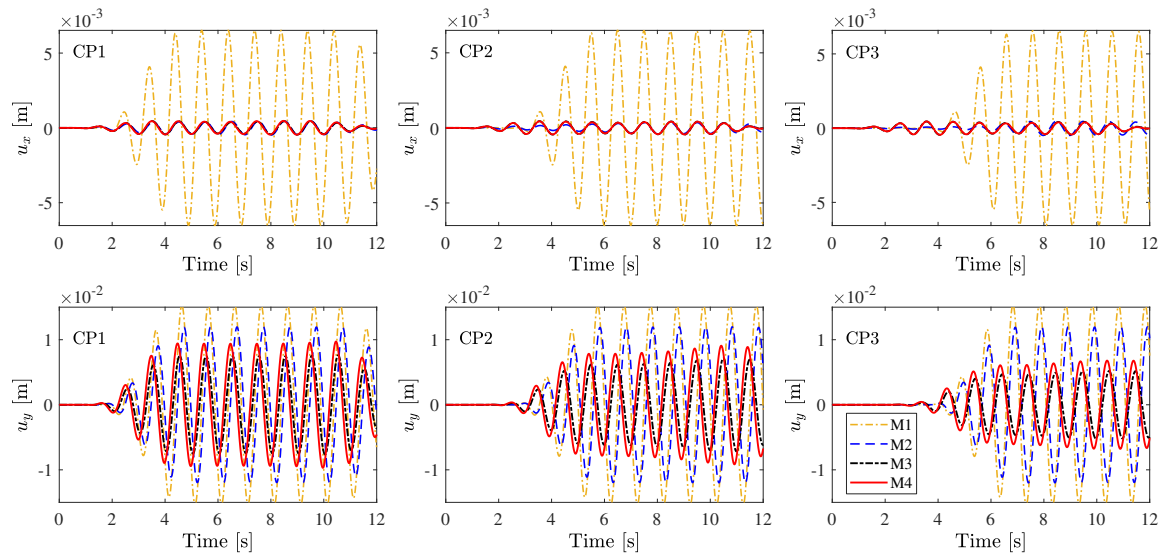
Figure 5.12: Displacements at CP_1, CP_2, and CP_3 in case of homogeneous half-space.
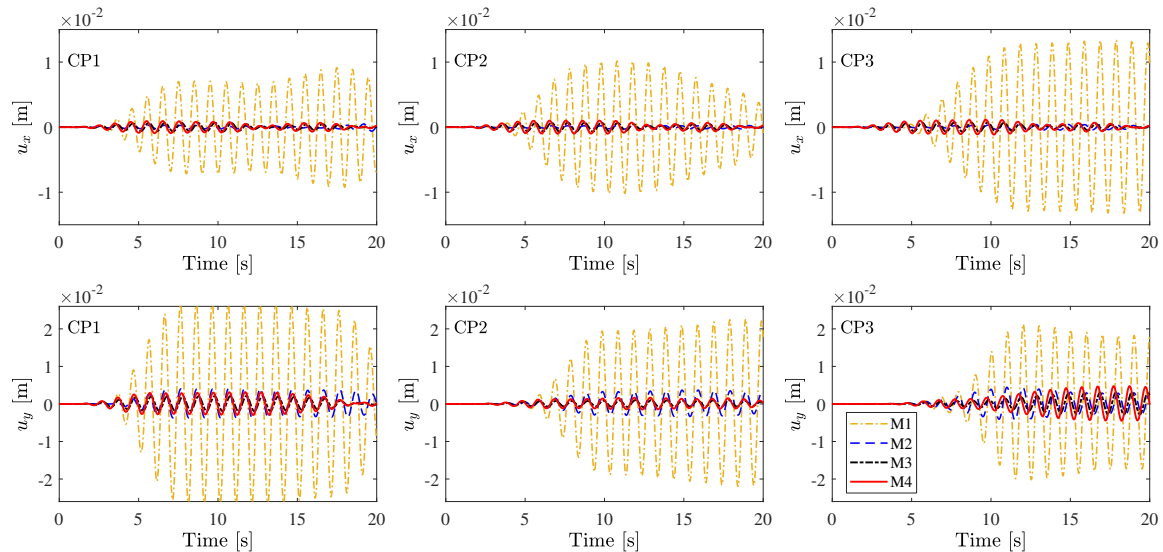
Figure 5.13: Displacements at CP_1, CP_2, and CP_3 in case of heterogeneous half-space.

The x- and y-displacement components at three control points achieved through four models are plotted in Fig. 5.12 for case 1 and in Fig. 5.13 for case 2. Generally, model M1 yields much larger results compared with those by M2, M3, and M4, which is as expected because M1 does not account for the resistance coming from pipe stiffness while models M2, M3, and M4 consider the effect of SPI.
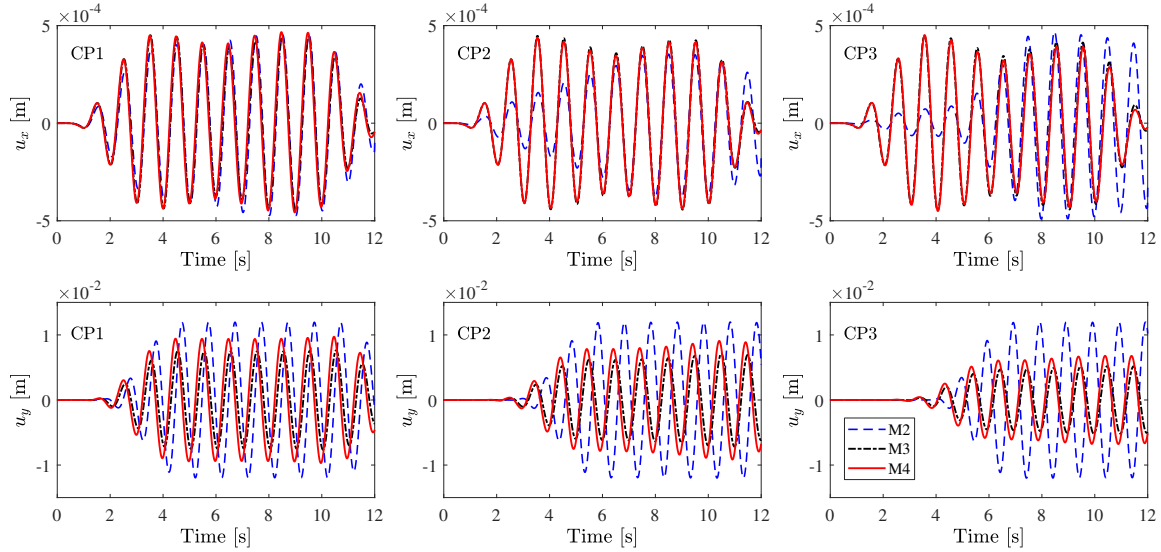
Figure 5.14: Displacements at CP$_1$, CP$_2$, and CP$_3$ by M2, M3, and M4 for homogeneous half-space.
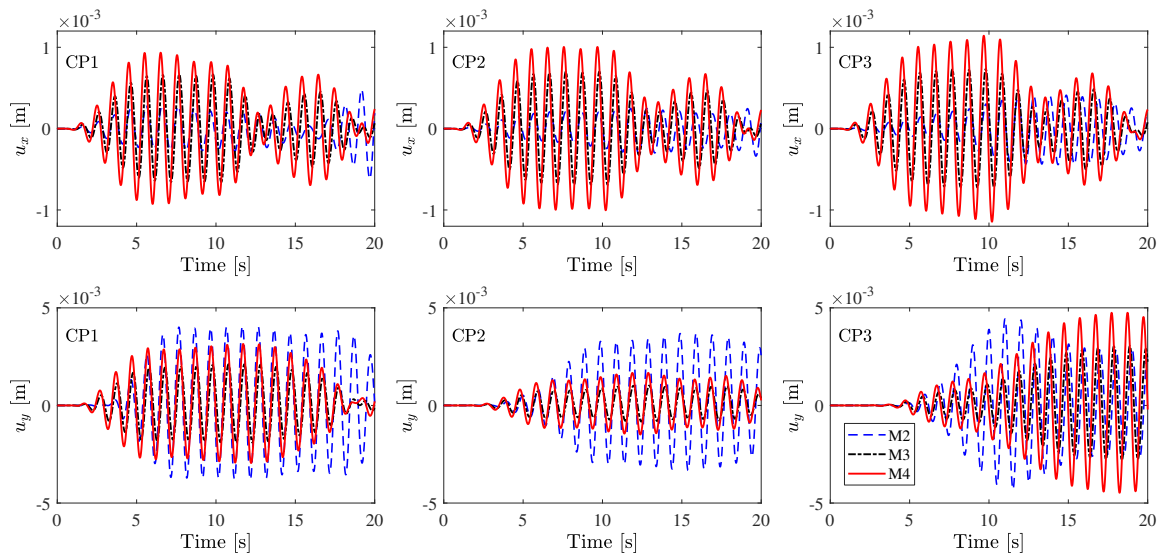
Figure 5.15: Displacements at CP$_1$, CP$_2$, and CP$_3$ by M2, M3, and M4 for heterogeneous half-space.

To compare the results by M2, M3, and M4, we plot only the displacement histories at control points computed by those three models. Fig. 5.14 shows the results for the homogeneous half-space, while Fig. 5.15 displays those for the heterogeneous half-space. Overall, the results computed by M2, M3, and M4 are of the same order of magnitude, for both homogeneous and heterogeneous half-spaces. Moreover, compared with the results by M2, displacement time histories obtained by M3 and M4 are more consistent with each other. This is not particularly surprising because the models M3 and M4 are mathematically

equivalent, given that the PIM and SIF are accurately determined. The differences in the patterns of displacement histories between M2 and M3 represent the effect of kinematic interaction, in which the existence of massless pipe beam alters the free-field ground motions.

However, there are still some differences in the amplitude of displacement between models M3 and M4, especially in case of the heterogeneous half-space. This is partially because of the SIF approximation mentioned in Subsection 5.2.3. The assumption of rigid (or nearly rigid) pipe cross section used to solve for the SIFs is also a source of error.

Despite those limitations, the reduced-order models M2 and M3 are capable of analyzing the potential risk of asynchronous ground excitation and local site (basin) effect to the integrity of extended structures. For instance, time histories of y-displacement at three control points are fairly uniform for homogeneous half-space, as shown in Fig. 5.14. Meanwhile, for heterogeneous medium, as shown in Fig. 5.15, y-displacements at different control points are considerably different from each other, because of the wave interference inside the basin. It is well-known that the differential displacement between pipe nodes causes excess strains and stresses in pipe elements, potentially threatening the integrity of pipeline networks.

5.4 Conclusions

This chapter presents a demonstration of how to incorporate the SIFs obtained in Chapters 3 and 4 into a reduced-order model to analyze SPI problems, specifically a straight pipe subjected to Rayleigh surface wave propagating through homogeneous and heterogeneous elastic half-spaces. The displacements at the control points calculated by reduced-order model, either with free-field input motion or with PIM, are of the same order of magnitude with those by direct model using 2D FE analyses. Especially, the reduced-order model using PIM agrees well with the direct model, sufficiently capturing the amplitude and phase of time histories of the x- and y-displacements at three control points.

The reduced-order model, together with the derived SIFs, will benefit earthquake engineering methods by providing a versatile tool to account for the effects of spatial variability and incoherency in the seismic demand of extended structures.

Chapter 6

Conclusions

Contents of this chapter

6.1 Summary of previous chapters

This thesis presents the author's research into the reduced-order model for dynamic SPI problems to evaluate the seismic performance of that structure.

Chapter 2 presents a mechanics-based reduced-order model to capture SPI in sandy soils under biaxial loading on a two-dimensional plane perpendicular to the pipe axis. This model is calibrated with published experimental data and FE analyses. For the FDC of soil spring, unlike the most widely used ASCE bilinear model, this novel method is able to take into consideration the true smooth nonlinearity, hysteresis loop, pinching phenomenon, and coupling between lateral and vertical soil-pipe motions. Results of the proposed method show great agreement with those computed by FE analyses and SPH approaches for different cases of loading patterns. The limitations of the proposed approach are that it currently is applicable to the case of rigid (or nearly rigid) pipes, and that it cannot capture the post-peak (softening) behavior of FDC, which has been observed for dense to very dense sands.

Chapters 3 and 4 derive analytical solutions to compute the frequency-domain axial and in-plane SIFs, respectively, for an infinitely long rigid cylinder buried in homogeneous half-space. Using Hankel– and Bessel–Fourier series expansion, we solved a mixed-boundary-value problem considering a harmonic displacement at the structure boundary and traction-free boundary condition at the half-space free surface. We then verified our analytical solutions using results obtained from FE simulations. The results show that SIFs strongly vary with the frequency of excitation, because of the constructive and destructive interference of waves occurring within the region between soil free surface and the structure. The SIFs depend on shear modulus and Poisson's ratio of the half-space, burial location and dimension of structure, and also on material contrast in case of two-layered half-space.

The results from Chapters 3 and 4 will provide the community database of dynamic SIFs in a tabulated or graphical form, to enable their use by practitioners who are interested in

selecting the most appropriate values of springs and dashpots for this class of SPI problems. Accordingly, Chapter 5 presents a project that exemplifies the potentials of those SIF results: a straight pipe subjected to Rayleigh surface wave propagating through homogeneous and heterogeneous half-spaces. We showed that the reduced-order model with appropriate springs and dashpots yields satisfactory results of displacement time histories at the control points, compared to those computed by direct 2D FE analyses. This reduced-order model, together with the derived SIFs, obviously provides a robust and versatile tool to improve the analysis of buried structures under seismic excitation, while maintaining computational efficiency.

6.2 Future work

A physics-based reduced-order model to analyze the SbSI problems under seismic excitation is going to be proposed. Specifically, given the pipeline (or tunnel) network information, as well as the seismic hazard maps, we will provide values for soil springs and dashpots to be incorporated into a physics-based model to design or evaluate the seismic performances of the structural system.

Furthermore, we aim to build a nonlinear reduced-order model for SPI analysis in time domain under TGD. The proposed model is a combination of the hysteresis Bouc–Wen model and the derived SIFs, in which it behaves similarly to a linear system of frequency-dependent springs and dashpots for weak ground shaking while generating a nonlinear FDC for strong ground shaking. This model is able to capture the main features of the system with an efficient computational effort.

Bibliography

Abramowitz, M., and I. A. Stegun (1948), *Handbook of mathematical functions with formulas, graphs, and mathematical tables*, vol. 55, US Government printing office.

Ahmad, S., and A. Bharadwaj (1991), Horizontal impedance of embedded strip foundations in layered soil, *Journal of geotechnical engineering*, *117*(7), 1021–1041.

ALA (2005), Seismic guidelines for water pipelines, *Report R80.01.01*, American Lifelines Alliance, Washington, DC.

Anastasopoulos, I., N. Gerolymos, V. Drosos, R. Kourkoulis, T. Georgarakos, and G. Gazetas (2007), Nonlinear response of deep immersed tunnel to strong seismic shaking, *Journal of Geotechnical and Geoenvironmental Engineering*, *133*(9), 1067–1090, doi: 10.1061/(ASCE)1090-0241(2007)133:9(1067).

Ancheta, T. D., R. B. Darragh, J. P. Stewart, E. Seyhan, W. J. Silva, B. S. Chiou, K. E. Wooddell, R. W. Graves, A. R. Kottke, D. M. Boore, et al. (2013), PEER NGA-WEST2 database.

ASCE (1984), Guidelines for the seismic design of oil and gas pipeline systems, *Report*, Committee on Gas and Liquid Fuel Lifeline, ASCE, Reston, VA.

Asimaki, D., J. Garcia-Suarez, D. Kusanovic, K. Nguyen, and E. E. Seylabi (2019), Next generation reduced order models for soil-structure interaction, in *Earthquake Geotechnical Engineering for Protection and Development of Environment and Constructions*, vol. 4, edited by F. Silvestri and N. Moraci, pp. 138–152, CRC Press, London, doi: 10.1201/9780429031274.

Audibert, J. M., and K. J. Nyman (1977), Soil restraint against horizontal motion of pipes, *Journal of the Geotechnical Engineering Division*, *103*(10), 1119–1142.

Ayala, A. G., M. J. O'Rourke, et al. (1989), *Effects of the 1985 Michoacan earthquake on water systems and other buried lifelines in Mexico*, National Center for earthquake engineering research.

Ayoubi, P., D. Asimaki, and K. Mohammdi (2018), *Basin Effects in Strong Ground Motion: A Case Study from the 2015 Gorkha, Nepal, Earthquake*, pp. 288–296, ASCE, doi: 10.1061/9780784481462.028.

Baber, T. T., and M. N. Noori (1985), Random vibration of degrading, pinching systems, *Journal of Engineering Mechanics*, *111*(8), 1010–1026, doi:10.1061/(ASCE)0733-9399(1985)111:8(1010).

Basu, U. (2009), Explicit finite element perfectly matched layer for transient three-dimensional elastic waves, *International Journal for Numerical Methods in Engineering*, *77*(2), 151–176.

Bharadwaj, A., and S. Ahmad (1992), Rocking impedance of embedded strip foundations in layered soil, *Journal of geotechnical engineering*, *118*(5), 796–813.

Bielak, J., K. Loukakis, Y. Hisada, and C. Yoshimura (2003), Domain Reduction Method for Three-Dimensional Earthquake Modeling in Localized Regions, Part I: Theory, *Bulletin of the Seismological Society of America*, *93*(2), 817–824, doi:10.1785/0120010251.

Bouc, R. (1971), Modele mathematique d'hysteresis, *Acustica*, *24*(1), 16–25.

Bransby, M., T. Newson, P. Brunning, and M. Davies (2001), Numerical and centrifuge modeling of the upheaval resistance of buried pipelines, in *20th International Conference on Offshore Mechanics and Arctic Engineering; Polar and Arctic Pipeline Technology*, ASME, New York.

Burnett, A. J. (2015), Investigation of full-scale horizontal pipe-soil interaction and large strain behaviour of sand, MASc. thesis, Queen's Univ., Kingston, Ontario, Canada.

CEN (2006), Eurocode 8, part 4: silos, tanks and pipelines, CEN EN1998-4, *Standard*, European Committee for Standardization, Brussels.

CIA (2018), *The World Factbook 2018*, Central Intelligence Agency, Washington DC.

Colton, J. (1981), *Measurement of dynamic soil-pipe axial interaction for full-scale buried pipelines under field laying conditions*, SRI International.

Colton, J., P. Chang, and H. Lindberg (1982), Measurement of dynamic soil-pipe axial interaction for full-scale buried pipelines, *International Journal of Soil Dynamics and Earthquake Engineering*, *1*(4), 183–188, doi:https://doi.org/10.1016/0261-7277(82)90022-5.

Daiyan, N. (2013), Investigating soil/pipeline interaction during oblique relative movements, Ph.D. thesis, Memorial University of Newfoundland.

Datta, T., and E. Mashaly (1986), Pipeline response to random ground motion by discrete model, *Earthquake engineering & structural dynamics*, *14*(4), 559–572.

Datta, T. K., and E. A. Mashaly (1988), Seismic Response of Buried Submarine Pipelines, *Journal of Energy Resources Technology*, *110*(4), 208–218, doi:10.1115/1.3231384.

Davidson, R., and C. Poland (2016), Lifelines (EERI Earthquake Reconnaissance Team Report: M7. 8 Gorkha, Nepal Earthquake on April 25, 2015 and Its Aftershocks), *Tech. rep.*, Earthquake Engineering Research Institute.

DeSanto, J. A. (1992), Scalar wave theory, in *Scalar Wave Theory*, pp. 1–31, Springer.

Di Prisco, C., and A. Galli (2006), Soil-pipe interaction under monotonic and cyclic loads: experimental and numerical modelling, in *Proceedings of the First Euromediterranean Symposium on Advances in Geomaterials and Structures, Hammamet, Tunisia*, vol. 35, pp. 755–760, Commission Universitaire pour le Developpement.

Dickin, E. A. (1994), Uplift resistance of buried pipelines in sand, *Soils and foundations*, *34*(2), 41–48.

El Hmadi, K., and M. J. O'Rourke (1988), Soil springs for buried pipeline axial motion, *Journal of geotechnical engineering*, *114*(11), 1335–1339.

Esposito, S., S. Giovinazzi, L. Elefante, and I. Iervolino (2013), Performance of the L'aquila (central Italy) gas distribution network in the 2009 (M_w 6.3) earthquake, *Bulletin of Earthquake Engineering*, *11*(6), 2447–2466, doi:10.1007/s10518-013-9478-8.

Finch, M. (1999), Upheaval buckling and floatation of rigid pipelines: The influence of recent geotechnical research on the current state of the art, in *Proc., Offshore Technology Conference*, Texas.

Gazetas, G. (1980), Static and dynamic displacements of foundations on heterogeneous multilayered soils, *Geotechnique*, *30*(2), 159–177.

Gazetas, G. (1983), Analysis of machine foundation vibrations: state of the art, *International Journal of Soil Dynamics and Earthquake Engineering*, *2*(1), 2–42.

Goit, C. S., and M. Saitoh (2013), Model tests and numerical analyses on horizontal impedance functions of inclined single piles embedded in cohesionless soil, *Earthquake engineering and engineering vibration*, *12*(1), 143–154.

Graff, K. F. (2012), *Wave motion in elastic solids*, Courier Corporation.

Guo, P. (2005), Numerical modeling of pipe-soil interaction under oblique loading, *Journal of Geotechnical and Geoenvironmental Engineering*, *131*(2), 260–268, doi:10.1061/(ASCE)1090-0241(2005)131:2(260).

Guo, P. J., and D. F. E. Stolle (2005), Lateral pipe-soil interaction in sand with reference to scale effect, *Journal of Geotechnical and Geoenvironmental Engineering*, *131*(3), 338–349, doi:10.1061/(ASCE)1090-0241(2005)131:3(338).

Hallquist, J. O. (2006), *LS-DYNA Theory Manual*.

Hamada, M. (1992), Case studies of liquefaction and lifeline performance during past earthquakes, vol. 1; Japanese case studies, *National Center for Earthquake Engineering Research, Technical Report*, *92*, 341.

Hashash, Y. M., J. J. Hook, B. Schmidt, I. John, and C. Yao (2001), Seismic design and analysis of underground structures, *Tunnelling and underground space technology*, *16*(4), 247–293.

Helmholtz, H. (1858), Über integrale der hydrodynamischen gleichungen, welche den wirbelbewegungen entsprechen., *Journal für die reine und angewandte Mathematik*, *1858*(55), 25–55.

Highland, L., P. T. Bobrowsky, et al. (2008), *The landslide handbook: a guide to understanding landslides*, US Geological Survey Reston.

Hindy, A., and M. Novak (1979), Earthquake response of underground pipelines, *Earthquake Engineering & Structural Dynamics*, *7*(5), 451–476.

Hindy, A., and M. Novak (1980), Pipeline response to random ground motion, *Journal of the Engineering Mechanics Division*, *106*(2), 339–360.

Hryniewicz, Z. (1981), Dynamic response of a rigid strip on an elastic half-space, *Computer methods in applied mechanics and engineering*, *25*(3), 355–364.

Hsu, T.-W. (1996), Soil restraint against oblique motion of pipelines in sand, *Canadian geotechnical journal*, *33*(1), 180–188.

Hsu, T.-W., Y.-J. Chen, and C.-Y. Wu (2001), Soil friction restraint of oblique pipelines in loose sand, *Journal of Transportation Engineering*, *127*(1), 82–87, doi:10.1061/(ASCE) 0733-947X(2001)127:1(82).

Hsu, Y. S. (2020), Finite element approach of the buried pipeline on tensionless foundation under random ground excitation, *Mathematics and Computers in Simulation*, *169*, 149–165, doi:https://doi.org/10.1016/j.matcom.2019.09.004.

Hurley, S., and R. Phillips (1999), *Large Scale Modelling of Pipeline/soil Interaction Under Lateral Loading*, C-CORE, Memorial University of Newfoundland.

Iserles, A., and S. P. Nørsett (2005), Efficient quadrature of highly oscillatory integrals using derivatives, *Proceedings of the Royal Society A: Mathematical, Physical and Engineering Sciences*, *461*(2057), 1383–1399.

Israil, A., and S. Ahmad (1989), Dynamic vertical compliance of strip foundations in layered soils, *Earthquake engineering & structural dynamics*, *18*(7), 933–950.

Joshi, S., A. Prashant, A. Deb, and S. K. Jain (2011), Analysis of buried pipelines subjected to reverse fault motion, *Soil Dynamics and Earthquake Engineering*, *31*(7), 930–940, doi:https://doi.org/10.1016/j.soildyn.2011.02.003.

Jung, J. K., T. D. O'Rourke, and C. Argyrou (2016), Multi-directional force-displacement response of underground pipe in sand, *Canadian Geotechnical Journal*, *53*(11), 1763–1781, doi:10.1139/cgj-2016-0059.

Karasudhi, P., L. M. Keer, and S. L. Lee (1968), Vibratory Motion of a Body on an Elastic Half Plane, *Journal of Applied Mechanics*, *35*(4), 697–705, doi:10.1115/1.3601294.

Karimian, H., D. Wijewickreme, and D. Honegger (2006), Full-scale laboratory testing to assess methods for reduction of soil loads on buried pipes subject to transverse ground movement, in *Proc 6th international pipeline conference, Calgary, Canada*, vol. 1, pp. 91–99, ASME, doi:10.1115/IPC2006-10047.

Kausel, E. (2006), *Fundamental Solutions in Elastodynamics: A Compendium*, Cambridge University Press, Cambridge, doi:10.1017/CBO9780511546112.

Kausel, E. (2010), Early history of soil–structure interaction, *Soil Dynamics and Earthquake Engineering*, *30*(9), 822–832.

Kausel, E., R. V. Whitman, J. P. Morray, and F. Elsabee (1978), The spring method for embedded foundations, *Nuclear Engineering and design*, *48*(2–3), 377–392.

Kouretzis, G. P., D. K. Karamitros, and S. W. Sloan (2015), Analysis of buried pipelines subjected to ground surface settlement and heave, *Canadian geotechnical journal*, *52*(8), 1058–1071.

Kronrod, A. S. (1965), *Nodes and weights of quadrature formulas, sixteen-place tables: Authorized translation from the Russian*, New York: Consultants Bureau.

Kuesel, T. R. (1969), Earthquake design criteria for subways, *Journal of the structural division*, pp. 1213–1231.

Lee, D. H., B. H. Kim, H. Lee, and J. S. Kong (2009), Seismic behavior of a buried gas pipeline under earthquake excitations, *Engineering Structures*, *31*(5), 1011–1023, doi:10.1016/j.engstruct.2008.12.012.

Lin, C. H., V. W. Lee, M. I. Todorovska, and M. D. Trifunac (2010), Zero-stress, cylindrical wave functions around a circular underground tunnel in a flat, elastic half-space: incident p-waves, *Soil Dynamics and Earthquake Engineering*, *30*(10), 879–894.

Liu, M., and G. Liu (2010), Smoothed particle hydrodynamics (SPH): An overview and recent developments, *Archives of computational methods in engineering*, *17*(1), 25–76.

Liu, W., H. Miao, C. Wang, and J. Li (2018), The stiffness of axial pipe-soil springs and axial joint springs tested by artificial earthquakes, *Soil Dynamics and Earthquake Engineering*, *106*, 41–52, doi:https://doi.org/10.1016/j.soildyn.2017.12.014.

Liu, X., H. Zhang, Y. Han, M. Xia, and W. Zheng (2016), A semi-empirical model for peak strain prediction of buried x80 steel pipelines under compression and bending at strike-slip fault crossings, *Journal of Natural Gas Science and Engineering*, *32*, 465–475, doi:https://doi.org/10.1016/j.jngse.2016.04.054.

Luco, J., and R. Westmann (1972), Dynamic response of a rigid footing bonded to an elastic half space, *Journal of Applied Mechanics*, *39*(2), 527–534.

Lund, L., and T. Cooper (1995), *Water Systems*, chap. 4, p. 96, American Society of Civil Engineers, New York.

Lysmer, J., and R. L. Kuhlemeyer (1969), Finite dynamic model for infinite media, *Journal of the Engineering Mechanics Division*, *95*(4), 859–878.

Matsubara, K., and M. Hoshiya (2000), Soil spring constants of buried pipelines for seismic design, *Journal of engineering mechanics*, *126*(1), 76–83.

Mavridis, G., and K. Pitilakis (1996), Axial and transverse seismic analysis of buried pipelines, in *Proceedings of the 11th World Conference on Earthquake Engineering*, pp. 81–88.

Mindlin, R. (1964), Displacements and stresses due to nuclei of strain in the elastic half-space, *Report, Department of Civil Engineering and Engineering Mechanics, Columbia University, New York.*

Mow, C.-C., and Y.-H. Pao (1971), The diffraction of elastic waves and dynamic stress concentrations, *Tech. rep.*, RAND CORP SANTA MONICA CALIF.

Muleski, G., and T. Ariman (1985), A shell model for buried pipes in earthquakes, *International Journal of Soil Dynamics and Earthquake Engineering*, *4*(1), 43–51.

Nasu, N., S. Kazama, T. Morioka, and T. Tamura (1974), Vibration test of the underground pipe with a comparatively large cross section, in *Proceedings of the Fifth World Conference on Earthquake Engineering*, vol. 1, p. 583.

Newmark, N. M. (1968), Problem in wave propagation in soil and rock, in *Proceedings of Int. Symp. Wave Propagation and Dynamic Properties of Earth Materials*, pp. 7–26, Univ. New Mexico Press.

Nguyen, K. T., and D. Asimaki (2018), A modified uniaxial Bouc–Wen model for the simulation of transverse lateral pipe-cohesionless soil interaction, in *Geotechnical Earthquake Engineering and Soil Dynamics V*, pp. 25–36, American Society of Civil Engineers, Texas, doi:10.1061/9780784481479.003.

Nguyen, K. T., and D. Asimaki (2020), Smooth nonlinear hysteresis model for coupled biaxial soil-pipe interaction in sandy soils, *Journal of Geotechnical and Geoenvironmental Engineering*, *146*(6), doi:10.1061/(ASCE)GT.1943-5606.0002230.

NIST, G. (2012), Gcr 12-917-21 (2012) soil-structure interaction for building structures, *Gaithersburg, National Institute of Standards and Technology.*

Nourzadeh, D., and S. Takada (2013), Response of gas distribution pipeline network to seismic wave propagation in greater Tehran area, Iran, in *International Efforts in Lifeline Earthquake Engineering*, pp. 237–244, ASCE.

Novak, M., and F. Aboul-Ella (1978), Impedance functions of piles in layered media, *Journal of the Engineering Mechanics Division*, *104*(3), 643–661.

Novak, M., F. Aboul-Ella, and T. Nogami (1978), Dynamic soil reactions for plane strain case, *Journal of the Engineering Mechanics Division*, *104*(4), 953–959.

Nyman, K. J. (1984), Soil response against oblique motion of pipes, *Journal of Transportation Engineering*, *110*(2), 190–202.

Ogawa, Y., and T. Koike (2001), Structural design of buried pipelines for severe earthquakes, *Soil Dynamics and Earthquake Engineering*, *21*(3), 199–209.

Olson, N. (2009), Soil performance for large scale soil-pipeline tests, Ph.D. thesis, Cornell University, Ithaca, NY.

O'Rourke, M. (2009), *Wave Propagation Damage to Continuous Pipe*, pp. 1–9, American Society of Civil Engineers, doi:10.1061/41050(357)76.

O'Rourke, M., and C. Nordberg (1992), Behavior of buried pipelines subject to permanent ground deformation, in *Proc., 10th World Conf. on Earthquake Engineering*, pp. 5411–5416, Balkema, Rotterdam.

O'Rourke, M. J., and K. El Hmadi (1988), Analysis of continuous buried pipelines for seismic wave effects, *Earthquake Engineering & Structural Dynamics*, *16*(6), 917–929, doi:10.1002/eqe.4290160611.

O'Rourke, M. J., and X. Liu (1999), *Response of buried pipelines subject to earthquake effects*, Multidisciplinary Center for Earthquake Engineering Research, NY.

O'Rourke, T. (2010), Geohazards and large, geographically distributed systems, *Géotechnique*, *60*(7), 505–543, doi:10.1680/geot.2010.60.7.505.

O'Rourke, T., and M. Palmer (1996), Earthquake performance of gas transmission pipelines, *Earthquake Spectra*, *12*(3), 493–527.

Padrón, L., J. Aznárez, O. Maeso, and M. Saitoh (2012), Impedance functions of end-bearing inclined piles, *Soil Dynamics and Earthquake Engineering*, *38*, 97–108.

Pitilakis, K., and G. Tsinidis (2014), *Performance and Seismic Design of Underground Structures*, chap. 11, pp. 279–340, Springer International Publishing, Cham, doi:10.1007/978-3-319-03182-8_11.

PRCI (2004), Guidelines for the seismic design and assessment of natural gas and liquid hydrocarbon pipelines, *Report*, Pipeline Research Council International, Houston, TX.

PRCI (2009), Guidelines for constructing natural gas and liquid hydrocarbon pipelines through areas prone to landslide and subsidence hazards, *Report*, Pipeline Research Council International, Houston, TX.

Psyrras, N., O. Kwon, S. Gerasimidis, and A. Sextos (2019), Can a buried gas pipeline experience local buckling during earthquake ground shaking?, *Soil Dynamics and Earthquake Engineering*, *116*, 511–529.

Rajapakse, R., and A. Shah (1988), Impedances of embedded rigid strip foundations, *Earthquake engineering & structural dynamics*, *16*(2), 255–273.

Robert, D. J., and N. I. Thusyanthan (2015), Numerical and experimental study of uplift mobilization of buried pipelines in sands, *Journal of Pipeline Systems Engineering and Practice*, *6*(1), 04014,009, doi:10.1061/(ASCE)PS.1949-1204.0000179.

Robert, D. J., K. Soga, and T. D. O'Rourke (2016a), Pipelines subjected to fault movement in dry and unsaturated soils, *International Journal of Geomechanics*, *16*(5), C4016,001, doi:10.1061/(ASCE)GM.1943-5622.0000548.

Robert, D. J., K. Soga, T. D. O'Rourke, and T. Sakanoue (2016b), Lateral load-displacement behavior of pipelines in unsaturated sands, *Journal of Geotechnical and Geoenvironmental Engineering*, *142*(11), 04016,060, doi:10.1061/(ASCE)GT.1943-5606.0001504.

Saberi, M., F. Behnamfar, and M. Vafaeian (2013), A semi-analytical model for estimating seismic behavior of buried steel pipes at bend point under propagating waves, *Bulletin of Earthquake Engineering*, *11*(5), 1373–1402.

Sakurai, A., and T. Takahashi (1969), Dynamic stresses of underground pipelines during earthquakes, in *Proc., 4th World Conf. on Earthquake Engineering*, pp. 81–95, Editorial Universitaria, Santiago de Chile.

Seron, F., J. Badal, and F. Sabadell (1996), A numerical laboratory for simulation and visualization of seismic wavefields, *Geophysical Prospecting*, *44*(4), 603–642.

Seylabi, E. E. (2016), Reduced order modeling of soil structure interaction problems, Ph.D. thesis, UCLA.

Seylabi, E. E., C. Jeong, and E. Taciroglu (2016), On numerical computation of impedance functions for rigid soil-structure interfaces embedded in heterogeneous half-spaces, *Computers and Geotechnics*, *72*, 15–27.

Shinozuka, M., and T. Koike (1979), *Estimation of structural strains in underground lifeline pipes*, Columbia University, Department of Civil Engineering and Engineering Mechanics.

Simon, D. (2006), *Optimal State Estimation: Kalman, H Infinity, and Nonlinear Approaches*, Wiley-Interscience.

Smith, C. E. (2018), Near-term pipeline plans nearly double, future slows, *Oil & Gas Journal*, *116*(2), 72–82.

St John, C., and T. Zahrah (1987), Aseismic design of underground structures, *Tunnelling and underground space technology*, *2*(2), 165–197.

Tang, A. K., and J. M. Eidinger (2013), *Chile Earthquake of 2010*, American Society of Civil Engineers, doi:10.1061/9780784412824.

Towne, D. H. (1988), *Wave phenomena*, chap. 11, p. 203, Courier Dover Publications, New York.

Trautmann, C. (1983), Behavior of pipe in dry sand under lateral and uplift loading, Ph.D. thesis, Cornell University, Ithaca, NY.

Uckan, E. (2013), *Lifeline Damage Caused in the 23 October (Mw=7.2) 2011 and 9 November (M=5.6) 2011, Van Earthquakes in Eastern Turkey*, pp. 51–58, American Society of Civil Engineers, doi:10.1061/9780784413234.007.

Varun, and D. Assimaki (2012), A generalized hysteresis model for biaxial response of pile foundations in sands, *Soil Dynamics and Earthquake Engineering*, *32*(1), 56–70, doi:https://doi.org/10.1016/j.soildyn.2011.08.004.

Vazouras, P., and S. A. Karamanos (2017), Structural behavior of buried pipe bends and their effect on pipeline response in fault crossing areas, *Bulletin of Earthquake Engineering*, *15*(11), 4999–5024.

Vazouras, P., S. A. Karamanos, and P. Dakoulas (2010), Finite element analysis of buried steel pipelines under strike-slip fault displacements, *Soil Dynamics and Earthquake Engineering*, *30*(11), 1361–1376.

Vazouras, P., P. Dakoulas, and S. A. Karamanos (2015), Pipe-soil interaction and pipeline performance under strike-slip fault movements, *Soil Dynamics and Earthquake Engineering*, *72*, 48–65.

Vesic, A. (1961), Beams on elastic subgrade and the Winkler's hypothesis, in *Proc. 5th Int. Conf. on SMFE*, vol. 1, pp. 845–851.

Viktorov, I. A. (1967), *Rayleigh and Lamb Waves: Physical Theory and Applications: Translated from Russian*, Plenum Press, New York.

Wang, C.-H., and S.-Y. Chang (2007), Development and validation of a generalized biaxial hysteresis model, *Journal of engineering mechanics*, *133*(2), 141–152.

Wen, Y.-K. (1976), Method for random vibration of hysteretic systems, *Journal of the engineering mechanics division*, *102*(2), 249–263.

Yan, K., J. Zhang, Z. Wang, W. Liao, and Z. Wu (2018), Seismic responses of deep buried pipeline under non-uniform excitations from large scale shaking table test, *Soil Dynamics and Earthquake Engineering*, *113*, 180–192, doi:https://doi.org/10.1016/j.soildyn.2018.05.036.

Yimsiri, S., K. Soga, K. Yoshizaki, G. R. Dasari, and T. D. O'Rourke (2004), Lateral and upward soil-pipeline interactions in sand for deep embedment conditions, *Journal of Geotechnical and Geoenvironmental Engineering*, *130*(8), 830–842, doi:10.1061/(ASCE)1090-0241(2004)130:8(830).

A p p e n d i x   A

Asymptotic method for computing high oscillatory integrals

The asymptotic method is based on a theorem proposed by *Iserles and Nørsett* (2005), reads as follows

Theorem 1 *Let $f, g \in C^\infty[a, b]$, g is strictly monotone and $g' \neq 0$ on $[a, b]$. Consider a highly oscillatory integral*

$$I[f] = \int_a^b f(x)e^{i\omega g(x)} \mathrm{d}x .$$

Let

$$Q_s[f] = -\sum_{k=0}^{s} \frac{1}{(-i\omega)^{k+1}} \left[\frac{f_k(b)}{g'(b)} e^{i\omega g(b)} - \frac{f_k(a)}{g'(a)} e^{i\omega g(a)} \right] ,$$

where $s \in \mathbb{Z}^+$ and f_k is defined by $f_0(x) = f(x)$ and $f_k(x) = \dfrac{\mathrm{d}}{\mathrm{d}x} \dfrac{f_{k-1}(x)}{g'(x)}$ for $k \geq 1$. Then, for $\omega \to \infty$, $I[f] = Q_s[f] + O(\omega^{-s-2})$.

Take I_1 in Eq. (4.49) as an example. It is rewritten as

$$I_1 = \int_0^1 \frac{-i}{\sqrt{1-\xi^2}} \frac{\left(2\xi^2 - r_0^2\right)^2 - 4\xi^2 \sqrt{1-\xi^2} \sqrt{r_0^2 - \xi^2}}{\left(2\xi^2 - r_0^2\right)^2 + 4\xi^2 \sqrt{1-\xi^2} \sqrt{r_0^2 - \xi^2}} \left[\left(\xi + i\sqrt{1-\xi^2}\right)^{n+m} + \right.$$

$$\left. \left(-\xi + i\sqrt{1-\xi^2}\right)^{n+m} \right] e^{i2hk_\alpha \sqrt{1-\xi^2}} \mathrm{d}\xi.$$

With large burial depth h, the integrand of I_1 oscillates rapidly. The classical Gaussian quadrature rule requires exceedingly small subintervals. For large enough h, this classical method is useless because the error is $O(1)$ as $h \to \infty$. Instead, we used asymptotic method based on theorem 1 to evaluate I_1. By changing the variable $\nu = \sqrt{1-\xi^2}$, we remove the singularity at $\xi = 1$ and ensure that $g' \neq 0$ on $[0, 1]$ as well, but a new singularity appears at $\nu = 1$ ($\xi = 0$). To handle this, we write

$$I_1 = \int_0^1 \mathcal{F}(\xi)\mathrm{d}\xi = \underbrace{\int_0^{c_0} \mathcal{F}(\xi)\mathrm{d}\xi}_{I_{11}} + \underbrace{\int_{c_0}^1 \mathcal{F}(\xi)\mathrm{d}\xi}_{I_{12}} = I_{11} + I_{12} ,$$

where $c_0 = \sqrt{\dfrac{2\pi n_c}{hk_\alpha} - \left(\dfrac{\pi n_c}{hk_\alpha}\right)^2}$. Gauss–Kronrod quadrature was used to evaluate I_{11}, which is the integration over the first n_c cycles of the integrand from $\xi = 0$ to $\xi = c_0$. This study used $n_c = 100$. For I_{12}, let $v = \sqrt{1 - \xi^2}$, we have

$$
I_{12} = \int_0^{1-\frac{\pi n_c}{hk_\alpha}} \frac{-i}{\sqrt{1-v^2}} \frac{\left(2(1-v^2) - r_0^2\right)^2 - 4(1-v^2)v\sqrt{r_0^2 - 1 + v^2}}{\left(2(1-v^2) - r_0^2\right)^2 + 4(1-v^2)v\sqrt{r_0^2 - 1 + v^2}} \times
$$
$$
\left[\left(\sqrt{1-v^2} + iv\right)^{n+m} + \left(-\sqrt{1-v^2} + iv\right)^{n+m}\right] e^{i2hk_\alpha v} dv.
$$

Clearly, I_{12} is of the form $I_{12}[f] = \int_0^{1-\frac{\pi n_c}{hk_\alpha}} f(v) e^{i\omega g(v)} dv$, with $\omega = 2hk_\alpha$ and $g(v) = v$. From theorem 1 with $s = 2$, we computed

$$
I_{12} = -\sum_{k=0}^{2} \frac{1}{(-i2hk_\alpha)^{k+1}} \left[f_k\left(1 - \frac{\pi n_c}{hk_\alpha}\right) e^{i2hk_\alpha\left(1-\frac{\pi n_c}{hk_\alpha}\right)} - f_k(0) \right].
$$

Note that

$$
f_0 = f, \quad f_1 = -\frac{g''}{g'^2} f + \frac{1}{g'} f' = f', \quad f_2 = \left(\frac{3g''^2}{g'^4} - \frac{g'''}{g'^3}\right) f - \frac{3g''}{g'^3} f' + \frac{1}{g'^2} f'' = f''.
$$

The values of the function f and its derivatives f', f'' at $v = 0$ and $v = 1 - \frac{\pi n_c}{hk_\alpha}$ were computed numerically.